IMMW 2001

Center for Research in Scientific Computation

NC STATE UNIVERSITY

Industrial Mathematics Modeling Workshop

for Graduate Students, July 23 - July 31, 2001

Edited by Pierre A. Gremaud, Zhilin Li, Ralph C. Smith and Hien T. Tran

Participants

Graduate Students

1. Soad Abuhawas, Texas Tech University, sahmad02@yahoo.com

2. John Bardsley, Montana State University, bardsley@math.montana.edu

3. Jeffrey B. Burnett, North Carolina State University, jbburnet@stat.ncsu.edu

4. Gregory Daspit, The University of Alabama at Birmingham, gdaspit@math.uab.edu

5. Oliver Diaz, University of Texas at Austin, odiaz@math.utexas.edu

6. Nathan Gibson, North Carolina State University, gibso@math.utk.edu

7. Chuan Hsiang Han, North Carolina State University, chan2@unity.ncsu.edu

8. Eugenie Jackson, East Tennessee State University, zems8@yahoo.com

9. Valeriy Korostyshevskiy, University of Maryland, Baltimore County, korostys@math.umbc.edu

10. Mark Kozek, Wake Forest University, kozemr0@wfu.edu

11. Shannon Kubiak, Towson University, smkubiak@msn.com

12. Jason Kurtz, Clarkson University, kurtzj@clarkson.edu

13. Scott La Voie, East Tennessee State University, zsll9@etsu.edu

14. Chunhua Lan, Washington University, lc2@cec.wustl.edu

15. Heather Lehr, University of Texas at Austin, heather@mail.ma.utexas.edu

16. Rachel Levy, North Carolina State University, raylevy@netpath.net

17. Terry Jo Lieterman, University of North Carolina at Chapel Hill, terryjo@amath.unc.edu

18. Kevin Lynch, East Tennessee State University, mathrocks25@yahoo.com

19. Cynthia Martin, Texas Tech University, cmartin@math.ttu.edu

20. Todd Moeller, Georgia Institute of Technology, moeller@math.gatech.edu

21. Ahmed A. Naga, Wayne State University, anaga@math.wayne.edu

22. Abigail Ochberg, University of Michigan, aochberg@math.lsa.umich.edu

23. Mahendra Panagoda, Michigan State University, panagoda@msu.edu

24. Albert Parker, Montana State University - Bozeman, parker@math.montana.edu

25. Luis A. Cueva Parra, The University of Southern Mississippi, cueva@pax.st.usm.edu

26. Jae-Hong Pyo, University of Maryland at College Park, pjh@math.umd.edu

27. Zoi Rapti, University of Massachusetts at Amherst, Zrapti@hotmail.com

28. Jill Reese, North Carolina State University, jillian2179@yahoo.com

29. Bing Song, University of California, Los Angeles, songbing@math.ucla.edu

30. Yoon Song, University of Maryland - Baltimore County, ysong1@umbc.edu

31. Edward J. Swim, Texas Tech University, eswim@math.ttu.edu

32. Hansun To, Temple University, hansun@math.temple.edu

33. Chad Wilson, University of Alabama at Birmingham, chad@math.uab.edu

34. Kittipat Wong, University of Illinois at Urbana-Champaign, kwong1@math.uiuc.edu

35. Xingzhou Yang, North Carolina State University, xyang3@unity.ncsu.edu

36. Yan Yu, State University of New York at Stony Brook, yan2000@ams.sunysb.edu

37. Stanilslav Zabic, Louisiana State University, zabic@lsu.edu

38. Yi Zhao, Rutgers University, yzhao@math.rutgers.edu

Problem Presenters and Faculty

1. H.T. Banks, North Carolina State University, htbanks@eos.ncsu.edu

2. Damon Christenbury, Michelin, North America, damon.christenbury@us.michelin.com

3. Jean-Pierre Fouque, North Carolina State University, fouque@math.ncsu.edu

4. Khaled Furati, North Carolina State University, kmfurati@kfupm.edu.sa

5. Pierre Gremaud, North Carolina State University, gremaud@unity.ncsu.edu

6. Farshid Guilak, Orthopaedic Research Laboratories, Department of Surgery, Duke University Medical Center, guilak@duke.edu

7. Sarah Holte, Fred Hutchinson Cancer Research Center, sarah@hivnet.fhcrc.org

8. Holly Leddy, Orthopaedic Research Laboratories, Department of Surgery, Duke University Medical Center, hal2@duke.edu

9. Sharon Lubkin, North Carolina State University, lubkin@eos.ncsu.edu

10. Zhilin Li, North Carolina State University, zhilin@math.ncsu.edu

11. James M. Nelson, Boeing Phantom Works, james.nelson3@pss.boeing.com

12. Zoubeida Ounaies, ICASE, NASA Langley Research Center, z.ounaies@larc.nasa.gov

13. Yeol C. Seong, Commodities Derivatives Group, Bank of Montreal, Yeol.seong@bmo.com

14. Ralph Smith, North Carolina State University, rsmith@unity.ncsu.edu

15. Hien Tran, North Carolina State University, tran@control.math.ncsu.edu

16. Yue Zhang, Michelin, North America, Yue.Zhang@us.michelin.com

Contents

Preface

This volume contains the proceedings of the Industrial Mathematics Modeling Workshop for Graduate Students that was held at the Center for Research in Scientific Computation at North Carolina State University (NCSU), Raleigh, North Carolina, July 23 - July 31, 2001. This workshop which was the seventh one held at NCSU brought together 39 graduate students. These students represented a large number of graduate programs including Clarkson University, East Tennessee State University, Georgia Institute of Technology, Louisiana State University, Michigan State University, Montana State University, Rutgers University, State University of New York at Stony Brook, Temple University, Texas Tech University, Towson University, University of Alabama at Birmingham, University of California at Los Angeles, University of Illinois at Urbana-Champaign, University of Maryland at Baltimore County and at College Park, University of Massachusetts at Amherst, University of Michigan at Ann Arbor, University of North Carolina at Chapel Hill, University of Southern Mississippi, University of Texas at Austin, Wake Forest University, Washington University, Wayne State University.

The students were divided into six teams to work on "industrial mathematics" problems presented by industrial scientists. These were not the neat, well-posed academic exercises typically found in coursework, but were challenging real world problems from industry or applied science. The problems, which were presented to the students on the first day of the workshop, required fresh insights for their formulation and solution. Each group spent the first eight days of the workshop investigating their project and then reported their findings in half-hour public seminars on the last day of the workshop.

The following is a list of the presenters and the projects they brought to the workshop.

- **James M. Nelson** (Boeing Phantom Works) *Autoregistration of Radiographic Projection Views of Known Geometries for Computed Laminography*

- **Zoubeida Ounaies** (NASA Langley Research Center) *High-Performance Polymers Sensors*

- **Yeol Seong** (Bank of Montreal) *Pricing Interest Rate Related Instruments*

- **Farshid Guilak** (Duke University Medical Center) *Modeling of Molecular Diffusion in Articular Cartilage Using Fluorescence Microscopy*

- **Sarah Holte** (Fred Hutchinson Cancer Research Center) *Modeling Control of HIV Infection Through Structured Treatment Interruptions*

- **Damon Christenbury and Yue Zhang** (Michelin North America) *Ring Structure Against Rolling Circular Drum*

These problems represent a broad spectrum of mathematical topics and applications. Although nine days is a short time for a full investigation of some of the aspects of such industrial problems, the reader will observe remarkable progress on all projects.

We, the organizers, strongly believe that this type of workshop provide very valuable non-academic research related experiences for graduate students while contributing to the research efforts of industrial participants. In addition, this type of activity facilitates the development of graduate students' ability to communicate and interact with scientists who are not traditional mathematicians but require and employ mathematical tools in their work. By providing a unique experience of how Mathematics is applied outside Academia, the workshop has helped many students in deciding what kind of career they aspire to. In some cases in past workshops,

this help has been in the form of direct hiring by the participating companies. By broadening the horizon beyond what is usually presented in graduate education, students interested in academic careers also find a renewed sense of excitement about Applied Mathematics.

The success of the workshop was greatly enhanced by active participation in a very friendly atmosphere and almost uninterrupted work during the nine days of attendance. The organizers are most grateful to participants for their contributions. The organizers would like to thank the National Science Foundation, the Center for Research in Scientific Computation and the Department of Mathematics at North Carolina State University for their generous financial support. Special thanks are due to the faculty and staff of the Center for Research in Scientific Computation, the Department of Mathematics and North Carolina State University for the provision of excellent facilities and services. Finally, we would like to thank Brenda Currin, July Duran, Rory Schnell and Vicky Williams for their efforts and help in all administrative matters and Brian Adams and Jim Nealis for providing transportation for the participants.

Pierre Gremaud, Zhilin Li, Ralph Smith, Hien Tran,
Raleigh, 2001.

Report 1

An Inverse Problem in X-Ray Radiography

John Bardsley[1], Valeriy Korostyshevskiy[2], Luis Cueva Parra[3],
Scott La Voie[4], Terry Jo Leiterman[5], Jill Reese[6], Bing Song[7]

Problem Presenter:
James M. Nelson
Boeing Phantom Works

Faculty Consultants:
Pierre A. Gremaud & Zhilin Li

Abstract

The imaging technique of X-ray radiography is useful for the inspection of parts used in military aircraft. Given a source/detector/object configuration, a two-dimensional radiographic image is collected. Using a series of these images, a three-dimensional image of a part is constructed in which defects can be detected. The inverse problem of interest is to estimate, to an arbitrarily high degree of accuracy, the position of the X-ray source and detector system based upon a given object's geometry and its radiographic image. A least squares approach is taken, and the optimization technique DIRECT-1 is applied to the resulting constrained minimization problem. Numerical results are presented. Based upon those results, conclusions are made and possibilities for future work are discussed. We end with an idea for a different approach to finding the solution to the problem.

1.2   Introduction and Motivation

Boeing Corporation manufactures high-performance military aircraft which are used in Class I efforts involving dangerous missions or serious risk to pilot safety. The high integrity of Class I aircraft components is therefore of the utmost importance. Aircraft parts may be manufactured through either forging or mold casting methods. Cast parts have many benefits over forged parts. They are lighter, are easier to produce, and provide a four to one cost benefit. Nevertheless, forged parts are used exclusively because cast parts are difficult to manufacture

---

[1]Montana State University
[2]University of Maryland, Baltimore County
[3]University of Southern Mississippi
[4]East Tennessee State University
[5]University of North Carolina at Chapel Hill
[6]North Carolina State University
[7]Univerity of California, Los Angeles

1

reliably. Minute defects occur for various reasons during the casting process, affecting the strength of the part. Consequently, Class I aircraft require 100% radiographic inspection of certain parts for defects if they are cast. In this process, radiographic X-ray scans are utilized to create an image of a cast part. In Section 1.3 we formulate a mathematical model of the radiographic imaging process. Depending upon the quality of the image, all defect sizes above a certain threshold can be found.

Boeing uses a two million dollar X-ray system to perform the necessary inspection of cast parts. Given that thousands of these parts are produced at one time by vendors who do not have access to such machinery, it is currently infeasible to exclusively use cast parts. Boeing's goal is to provide low-cost imaging software to their manufacturing vendors so that cast parts of a reliable quality can be manufactured in a more cost effective manner. The vendors can set up a virtual radiographic X-ray system that provides a radiographic image of a casting given the locations of the casting, the X-ray source and the detector. Reaching this point in radiographic technology will allow Boeing to cut costs without cutting quality.

The inverse problem of interest is to estimate, to an arbitrarily high degree of accuracy, the position of the X-ray source and detector system based upon a given object's geometry and its radiographic image. A solution of this problem is necessary in order for Boeing to realize its goal of using quality, cost-effective cast parts in the production of Class I aircraft. We formulate the Inverse Problem in Section 1.4. The optimization techniques used in solving the associated minimization problem are discussed in Section 1.5, and in Section 1.6 we present numerical results. Conclusions and possibilities for future work are presented in Section 1.7. In Section 1.8 an alternative approach to the solution of this problem is outlined.

1.3   The Mathematical Model

As X-rays pass through an object they are inhibited by the object's compositional nature. A particular radiographic image shows variations in intensity which correspond to the density and thickness of the material through which the X-ray has passed. This phenomenon is modeled by the equation

$$F(R_{ij}) = e^{-\int_{R_{ij}}^{R_s} \mu(s)ds},$$

where R_s is the position of the X-ray source and is assumed to be a point source; R_{ij} is the position of the $(i,j)^{\text{th}}$ pixel on the detector array, $1 \leq i, j \leq n$; $F(R_{ij})$ is the intensity of the X-ray at the $(i,j)^{\text{th}}$ pixel; μ is a measure of the density of the substance through which the X-rays are traveling; the integration is with respect to arclength along the line from R_{ij} to R_s. See Figures 1.1 and 1.2.

1.4   The Inverse Problem

As stated in Section 1.2, the inverse problem of interest is to estimate, to an arbitrarily high degree of accuracy, the position of the X-ray source and detector system based upon a given object's geometry and its radiographic image. In order to state this problem as simply as possible, we consider the mathematical model given in Section 1.3. We will make the assumption that μ is constant within the object and is zero outside of the object. The above equation can then be written

$$F(R_{ij}) = e^{-\mu b(R_s, R_{ij})},$$

where $b(R_s, R_{ij})$ is the chord length of the segment of the line from R_{ij} to R_s which lies inside of the object being X-rayed. (In Figure 1.1 this is the length of the dashed line segment.) μ is a positive constant. We will further simplify the model by assuming that the source and the detector are fixed in relation to each other.

In order to express b in a more concise manner, we introduce a coordinate system. The center of this coordinate system will be at the center of the detector array, and the detector array will lie in the xy-plane in some fixed orientation. (See Figure 1.1.) The object will also have a fixed initial registration G_{obj} in relation to this fixed coordinate system. We can then obtain any possible radiographic image by rotating and translating G_{obj} in relation to the fixed coordinates. It follows then that b is a function of a translation variable $R = (x, y, z)$ and rotation variables θ and ϕ which are the standard spherical coordinates with respect to our fixed coordinate system. Finally, in our application a non-zero intensity is measured at every pixel which allows for the equation

RADIOGRAPHY SCHEME
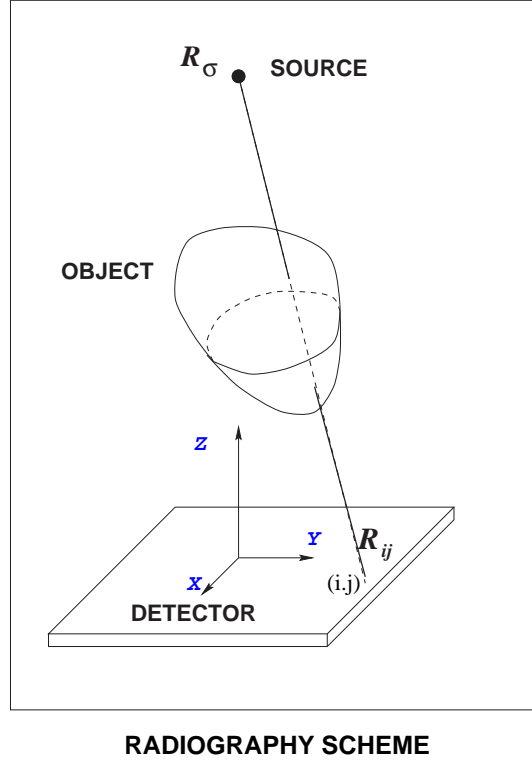
Figure 1.1: Schematic of the Source-Detector System.

$$\mathbf{b}(R, \theta, \phi) = \mathbf{d}$$

where $\mathbf{d}_{ij} = -\frac{1}{\mu} \log(F(R_{ij}))$ and $\mathbf{b}_{ij} = b(R_s, R_{ij})$.

We are now in the position to state the Inverse Problem in its final form. Given a radiographic image $\mathbf{F}$ we want to estimate, to an arbitrarily high degree of accuracy, the corresponding rotation and translation of the object. Equivalently, we want to solve

$$(M) \qquad \min_{R, \theta, \phi} V(R, \theta, \phi)$$

where $V(R, \theta, \phi) = ||\mathbf{d} - \mathbf{b}(R, \theta, \phi)||^2$. Here $|| \cdot || = \frac{1}{n} || \cdot ||_F$ where $|| \cdot ||_F$ is the Frobenius norm for matrices, and n is the number of pixels in one dimension of the radiograph.

1.5   Optimization Techniques

In this section we will concentrate on the optimization problem (M). Several difficulties present themselves in the pursuit of a solution. We seek to minimize our objective function V over the parameter space (R, θ, ϕ). Each five-tuple (R, θ, ϕ) corresponds to a rotation and translation of the object with respect to the fixed coordinates on the detector. Since neither the source nor any points on the detector can be inside of the object, we have choices of (R, θ, ϕ) that are infeasible. Since we have no way of determining these constraints explicitly, we say that they are hidden. When such a problem has hidden constraints it is referred to as a "black-box" optimization problem and standard constrained optimization techniques will not work.

The first approach considered in solving (M) was the use of Quasi-Newton line search algorithms for unconstrained optimization, which have the form:

Quasi-Newton Line Search Algorithm

Figure 1.2: Source Detector System with Corresponding Radiographic Image.

```
k := 0;
(R_0, θ_0, φ_0) := initial guess for the solution (R_*, θ_*, φ_*);
begin iteration
        p_k := Quasi-Newton search direction;
        α_{k+1} := arg min_{α>0} V((R_k, θ_k, φ_k) + α p_k);        % line search
        (R_{k+1}, θ_{k+1}, φ_{k+1}) := (R_k, θ_k, φ_k) + α_{k+1} p_k;        % update approx solution
        k := k + 1;
end iteration
```
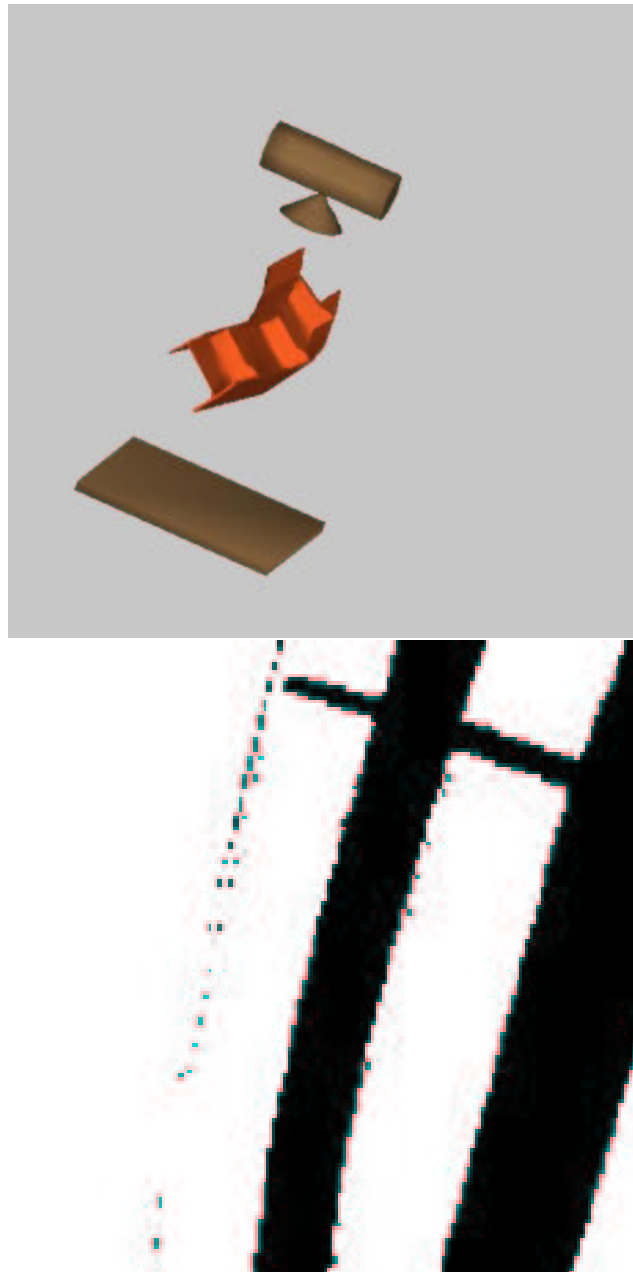
There are three problems with this approach. The first is that in order to use such methods we must ignore the hidden constraints mentioned above. The second is that such methods require gradient information, and since we have no analytic expression for V we cannot compute gradients of V explicitly. Finite differences may be used to create an approximation to the gradient of V, but this can introduce instability, particularly if V is highly oscillatory. Finally, these methods only seek a local, not a global, minimum.

The second approach considered in solving (M) was the use of the DIRECT-1 algorithm [3]. DIRECT-1 requires only function evaluations, allows for hidden constraints, and seeks a global minimum. DIRECT-1 is designed to solve problems of the following form:

Problem: Let $B \subset \Omega = \{\mathbf{x} \in \mathbb{R}^n : a_i \leq \mathbf{x}_i \leq b_i\}$ and $f : B \to \mathbb{R}$ be Lipschitz continuous with constant γ. Let f^* be

$$f^* = \min_{\mathbf{x} \in B} f(\mathbf{x}).$$

Find $\mathbf{x}_{opt} \in B$ such that

$$f_{opt} = f(\mathbf{x}_{opt}) \leq f^* + \epsilon,$$

where ϵ is a given small positive constant.

In our case, $f = V$ and $\mathbf{x} = (R, \theta, \phi)$. Assuming that the object being X-rayed is smooth, the chord length function b, and hence V, is smooth. Further, since V is constant outside of a compact region in $\mathbb{R}^5$, V is Lipschitz. In order to define Ω explicitly, we need upper and lower bounds on our unknowns. Since θ and ϕ are the standard spherical coordinates with respect to our coordinate system, we have $0 \leq \theta \leq 2\pi$ and $0 \leq \phi \leq \pi$. It remains to define upper and lower bounds on the translation variables x, y and z, where $R = (x, y, z)$. This can be done since we have an initial position of the object relative to the source/detector. B is then defined to be the feasible subset of Ω. That is, $B \subset \Omega$ and $\Omega - B$ is the set of infeasible point inside of Ω.

Now that we have stated our problem in the form given above, we are ready to apply the DIRECT-1 algorithm. In order to solve the minimization problem (M), DIRECT-1 iteratively divides the hyper-rectangle Ω into smaller hyper-rectangles. The objective function, in our case V, is evaluated at the center of each of these hyper-rectangles. Based on the values of the objective function at these points, the algorithm continues to divide up Ω in a systematic manner. The hyper-rectangles corresponding to the smaller objective function values are more likely to be divided again. Figure 1.3 provides an example of the division process created by DIRECT-1 for a minimization problem in two dimensions.

1.6 Numerical Results

The numerical tests were performed using a main program (*main.f*), which calls the DIRECT-1 algorithm and its corresponding subroutines for the optimization task. The DIRECT-1 algorithm calls the function evaluation subroutine (*myfunc.f*), which evaluates the function to be optimized. The above codes were written in Fortran 77. The object and source/detector in their initial registration are those of Figure 1.2.

The DIRECT-1 algorithm requires certain parameters to be fixed in advance. Those parameters include the maximum number of function evaluations, in our simulations we chose $100, 200, 1500,$ and $20000,$ the maximum number of iterations, which was fixed at 6000, the ϵ value, which was set to 0.1×10^{-3}, and the bounds for each variable (our problem has 5 variables: rotation θ, rotation ϕ, and translation (x_1, x_2, x_3)).

Two kinds of bounds were chosen for the unknowns. One type of bound corresponds to a large search region for DIRECT-1. This will give us an indication of how the algorithm might work on the general

DIRECT-1

Example for Division created by DIRECT-1

3rd iteration　　　　　　　　　　　4th iteration

5th iteration　　　　　　　　　　　10th iteration
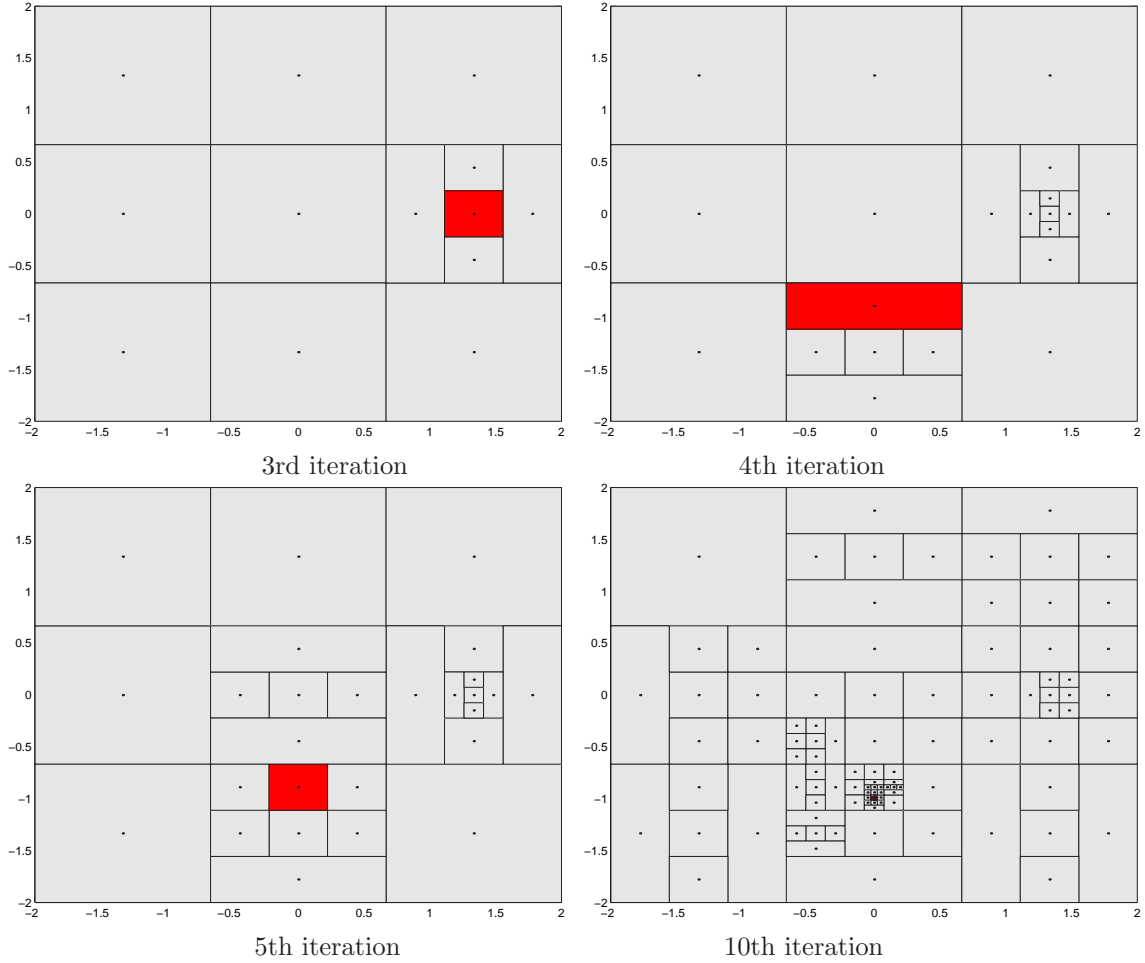
Figure 1.3: The lowest function value has been found within the dark area which is decreasing in size.

problem in which the solution to (M) is not known. The other type of bound restricts the search reagion to a neighborhood of the global minimum. This gives us an indication of how the function behaves near the solution. In our simulations the exact solution is either $\{\theta = 0.0, \phi = 0.0, x_1 = 0.0, x_2 = 0.0, x_3 = 0.0\}$ or $\{\theta = 45.0, \phi = 22.5, x_1 = 1.0, x_2 = 1.0, x_3 = 1.0\}$. For both cases the optimum (minimum) function value is 0.0 .

Other parameters are fixed based on the specific problem. Such parameters include the radiograph size, we will consider both 32 pixels × 32 pixels and 128 pixels × 128 pixels, and the attenuation coefficient, which was chosen to be equal to 12 in order to get a suitable radiograph intensity resolution. In practice the attenuation coefficient corresponds to the material composition of the objet.

Experiments for different test cases are reported in Tables 1-6. Tables 1.1 and 1.2, show the iteration history for 32 pixels × 32 pixels and a small number of function evaluations with two different bounds on the translation variables. Tables 1.3 and 1.4 show the iteration history for a tests problem with a radiograph size of 128 pixels × 128 pixels, a larger number of iterations and broader bounds for the variables. In order to study the behaviour of our objective function in a small region near the solution, we set narrow bounds on the variables about the global minimum. Tables 1.5, 1.6 and 1.7 show the results for three such test cases.

Radiograph size	Bounds	Exact solution
32×32	$40.0 \leq \theta \leq 55.0$	$\theta = 45.0$
# of V-evaluations	$20.0 \leq \phi \leq 30.0$	$\phi = 22.5$
200	$0.0 \leq x_1 \leq 5.0$	$x_1 = 1.0$
Attenuation coefficient	$0.0 \leq x_2 \leq 5.0$	$x_2 = 1.0$
$\mu = 12$	$0.0 \leq x_3 \leq 5.0$	$x_3 = 1.0$
Iteration	**N. of Evaluation**	**V min**
1	11	1.4298218452
2	19	0.9350729985
4	39	0.9166014030
7	85	0.8986268454
10	133	0.8982874120
11	161	0.8972508360
13	209	0.8969325615
Execution time 443.3 seconds	**Minimum value V** 0.8969326	**Computed solution** $\theta = 42.2530864$ $\phi = 28.2098765$ $x_1 = 4.1666667$ $x_2 = 4.1666667$ $x_3 = 2.5000000$

Table 1.1: Iteration history

Conclusions based on these results are given in Section 1.7.

1.7   Conclusions and Comments

In the test cases above, corresponding to Tables 1.1-1.4, we see that DIRECT-1 is creating a sequence of iterates in which the objective function decreases. Nonetheless, in each of these cases the computed solution is far from the exact solution, and the computed minimum is far from the global minimum of 0. In Tables 1.5-1.7, we see large variations in the objective function value corresponding to small variations in R, θ and ϕ. This is particularly evident in Table 1.5, where from iteration 6 to iteration 7 a change in x_2 on the order of 10^{-3} corresponds to a 10^{-1} change in the objective function value. This suggests that our objective function V is highly oscillatory and therefore has a high number of local minima, which may explain the first observation since DIRECT-1 tends to become stuck at local minima. To more firmly establish the nature of V, we suggest fixing any four of the variables and plotting V as a function of the remaining variable. This would also give an indication of how oscillatory V is with respect to each of the variables.

The best possibility for improvement lies in a reformulation of the objective function V. Recall that in order to write V as a function of R, θ and ϕ we introduced a system of coordinates with the origin at the center of the detector array. We then introduced R, θ and ϕ as a translation and rotation of the object G_{obj}. The problem with this formulation is that small changes in the position of G_{obj} may require large changes in R, θ and ϕ. This introduces oscillations into V. In order to alleviate this problem we can instead fix the position of the object while rotating and translating the source/detector system. Since the center of the detector is at the origin, small changes in the position of the source/detector will correspond to small changes in R, θ and ϕ. The resulting objective function will therefore be more smooth.

The smoothness of V is obviously also affected by the smoothness of the object. In Figure 1.2, you can see that due to the reinforcement beams on the object used in the above cases, there are large variations in thickness corresponding to small changes in the position of the object. This introduces further oscillations into the objective function. A smoother object would result in a smoother objective function.

Figure 1.4 represents a schematic of the objective function. This image provides a representation of just how excessively oscillatory V may be for certain complex objects similar to our sample aircraft part. The high

Radiograph size	Bounds	Exact solution
32×32	$40.0 \leq \theta \leq 55.0$	$\theta = 45.0$
# of V-evaluations	$18.0 \leq \phi \leq 30.0$	$\phi = 22.5$
200	$-5.0 \leq x_1 \leq 8.0$	$x_1 = 1.0$
Attenuation coefficient	$-5.0 \leq x_2 \leq 8.0$	$x_2 = 1.0$
$\mu = 12$	$-5.0 \leq x_3 \leq 8.0$	$x_3 = 1.0$
Iteration	**N. of Evaluation**	**V min**
1	11	1.0905552222
2	19	0.6150227595
4	39	0.5572361480
5	49	0.5317911895
8	87	0.5299567485
9	107	0.5292577170
11	145	0.5288763034
12	159	0.5285107697
15	195	0.5234543329
		Computed solution
		$\theta = 49.1666667$
Execution time	**Minimum value V**	$\phi = 28.0000000$
424.0 seconds	0.5234543	$x_1 = 4.3888889$
		$x_2 = 5.83333333$
		$x_3 = 0.0555556$

Table 1.2: Iteration history
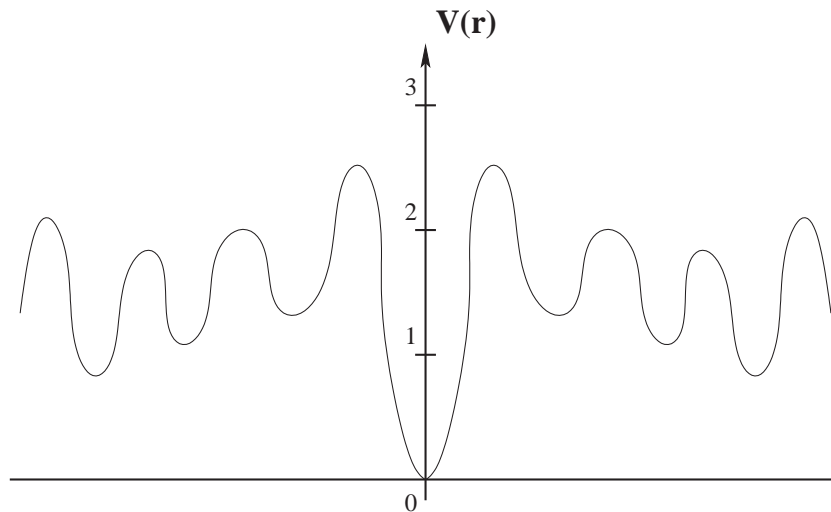

Figure 1.4: A difficult Minimization Problem: Example of an Oscillatory Objective Function.

Radiograph size	Bounds	Exact solution
128×128	$0.0 \leq \theta \leq 360.0$	$\theta = 45.0$
# of V-evaluations	$0.0 \leq \phi \leq 180.0$	$\phi = 22.5$
20000	$-10.0 \leq x_1 \leq 20.0$	$x_1 = 1.0$
Attenuation coefficient	$-10.0 \leq x_2 \leq 20.0$	$x_2 = 1.0$
$\mu = 12$	$-10.0 \leq x_3 \leq 20.0$	$x_3 = 1.0$
Iteration	**N. of Evaluation**	**V min**
1	11	1.3397925812
2	19	1.3229255127
16	75	1.3072716939
17	87	1.2441767734
66	651	1.2417808802
73	757	1.2380874485
75	785	1.2320471406
78	839	1.2265268582
84	925	1.2161344238
88	975	1.2159131715
89	993	1.2158987976
96	1071	1.2002982751
202	2129	1.1863057566
203	2137	1.1772176348
205	2157	1.1654195202
206	2169	1.1619777402
207	2177	1.1580224013
210	2239	1.1506786289
213	2283	1.1505738924
214	2295	1.1504056849
215	2309	1.1501975838
219	2357	1.1501473100
220	2371	1.1500792379
221	2381	1.1500340087
		Computed solution
		$\theta = 224.6090535$
Execution time	**Minimum value V**	$\phi = 149.1495199$
23.03×10^4 seconds	1.1500340	$x_1 = 19.4261545$
		$x_2 = 17.5925926$
		$x_3 = 9.9428441$

Table 1.3: Iteration history

Radiograph size	Bounds	Exact solution
128×128	$-90.0 \leq \theta \leq 270.0$	$\theta = 0.0$
# of V-evaluations	$-1.0 \leq \phi \leq 180.0$	$\phi = 0.0$
1500	$-38.0 \leq x_1 \leq 40.0$	$x_1 = 0.0$
Attenuation coefficient	$-38.0 \leq x_2 \leq 40.0$	$x_2 = 0.0$
$\mu = 12$	$-38.0 \leq x_3 \leq 40.0$	$x_3 = 0.0$
Iteration	**N. of Evaluation**	**V min**
1	11	1.5236727259
3	35	1.4740824756
7	105	1.4664192523
8	115	1.4633327454
11	165	1.4624315571
12	173	1.4596045527
14	193	1.4588382087
75	377	1.4580200589
102	543	1.4401144965
104	559	1.4369518683
106	589	1.4355538157
107	607	1.4303820943
108	625	1.4299838306
110	657	1.4272165411
111	669	1.4258087342
113	705	1.3999648750
		Computed solution
		$\theta = -30.4938272$
Execution time	**Minimum value V**	$\phi = 121.5288066$
32280 seconds	1.3999649	$x_1 = -15.6913580$
		$x_2 = 9.6666667$
		$x_3 = 0.0370370$

Table 1.4: Iteration history

Radiograph size	Bounds	Exact solution
32×32	$44.99900 \leq \theta \leq 45.00100$	$\theta = 45.0$
# of V-evaluations	$22.49900 \leq \phi \leq 22.50100$	$\phi = 22.5$
100	$0.99900 \leq x_1 \leq 1.00100$	$x_1 = 1.0$
Attenuation coefficient	$0.99900 \leq x_2 \leq 1.00100$	$x_2 = 1.0$
$\mu = 12$	$0.90000 \leq x_3 \leq 1.10000$	$x_3 = 1.0$
Iteration	**N. of Evaluation**	**V min**
1	11	0.0000000008
Execution time 44.35 seconds	**Minimum value V** 0.0000000	**Computed solution** $\theta = 45.0006667$ $\phi = 22.5000000$ $x_1 = 1.0000000$ $x_2 = 1.0000000$ $x_3 = 1.0000000$

Eval.	θ	ϕ	x_1	x_2	x_3	V
1	45.0000000	22.5000000	1.0000000	1.0000000	1.0000000	0.0000000
2	45.0006667	22.5000000	1.0000000	1.0000000	1.0000000	$7.8078432 \times 10^{-10}$
3	44.9993333	22.5000000	1.0000000	1.0000000	1.0000000	$7.8509288 \times 10^{-10}$
4	45.0000000	22.5006667	1.0000000	1.0000000	1.0000000	$1.60374167 \times 10^{-8}$
5	45.0000000	22.4993333	1.0000000	1.0000000	1.0000000	$1.64844689 \times 10^{-8}$
6	45.0000000	22.5000000	1.00066667	1.0000000	1.0000000	0.317432001
7	45.0000000	22.5000000	0.999333333	1.0000000	1.0000000	1.8570821×10^{-7}
8	45.0000000	22.5000000	1.0000000	1.00066667	1.0000000	2.0112183×10^{-7}
9	45.0000000	22.5000000	1.0000000	0.999333333	1.0000000	0.317423896
10	45.0000000	22.5000000	1.0000000	1.0000000	1.00066667	$5.26005106 \times 10^{-9}$
11	45.0000000	22.5000000	1.0000000	1.0000000	0.999333333	$5.24506572 \times 10^{-9}$
12	45.0006667	22.5006667	1.0000000	1.0000000	1.0000000	$1.75096586 \times 10^{-8}$
13	45.0006667	22.49993333	1.0000000	1.0000000	1.0000000	$1.63160925 \times 10^{-8}$
14	45.0006667	22.5000000	1.00066667	1.0000000	1.0000000	0.317433385
15	45.0006667	22.5000000	0.999333333	1.0000000	1.0000000	$1.79039366 \times 10^{-7}$
16	45.0006667	22.5000000	1.0000000	1.00066667	1.0000000	$1.98505329 \times 10^{-7}$
17	45.0006667	22.5000000	1.0000000	0.999333333	1.0000000	0.317425243
18	45.0006667	22.5000000	1.0000000	1.0000000	1.00066667	$6.07632611 \times 10^{-9}$
19	45.0006667	22.5000000	1.0000000	1.0000000	0.999333333	$6.00445293 \times 10^{-9}$

Table 1.5: Iteration history

Radiograph size	Bounds	Exact solution
128×128	$-0.50 \leq \theta \leq 1.40$	$\theta = 0.0$
# of V-evaluations	$-0.55 \leq \phi \leq 1.35$	$\phi = 0.0$
100	$-0.20 \leq x_1 \leq 1.00$	$x_1 = 0.0$
Attenuation coefficient	$-0.20 \leq x_2 \leq 1.00$	$x_2 = 0.0$
$\mu = 12$	$-0.20 \leq x_3 \leq 1.00$	$x_3 = 0.0$
Iteration	N. of Evaluation	V min
1	11	2.4430140225
2	19	2.3767842301
3	25	2.2676770985
4	29	1.2412734055
6	43	0.9637743787
8	71	0.9488465682
9	87	0.9271115115
10	95	0.7452087381
		Computed solution
		$\theta = 0.1685185$
Execution time	Minimum value V	$\phi = -0.1629630$
1901 seconds	0.7452087	$x_1 = 0.0000000$
		$x_2 = 0.0000000$
		$x_3 = 0.0444444$

Eval.	θ	ϕ	x_1	x_2	x_3	V
1	0.45	0.4	0.4	0.4	0.4	2.76729347
2	1.08333333	0.4	0.4	0.4	0.4	2.68744142
82	0.238888889	-0.162962963	0.0444444444	0.0000	0.0000	1.20829843
83	0.238888889	-0.162962963	-0.0444444444	0.0000	0.0000	1.23736547
84	0.238888889	-0.162962963	0.0000	0.0444444444	0.0000	2.18148961
85	0.238888889	-0.162962963	0.0000	-0.0444444444	0.0000	2.19257007
86	0.238888889	-0.162962963	0.0000	0.0000	0.0444444444	1.03721191
87	0.238888889	-0.162962963	0.0000	0.0000	-0.0444444444	1.02558313
88	1.08333333	1.03333333	0.0000	0.8000	0.0000	2.33425951
89	-0.183333333	1.03333333	0.0000	0.8000	0.0000	2.29927099
90	0.168518519	-0.162962963	0.0444444444	0.0000	0.	1.00515552
91	0.168518519	-0.162962963	-0.0444444444	0.0000	0.0000	1.29581035
92	0.168518519	-0.162962963	0.0000	0.0444444444	0.0000	2.16171059
93	0.168518519	-0.162962963	0.0000	-0.0444444444	0.0000	2.16511212
94	0.168518519	-0.162962963	0.0000	0.0000	0.0444444444	0.745208738
95	0.168518519	-0.162962963	0.0000	0.0000	-0.0444444444	0.994938122
96	1.08333333	0.4000	0.0000	0.8000	0.4000	2.34683152

Table 1.6: Iteration history

Radiograph size	Bounds	Exact solution
128×128	$-0.25 \le \theta \le 1.20$	$\theta = 0.0$
# of V-evaluations	$-0.25 \le \phi \le 1.20$	$\phi = 0.0$
100	$-0.15 \le x_1 \le 1.00$	$x_1 = 0.0$
Attenuation coefficient	$-0.15 \le x_2 \le 1.00$	$x_2 = 0.0$
$\mu = 12$	$-0.15 \le x_3 \le 1.00$	$x_3 = 0.0$
Iteration	**N. of Evaluation**	**V min**
1	11	2.5640839284
2	19	2.2814250644
3	25	2.2612233248
5	41	2.2335693356
7	69	2.2280693389
8	87	2.1462814256
		Computed solution
		$\theta = 0.9583333$
Execution time	**Minimum value V**	$\phi = -0.0083333$
1882 seconds	2.1462814	$x_1 = 0.0416667$
		$x_2 = 0.425$
		$x_3 = 0.0416667$

Table 1.7: Iteration history

number of local minima cause the search for the global minimum to become time-consuming and difficult.

By rotating the source/detector and using a smoother object we believe the resulting minimization problem will have much better conditioning. Our suggestion for a course of action is to implement these changes, applying DIRECT-1 with the new objective function V. If this course of action proves successful, then one can move on to less smooth objects.

Another other idea along similar lines is to use DIRECT-1 to narrow in on a local minimum and then use a different algorithm, IFFCO for example, to find the solution. IFFCO (Implicit Filtering for Constrained Optimization) is an algorithm which utilizes implicit filtering to solve problems with bound constraints as well as many local minima [1]. We could also use a different norm in the formulation of the minimization problem based upon matrix analysis of the **d** and **b**(R, θ, ϕ) matrices. Finally, polar coordinates could be used for the translation as well. This would make for easier determination of the bounds on the variables, although it most likely would not improve the conditioning of the objective function.

1.8 Another Approach

The idea of using computers to obtain radiographs originated in the late sixties, when in 1967 Sir Godfrey Newbold Hounsfield started working on the first computerized axial tomography (CAT) scanner. He mainly concentrated on obtaining a cross-sectional planar image of an organ or body using the information from a series of axial transverse X-ray scans – a form of tomography.

Approximately at the same time, people started working on the problem of reconstructing a 3D image from the set of 2D projections (see [9]), and different approaches were suggested. Ramanachandran ([10]) et al. employed the convolution theorem for the inverse of the product of Fourier transforms. Lanzavecchia et al. (see [11, 12]) applied a concept of the Radon transform in three-dimensional space. If the image intensity is given by f and a 2D projection is given by f^*, which appears to be the Radon transform of f, then the fundamental result that was used is the following. The 1D Fourier transform of a projection along the radial direction equals the 3D Fourier transform of image intensity, or, symbolically, $\mathcal{F}_1[\check{f}] = \mathcal{F}_3[f]$. This result is based on the *Central section theorem*. For the general case and examples see [13].

Acknowledgments

Bibliography

[1] T. Kelley, *Implicit Filtering.*
http://www4.ncsu.edu/eos/users/c/ctkelley/www/iffco.html

[2] M. Dahlbom, *Computed Tomography - CT,* Lecture notes, Spring 2001.
http://oden.nuc.ucla.edu/rs200b/lecture_notes/lecture5/ct1.html

[3] J. Gablonsky, *DIRECT version 2.0,* Fortran code.
http://www4.ncsu.edu/ jmgablon/

[4] S. Gondrom and S. Schropfer, *Digital computed laminography and tomosynthesis - functional principals and industrial applications,* NDT.net, July 1999, Vol. 4, No. 7.

[5] *Image Projections and the Radon Transform.*
http://www.owlnet.rice.edu/ elec431/projects96/DSP/bpanalysis.html

[6] A. Kalukin and V. Sankaran, *Three-Dimensional Visualization of Multilayered Assemblies using X-Ray Laminography,* IEEE Transactions on Components, Packaging, and Manufacturing Technology, September 1997.

[7] H. Kopka and P.W. Daly, *A Guide to $\LaTeX\,2_\varepsilon$: Document Preparation for Beginners and Advanced Users* -2nd ed., Addison-Wesley Publishing Company, New York, 1995.

[8] J. Nelson, *Synthradiograph.f,* Fortran code.

[9] R.A. Crowther, D.J. DeRosier, A. Klug, F.R.S. *The reconstruction of a three-dimensional structure from projections and its applications to electron microscopy,* Proceedings of Royal Society, London, A. 317, 1970.

[10] G.N. Ramanachandran, A.V. Lakshminarayanan, *Three-dimensional Reconstruction from Radiographs and Electron Micrographs: Application of Convolutions instead of Fourier Transform,* Proceedings of National Academy of Sciences, USA, Vol. 68, No. 9, 1971.

[11] S. Lanzavecchia, P. Bellon, *Fast computation of 3D Radon transform via a direct Fourier method,* Bioinformatics, Vol. 14, no. 2, 1998.

[12] S. Lanzavecchia, P. Bellon, M. Radermacher, *Fast and Accurate Three-dimensional Reconstruction from Projections with Random Orientations via Radon Transform,* Journal of Structural Biology, 128, 1999.

[13] Earl J. Kirkland, *Advanced computing in electron microscopy,* New York: Plenum Press, 1998.

Report 2

High-Performance Polymer Sensors

Gregory Daspit[1], Cynthia Martin[2], Jae-Hong Pyo[3], Cassandra Smith[4], Hansun To[5]

Problem Presenter:
Zoubeida Ounaies
ICASE, NASA Langley Research Center

Faculty Mentors:
Khaled Furati & Ralph Smith

Abstract

Due to their high sensitivity to voltage, piezoelectric polymers have excellent sensor characteristics which has led to their consideration for medical, aerospace and aeronautic applications. The desire to develop a sensor and/or actuator requiring relatively low voltage led to the evaluation and modeling of a unimorph piezoelectric polymer construction. We developed a model based on the Newtonian principles of force and moment balancing to predict displacement at various voltage levels. The model was compared to experimental data and was found to accurately characterize displacements within the considered regimes.

2.1   Introduction

The Institute for Computer Applications in Science and Engineering (ICASE) in Hampton, Virginia, is a research institute at NASA Langley Research Center (NASA LaRC) which fosters collaboration between its staff, NASA scientists and engineers, and research communities in universities and related industries.

Zoubeida Ounaies, a Senior Staff Scientist at ICASE, was invited to the workshop to present a current problem involving high-performance piezoelectric polymers for aerospace application. NASA LaRC is interested in developing piezoelectric polymer unimorphs to be employed as low power, light weight, wiper mechanisms for rover exploration in unmanned missions. Another NASA application focuses on synthetic jets for aircraft wings where the devices are employed as both sensors and actuators to affect the state of flows around the aircraft. There are other important possible applications in the biomedical field including artificial muscle actuators and actuator implants to stimulate tissue and bone growth.

Figure 1 depicts a schematic of the unimorph configuration considered in this project. A top layer of electrically active, anisotropic polyvinylidene fluoride (PVDF) and a bottom layer of electrically inactive,

---

[1]University of Alabama at Birmingham
[2]Texas Tech University
[3]University of Maryland at College Park
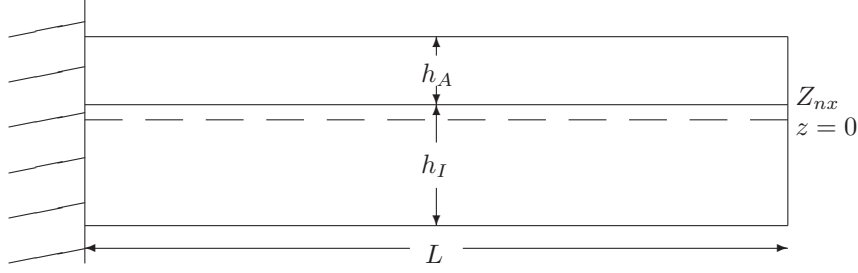[4]North Carolina State University
[5]Temple University

Figure 2.1: Longitudinal cross section of clamped unimorph.

isotropic polyimide are bonded together with an adhesive layer. We assume the device to be perfectly clamped as shown, where $x = 0$ and free at the other end where $x = L$. Voltage is applied on the outside of the clamps which are coated with conductive paint. The goal of the project is to develop a model that will predict the free-tip displacement as a function of input voltage given the piezoelectric and elastic properties of the layers.

We first consider the system depicted in Figure 1 with thickness $h = h_A + h_I$ whose h_A denotes the thickness of the active PVDF layer and h_I is the thickness of the inactive layer. To simplify, we assume that the thickness of the adhesive layer bonding the two is negligible. We realize that upon application of our model a small difference in prediction can be attributed to this assumption.

Throughout the modeling process, it was necessary to make a variety of assumptions. Two we have alluded to: the unimorph being perfectly clamped and the adhesive layer being negligible. There are other assumptions we need to make in order to begin deriving a model. We assume small displacements, that $h_I \neq h_A$, temperature is fixed at a room temperature of $25°$C, no saturation or limit on the movement of the active layer due to increased voltage, initial flat geometry, that both expansion of the piezoelectric layer upwards and along its width is negligible due to the anisotropic property of PVDF, and that there exists a neutral axis, Z_{ns}, in the strip where stress is zero.

Another area where we choose to assume linearity is in the stress-strain behavior of the materials. When these materials have a force (stress) exerted upon them, they will deform (strain) by an amount proportional to the magnitude of the stress. This proportionality constant or slope of the stress-strain curve, is often referred to as the elastic modulus or Young's modulus if in the lengthwise direction. Although the relationship between stress and strain need not always be linear, we assume that operating conditions are within the linear limits of the material and hence we can use Hooke's Law wich posits a linear relation between stress and strain.

2.2   The Model

Modeling a unimorph poses a change to previous models due to its two-layer construction. Since the two layers can be of different thickness and materials there are three things to consider: the asymmetry of the thickness, the different densities, and the different Young's moduli.

Keeping this in mind we considered thin beam theory. There are two modeling approaches that we can look at. The first approach is a Newtonian approach, which is a force and moment balancing approach. The second is a Hamiltonian approach, which deals with energy principles.

We will look at force balancing through the longitudinal direction. Let Δx be the change in displacement and let w be the vertical displacement force. Force balancing then yields

$$\int_x^{x+\Delta x} \rho \frac{\partial^2 w}{\partial t^2} = -S(x + \Delta x) + S(x) + \int_x^{x+\Delta x} f(t,s)ds - \gamma \int_x^{x+\Delta x} \frac{\partial w}{\partial t} ds \qquad (2.2.1)$$

where ρ is the material density, f is an external force (e.g., wind, grain of sand/obstruction), γ is an external damping constant and s is a shear resultant. Dividing by Δx and taking $\Delta x \to 0$, yields

$$\rho \frac{\partial^2 w}{\partial t^2} + \gamma \frac{\partial w}{\partial t} + \frac{\partial s}{\partial x} = f(t,x). \qquad (2.2.2)$$
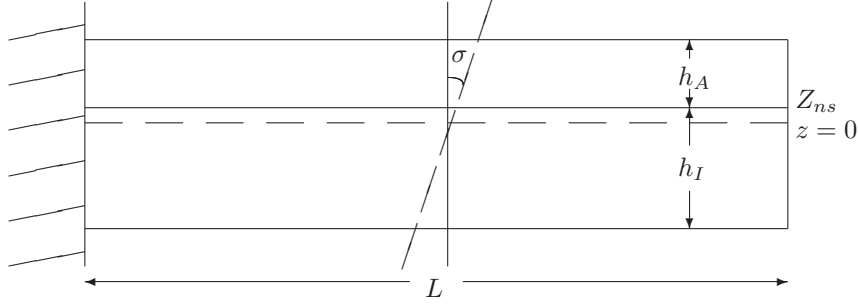
Figure 2.2: Assumed stress distribution for the unimorph.

We then consider the balance of moments. Letting M denote the resulting, moment balancing yields

$$M(x + \Delta x) - M(x) - S(x + \Delta x)\Delta x + \int_x^{x+\Delta x} f(t, s)(s - x)ds = 0. \tag{2.2.3}$$

From (2.3) divide by Δx and take $\Delta x \to 0$, to get

$$\frac{\partial M}{\partial x} - S = 0. \tag{2.2.4}$$

Combining (2.2) and (2.4) yields

$$\rho\frac{\partial^2 w}{\partial t^2} + \gamma\frac{\partial w}{\partial t} + \frac{\partial^2 M}{\partial x^2} = f(t, x). \tag{2.2.5}$$

The bending moment is specified by

$$M \approx \frac{1}{R} = \frac{w''}{[1 + (w')^2]^{3/2}} \approx w''(t, s) \tag{2.2.6}$$

where R denotes the radius of curvature and we use the notation $w' = \frac{\partial w}{\partial x}$ and $\dot{w} = \frac{\partial w}{\partial t}$. We then need to compute the proportionality constant. First, consider the constitutive relations, $F = kx$ (Hooke's law). Consider a (active/inactive) unimorph with an active layer of thickness h_A, Young's modulus Y_A and a density ρ_A. The inactive layer has thickness h_I, Young's modulus Y_I and a density ρ_I. The bonding layer between active/inactive layers is neglected, and we assume there is a perfect bonding. The coefficient d_{31} (see Appendix) is a proportionality constant which is in the thickness direction (z) and the lateral direction (x). This implies the strain e, can be expressed as

$$e = \frac{1}{Y_A}\sigma + d_{31}E, \tag{2.2.7}$$

where σ denotes the applied stress and E is the applied electric field. Replacing E by V(Voltage)/h_A and solving for σ, stress (2.7) becomes

$$\sigma = Y_Ae - Y_A\frac{d_{31}}{h_A}V. \tag{2.2.8}$$

To determine the bending moment, M, for the active layer, we integrate the stress over the active thickness which yields $M = -\int_{h_A} \sigma z dz$.

For the uniform beam case, i.e., $h_A = h_I = \frac{h}{2}$ and $Y_A = Y_I = Y$, $V = 0$, this yields

$$M = \frac{Yh^3b}{12}\frac{\partial^2 w}{\partial x^2} = YI\frac{\partial^2 w}{\partial x^2} \tag{2.2.9}$$

where b is a width of the beam. However, we know that in general $h_A \neq h_I$ and $Y_A \neq Y_I$ thus making it necessary to compute the position of the neutral plane axis, z_{ns}, an effective longitudinal axis through our device where stress is 0. Substituting (2.9) into (2.5) yields the Euler–Bernoulli Beam equation

$$\rho\frac{\partial^2 w}{\partial t^2} + \gamma\frac{\partial w}{\partial t} + YI\frac{\partial^4 w}{\partial x^4} = f(t, x). \tag{2.2.10}$$

We now need to consider boundary conditions. On the left the beam is clamped so we assume there is no displacement change and zero slope

$$w(t, 0) = w'(t, 0) = 0. \tag{2.2.11}$$

For the right we have the natural boundary conditions corresponding to the free end. We also know $M(t, L) = S(t, L) = 0$ which gives

$$w''(t, L) = w'''(t, L) = 0. \tag{2.2.12}$$

The initial condition corresponding to the position is $w(0, x) = w_0(x)$ and initial condition corresponding to the velocity is $w'(0, x) = w_1(x)$.

2.3 Derivation of Parameters

As noted previously, the two materials have different thicknesses, densities, and Young moduli. To compensate for this we need to find the effective linear density, the neutral axis, and the effective Young modulus of the entire unimorph.

Density: Given ρ_A, ρ_I as the densities of the active and the inactive layer, respectively, the linear density for the unimorph is

$$\rho = \rho_A h_A b + \rho_I h_I b. \tag{2.3.1}$$

Neutral Axis: From (2.8), it follows that in the absence of an applied voltage, the stress is given by $\sigma = Ye$ whose $e = kz$ for a uniform, homogeneous beam. Furthermore, moment balancing yields

$$M + \int_A \sigma z \, dz = 0. \tag{2.3.2}$$

Combining (3.2) with (2.7) and (2.9), we get $k = -\frac{1}{YI}A$, where

$$I = \int_A z^2 \, dA = \frac{h^3 b}{12} \quad \text{and} \quad e = -\frac{M}{YI} z. \tag{2.3.3}$$

Now we have to consider the relationship between the moment and the responding curvature shown in Figure 3.

Since the strain is defined to be the infinitesimal change in length over original length,

$$e = \frac{du}{dx} \tag{2.3.4}$$

where u is the displacement in the lateral direction. Moreover, combining (3.2) and (3.3),

$$M = YI \frac{\partial^2 w}{\partial x^2}. \tag{2.3.5}$$

From the force balancing equation, $\int_A \sigma \, dA = 0$, where A is the cross section area, combining (2.7) and (3.5) yields

$$\int_{-h_I}^{0} Y_I \frac{(z - z_{ns})}{R} dz + \int_{0}^{h_A} Y_A \frac{(z - z_{ns})}{R} dz = 0 \tag{2.3.6}$$

where R is the radius of curvature due to bending. Simplifying we can solve for our neutral axis which is

$$z_{ns} = \frac{Y_A h_A^2 - Y_I h_I^2}{2(Y_A h_A + Y_I h_I)}. \tag{2.3.7}$$

Young's modulus Y From (3.2) and combining (2.8) and the fact $e = kz$, Y can be determined by

$$Y = \frac{\left[(h_I + z_{ns})^3 - z_{ns}^3\right] Y_I + \left[(h_A - z_{ns})^3 + z_{ns}^3\right] Y_A}{(h_A - z_{ns})^3 + (h_I + z_{ns})^3}. \tag{2.3.8}$$

Since the materials we are dealing with are visco-elastic, there exists structural dampening. To decrease the computational complexities we used the Kelvin-Voigt model of dampening which introduces a coefficient c_D. To find the moment due to an applied voltage, V, we use the coefficient, $-\frac{d_{31}}{h_A} Y_A$. Thus, the force from (2.8) is

$$\sigma = Ye - \frac{d_{31}}{h_A} Y V(t) + c_D \dot{e}. \tag{2.3.9}$$

For PVDF/polyimide unimorphs, the displacement in the z direction and the electric field E applied through the thickness, and the damping effect are then modeled by the following differential equation

$$\rho \frac{\partial^2 w}{\partial t^2} + \gamma \frac{\partial w}{\partial t} + Y \frac{\partial^4 w}{\partial x^4} + c_D \frac{\partial^5 w}{\partial x^4 \partial t} = f(t, x) + \frac{\partial^2}{\partial x^2} (K_B V(t) \mathcal{X}_A(x)) \tag{2.3.10}$$

where $K_B = b \int_0^{h_A} Y_A \frac{d_{31}}{h_A} (z - z_{ns}) dz$ and $\mathcal{X}_A(x)$ is a characteristic function that is 1 on the region covered by the piezoelectric layer and 0 elsewhere. We have essential boundary conditions $w(t, 0) = w'(t, 0) = 0$ and natural boundary conditions $w''(t, L) = w'''(t, L) = 0$.

2.4 Numerical Method

In order to numerically solve the differential equation (3.11), we have to first consider a weak form of the model. Either Hamiltonian principles or integration by parts yields

$$\int_0^L \rho \frac{\partial^2 w}{\partial t^2} \phi \, dx + \int_0^L \gamma \frac{\partial w}{\partial t} \phi \, dx + \int_0^L Y \frac{\partial^2 w}{\partial x^2} \frac{\partial^2 \phi}{\partial x^2} \, dx + \int_0^L C_D \frac{\partial^3 w}{\partial x^2 \partial t} \frac{\partial^2 \phi}{\partial x^2} \, dx$$
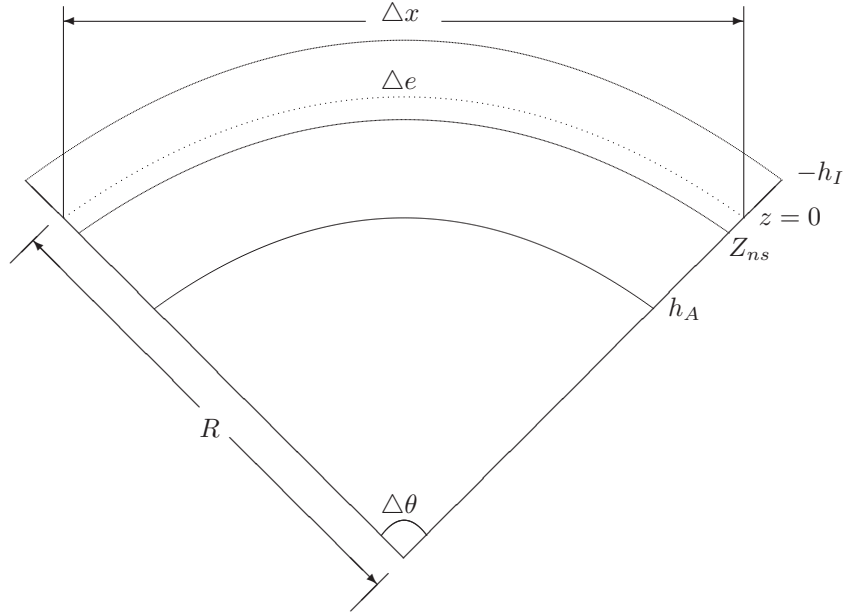

Figure 2.3: Coordinate system and reaction of unimorph under bending

$$= \int_0^L f(t,x)\phi dx + \int_0^L K_B V(t)\frac{\partial^2 \phi}{\partial x^2}dx$$

$$(2.4.1)$$

for all test functions $\phi \in H_L^2(0,L) = \phi \in H^2(0,L) : \phi(0) = \phi'(0) = 0\}$ To approximate the solutions, we employ the basis $\{\phi_i\}_{i=1}^{N+1}$ where

$$\phi_1(x) = \hat{\phi}_0(x) - 2\hat{\phi}_{-1}(x) - 2\hat{\phi}_1(x)$$

$$\phi_j(x) = \hat{\phi}_j(x), j = 2, ..., N+1$$

with the canonical bassis functions ϕ_j given by

$$\hat{\phi}_j(x) = \frac{1}{h^3}\begin{cases} (x - x_{j-2})^3, & x \in [x_{j-2}, x_{j-1}) \\ h^3 + 3h^2(x - x_{j-1}) + 3h(x - x_{j-1})^2 - 3(x - x_{j-1})^3, & x \in [x_{j-1}, x_j) \\ h^3 + 3h^2(x_{j+1} - x) + 3h(x_{j+1} - x)^2 - 3(x_{j+1} - x)^3, & x \in [x_j, x_{j+1}) \\ (x_{j+2} - x)^3, & x \in [x_{j+1}, x_{j+2}) \\ 0 & \text{otherwise} \end{cases}$$

$$(2.4.2)$$

Several representative basis functions are depicted in Figure 4. Approximate solutions are then found through the expansion

$$W^N(t,x) = \sum w_j(t)\phi_j(x)$$

and the finite-dimensional space of test functions is taken to be $H^N = \text{span}\{\phi_i\}$. Projection of the problem into H^N yields

Therefore, from (4.1) the weak form becomes the following:

$$\sum_{j=1}^{N+1}\left[\int_0^L \rho\phi_i\phi_j dx\right]\ddot{w}_j(t) + \sum_{j=1}^{N+1}\left[\int_0^L \gamma\phi_i\phi_j dx\right]\dot{w}_j(t) + \sum_{j=1}^{N+1}\left[\int_0^L Y\phi_j''\phi_i'' dx\right]w_j(t) + \sum_{j=1}^{N+1}\left[\int_0^L C_D\phi_i''\phi_j'' dx\right]\dot{w}_j(t)$$

$$= \int_0^L f(t,x)\phi_i dx + \int_0^L K_B V(t)\phi_i'' dx.$$
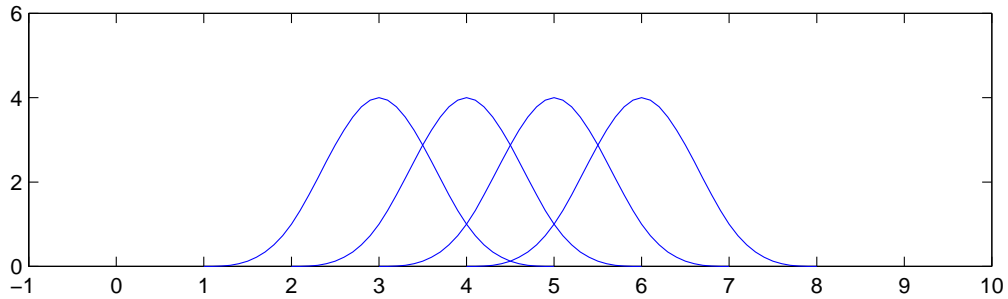
$$(2.4.3)$$

Figure 2.4: Spline basis functions

for all $\phi_i \in H^N$. This can then be formulated as the vector-valued differential equation

$$M\ddot{w}(t) + C\dot{w}(t) + Kw(t) = f(t) + BV(t) \tag{2.4.4}$$

where

$$w(t) = \begin{bmatrix} w_1(t) \\ \vdots \\ w_{N+1}(t) \end{bmatrix} \tag{2.4.5}$$

and

$$\begin{array}{rcl}
[K]_{ij} & = & \int_0^L Y\phi_i''\phi_j'' dx \tag{2.4.6} \\[2mm]
[M]_{ij} & = & \int_0^L \rho\phi_i\phi_j dx \tag{2.4.7} \\[2mm]
[C]_{ij} & = & \int_0^L \gamma\phi_i\phi_j dx + \int_0^L c_D\phi_i''\phi_j'' dx \tag{2.4.8} \\[2mm]
[B]_{ij} & = & \int_0^l K_B\phi_i'' dx \tag{2.4.9}
\end{array}$$

Set

$$y(t) = \begin{bmatrix} w_1(t) \\ \vdots \\ w_{N+1}(t) \\ \dot{w}_1(t) \\ \vdots \\ \dot{w}_{N+1}(t) \end{bmatrix} = \begin{bmatrix} w(t) \\ \dot{w}(t) \end{bmatrix}. \tag{2.4.10}$$

Putting (4.8) and (4.9) into (4.6), we get

$$\dot{y}(t) = \begin{bmatrix} \dot{w}(t) \\ \ddot{w}(t) \end{bmatrix} = \begin{bmatrix} 0 & I \\ -M^{-1}K & -M^{-1}C \end{bmatrix} \begin{bmatrix} w(t) \\ \dot{w}(t) \end{bmatrix} + \begin{bmatrix} 0 \\ M^{-1}f(t) \end{bmatrix} + \begin{bmatrix} 0 \\ M^{-1}B \end{bmatrix} V(t) \tag{2.4.11}$$

or

$$\dot{y}(t) = Ay(t) + BV(t) + F(t). \tag{2.4.12}$$

2.5 Experimental Validations

2.5.1 Commentary on the Data

The experimental data used to evaluate the model was measure by Zoubeida Ounaies, NASA LaRC, and included tip displacements obtained with 25, 50, 75, 100, and 150 volt inputs. Two sets of data at 50 volts were taken using different displacement sensors due to range limitations in an effort to determine if the displacement sensors produced consistent data.

The 150 volt data was not used as it showed signs of saturation and our model was developed on the assumption of no nonlinear saturation.

The data was collected at 1 Hz and contained approximately two cycles. We chose to make our comparison to second cycle data and used the maximum measured voltage (converted from the electric field) as the driving force in our model.

2.5.2 Parameters

Table 1 summarizes the parameters measured experimentally and those used in the model. The parameters used in the model were chosen in the process of hand fitting predictions of the model to the experimentally obtained displacement versus voltage curves for a 100 volt driving level. As can be noted from Table 1 our chosen values are all within experimentally valid intervals except d_{31}. Due to the difficulty of measuring d_{31},

it can be measured to within 20% of the mean. This generates an interval about the mean of the data of 20 to 30 pC/N, which does include the d_{31} employed in the model.

By far the most sensitive parameter was d_{31}, our least well known value. Our least sensitive parameter was γ, the coefficient of "air" dampening. The model also appeared to have a greater than predicted sensitivity to certain geometric values, in some cases changing the shape of the curve when the value was changed within experimental uncertainty ($1mil = 25.4\mu m = 25.4x10^{-6}m$).

At this time it was noted that there were two adhesive layers. We decided to consider the assumption that they were negligible. The adhesive layers have approximate thickness of $\frac{1}{4}mil = 6.35\mu m$. Since they were outside the electric field and of the same category of material as the inactive layer, we included their thickness in the inactive height, h_I. This is reasonable due to the aforementioned fact that both the adhesive and inactive layers are polyimides. While it is possible that the adhesive and solid polyimides would have different structures and hence densities and Young's modulus, it should not be appreciably compared to the other assumptions.

2.5.3   Model Predictions

Once the parameter values were selected for the unimorph driven at 100 volts, we then predicted the tip displacement verses voltage curves for the 25 volt, 50 volt, and 75 volt driving levels. These plots are shown in Figure 5 with one cycle of experimental values and the predicted model values. Comparing these generated curves to the experimentally measured curves suggested that we had successfully developed a linear model that accurately predicts tip displacement at multiple voltage levels. The reason ellipses were generated and not lines are due to structural dampening as modeled by the Kelvin-Voigt parameter, c_D

2.5.4   Characteristics of Unimorph (free tip displacement)

One of the characteristics of a unimorph is the variation of the maximum tip displacement with respect to application of voltage when no outside forces are involved. Free tip displacement should be proportional to the driving voltage. This can be seen by doing a least squares fit to a line (polyfit(V,D,1) in Matlab) of the points (driving voltage, range of tip displacement) for each voltage level. The residue of the experimental points when fit by least squares is 9.87×10^{-6} and the model's residue is 7.15×10^{-7}. The two lines resulting from the least squares fit are:

$$D_{model} = 0.1978 \times 10^{-5} \, V_{model} + 0.0678 \times 10^{-5}$$

$$D_{exp} = 0.1939 \times 10^{-5} \, V_{exp} + 0.0635 \times 10^{-5}$$

In Figure 6, the experimental data values are plotted (diamonds), D_{exp} (the line fit to the data points) is the dashed line, and D_{model} (the line predicted by the model) is the solid line.

To compare experimental values and those suggested by the model, it is logical to compare the proportionality constant (i.e., the slope). The slope of the line fit to the data is 0.1939×10^{-5}. While the slope of

Symbol	Units	Experimental Range	Used in Model	Meaning
L	m	$0.03 \pm 25.4 \times 10^{-6}$	0.03	length of assembly
b	m	$0.013 \pm 25.4 \times 10^{-6}$	0.013	width of assembly
h_A	m	52×10^{-6}	52×10^{-6}	thickness of active layer
ρ_A	kg/m^3	1.78×10^3	1.78×10^3	density of active layer
Y_A	N/m^2	$2.0 \times 10^9 - 2.6 \times 10^9$	2.0×10^9	Young's modulus of active layer
d_{31}	C/N	$23 \times 10^{-12} - 27 \times 10^{-12}$	20×10^{-12}	piezoelectric coefficient
h_I	m	125×10^{-6}	137×10^{-6}	thickness of inactive layer
ρ_I	kg/m^3	1.3×10^3	1.3×10^3	density of inactive layer
Y_I	N/m^2	$2.5 \times 10^9 - 2.8 \times 10^9$	2.7×10^9	Young's modulus of inactive layer
c_D	$N/sec/m^2$		2.2848×10^{-7}	coefficient of structural dampening
γ	$N/sec/m^2$		0.005	coefficient of air dampening

Table 2.1: Parameters employed in model

the line produced from the model is 0.1939×10^{-5}. Thus our model fits the experimental data with a relative error of 1.99% (the relative error in intercepts is 6.72%). The model fit to experimental data, obtained in this manner, appeared to be very reasonable.

2.6 Conclusions

2.6.1 Directions for Future Work

Future work can be conducted in efforts to answer the question of whether or not the angle of the tip displacement versus the voltage curve changes with voltage in the experimental data, with different models, or with the use of different measuring instruments.

In addition, futher experiments would be beneficial in verifying the model. The use of different materials such as copper with the active PVDF layer in taking experimental data could further verify the validity of the model.

Further consideration should be given to impulse, blocking, and uniform external forces such as those measured in a wind tunnel.
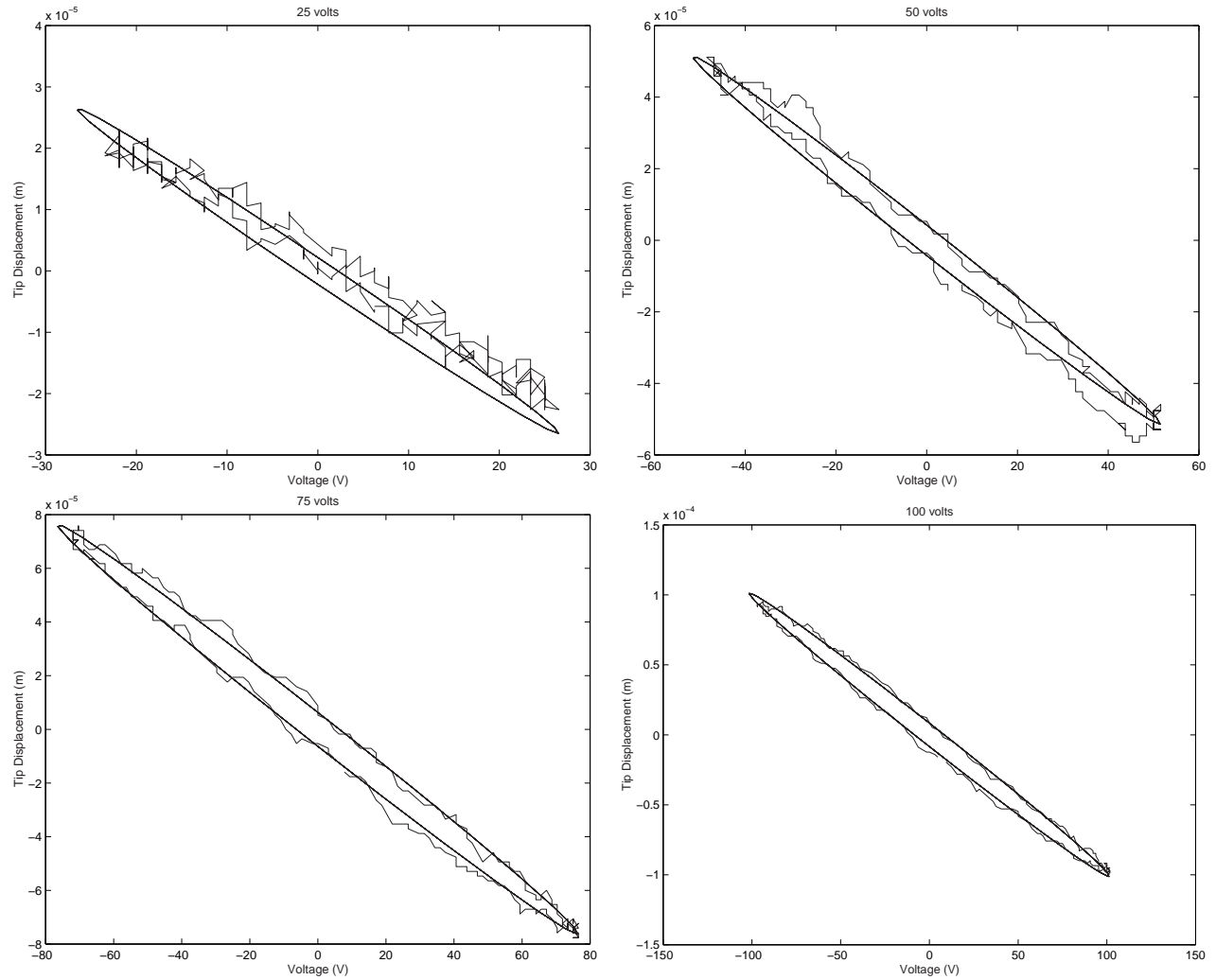

Figure 2.5: Experimental data compared to model predictions.

2.6.2   Characteristics of Unimorph (blocking force)

There are two values that characterize a particular unimorph, free-tip displacement and blocking force. As mentioned previously, free-tip displacement is the proportionality constant (i.e., the slope) representing how the full range of the tip movement relates to the applied voltage. Hence it is natural (and an important check) to compare this constant given by experimental values and those suggested by the model. Comparing slopes from the above fitted functions, our model fits the experimental data with a relative error of 1.99% (the relative error in intercepts is 6.72%), which is quite reasonable for model to experimental result comparison.

A future confirmation of the model would be to verify the other value used to characterize a unimorph, blocking force, between experimental values and predicted values. Blocking force is measured as the amount of force that can be applied at the tip of the unimorph so that the tip of the unimorph does not move with the force. This should be the equivalent force to that which the unimorph exerts on a solid, immovable block. This force should be proportional to the voltage applied to the piezoelectric part of the unimorph.

To determine the blocking force predicted by the model, we need to determine the external force f such that it is 0 everywhere except at the end where we let $f(L) = F_B$. Hence, solve for F_B when the tip displacement is constant at 0, i.e,

$$f(t, L) = -\frac{\partial^2}{\partial x^2}[K_B V(t)\chi_A(L)] - Y\frac{\partial^4 w}{\partial x^4} - C_D\frac{\partial^5 w}{\partial x^4\,\partial t}.$$
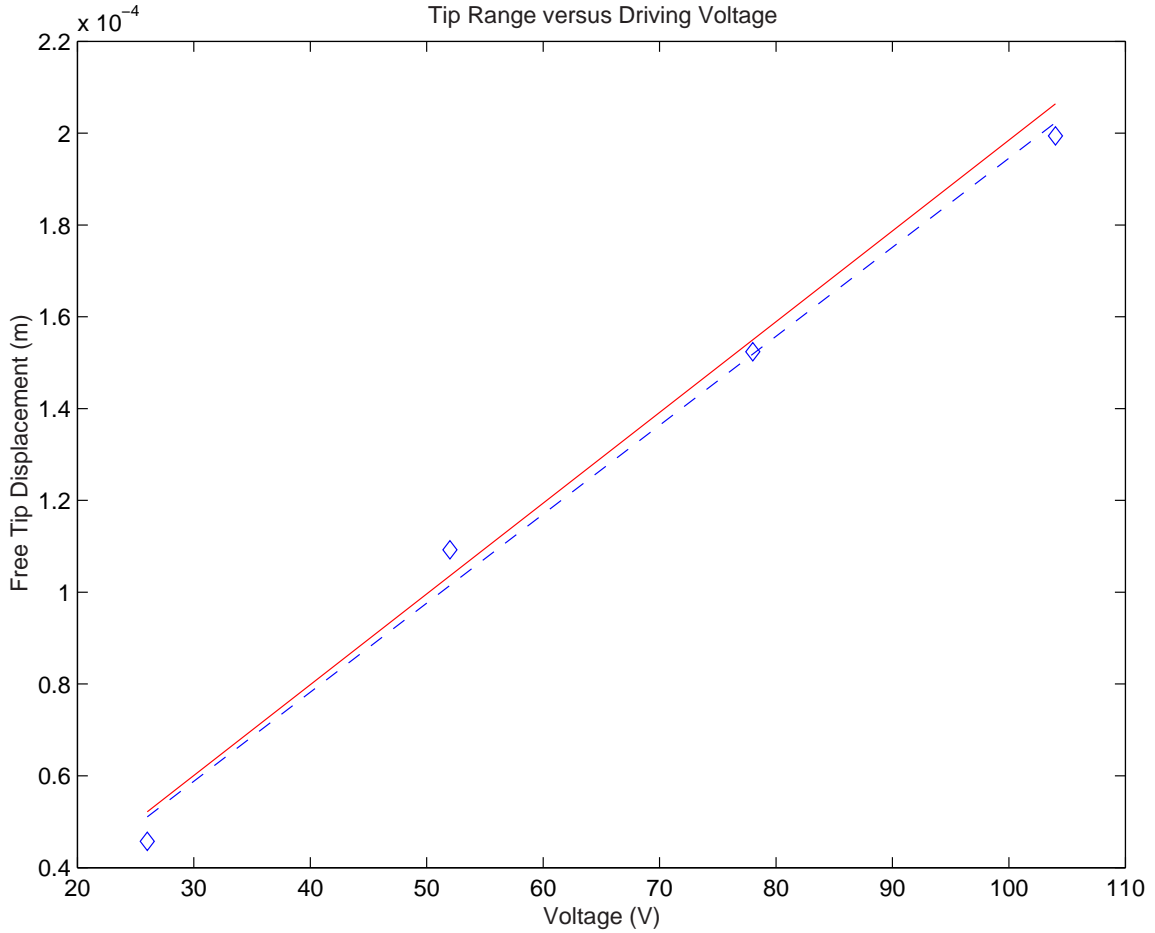

Figure 2.6: Comparison between experimental and numerical data

2.6.3 Inverse Problem

In any model one can always consider whether an inverse problem could be used to determine one or more of its input parameters given a known result. For the model presented here, the most uncertain parameter is d_{31}. Knowing the model's sensitivity to d_{31} and the relative ease of measuring tip displacement precisely and accurately, one very hopeful direction this model might take is to provide another way of calculating d_{31} for piezoelectric polymers.

2.6.4 Directions of Potential Model Improvements

Currently the model does NOT take into account the potential stretching of the inactive and adhesive layers. Additionally, the conductive layers have been ignored.

The primary parameter that would have "picked up the slack" in the model from the previously mentioned neglected conditions is the damping factor c_D. As these other conditions are added, the dependence on c_D is likely to diminish. The structural dampening term whose coefficient is c_D is currently based on Kelvin-Voigt dampening, though in this case a visco-elastic Boltzmann kernel based term would be more accurate but more difficult to compute.

Bibliography

[1] H.T. Banks, R.C. Smith and Y. Wang ,*Smart Material Structures: Modeling, Estimation and Control*, Masson/John Wiley, Paris/Chichester, 1996.

[2] I.H. Shames, *Introduction to Solid Mechanics*, Prentice – Hall, Inc. Englewood Cliffs, New Jersey, 1975.

[3] S.P. Timoshenko and J.M. Gere, *Mechanics of Material*, D. Van Nostrand Company, New York, 1972.

[4] X. Li, W.Y. Shih, et al., "Electromechanical Behavior of PZT-Brass Unimorphs," *Journal of the American Ceramic Society,* 82(7), pp. 1733-1740, 1999.

[5] Z. Ounaies, J.A. Young, and J.S. Harrison "An Overview of the Piezoelectric Phenomenon in Amorphous Polymers," *Field Responsive Polymers: Electroresponsive, Photoresponsive, and Responsive Polymers in Chemistry and Biology;* Editors: I.M. Khan and J.S. Harrison, American Chemical Society, 726(6), pp. 88 - 103, 1999.

2.7   Appendix

2.7.1   Piezoelectric Coefficient d_{vs}

In specifying the piezoelectric coefficient of a material, scientists specify a coordinate system as depicted in Figure 7. A piezoelectric coefficient denoted by d_{vs} will be a measurement of the change along direction s when an electric field is applied in the v direction. As one can see from Figure 7, the arrangement of our unimorph, the electric field is in the 3 direction so our concern is with the 3 piezoelectric coefficients d_{31}, d_{32}, and d_{33}.

d_{33}: This concerns changes in the thickness of the material (Δh) due to voltage applied. In a unimorph, this will affect h_A directly and indirectly anything that depends on h_A.

d_{32}: This concerns changes, in the width of the material (Δb) due to an applied electric field. In a unimorph this will not only change the cross-sectional area (and anything dependent upon it) but also cause curling along the width b which is assumed not to happen.

d_{31}: This concerns change in the length of the active layer in a unimorph (ΔL) due to applied voltage. In a unimorph this directly causes the longitudinal bending which deflects the tip.

Additionally, d_{31} and d_{32} both would stretch all bounding inactive layers in the unimorph. Since our concern is with longitudinal bending, the primary piezoelectric coefficient we are concerned with is d_{31}. In making our assumptions we have simplified our model such that $d_{32} = 0 = d_{33}$.
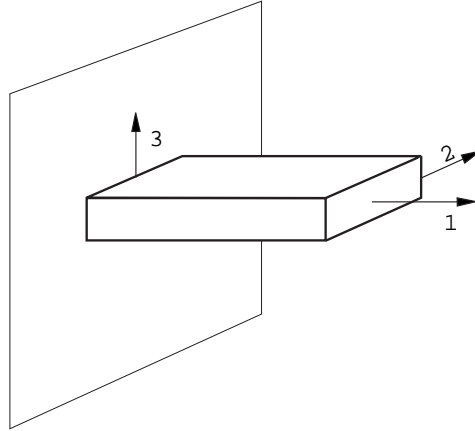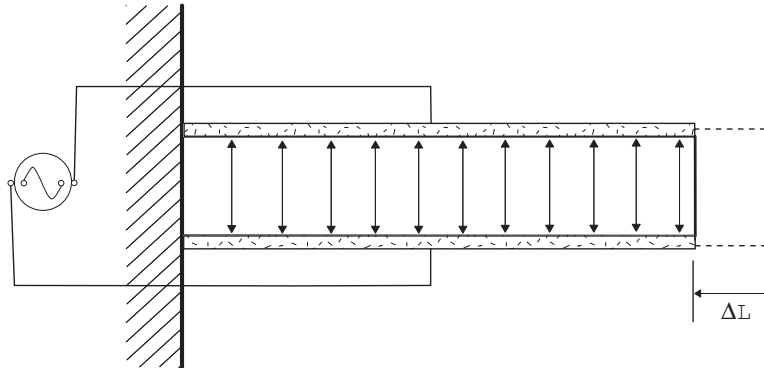

Figure 2.7: Depiction of the coordinate system

Figure 2.8: Picture of electric field in 3 direction and expansion in the 2 direction

Report 3

Pricing Interest Rate Related Instruments

Soad Abuhawas[1], Jeffrey Burnett[2], Oliver Díaz[3], Chuan Hsiang Han[4], Mahendra Panagoda[5], Yi Zhao[6]

Problem Presenter:
Yeol Cheol Seong
Bank of Montreal

Faculty Consultant:
Jean-Pierre Fouque

Abstract

This paper is concerned with implementing a method for pricing interest rate related derivatives. We first show a method for estimating the term structure of interest rates from market data and then show how this term structure is used to calibrate the Black-Derman-Toy model, a binomial model for the evolution of the short rate. An alogrithm for constructing the model is given and prices for several interest rate derivatives are then calculated using the Arrow-Debreu pricing scheme. Lastly, a framework for pricing coumpound options is explored.

3.1 Introduction and Motivation

Our project is concerned with the relationship between market interest rates and the valuation of derivatives on debt instruments. These debt instruments are contracts by which an investor lends money to a borrower in return for the promise of future cashflows. Derivatives on these debt instruments allow an investor to negotiate terms today for a debt instrument contract in the future. Many such derivatives allow the investor the option of entering into the debt agreement. Such derivatives are fittingly called "options." Another class of derivative contracts are "futures," which do not allow the option to exercise, but the terms of the negotiated price may be traded on the open market. Our task is to take public information about the price of traded assets to build

---

[1]Texas Technical University
[2]North Carolina State Univeristy
[3]University of Texas at Austin
[4]North Carolina State University
[5]Michigan State University
[6]Rutgers University

a framework for understanding the present value of future cashflows and to then determine a fair price for a variety of derivative contracts based on future cashflows.

Constructing an accurate model of expected future interest rates is of tantamount importance to members of the financial community. An accurate model allows both borrowers and lenders of money to protect themselves against unfavorable shifts in the interest rate. Such a model also allows firms the ability to negotiate the terms today for a loan that will begin at some time in the future. Such a model is often called the "term structure of interest rates." The term structure is not one number or one function, but a group of relationships that describe different aspects of future interest rates. There are four main aspects of the term strucutre: the discount curve, a spot interest rate curve, the implied forward rate curve, and the par yield curve. We must also distinguish between a model of today's yield curve and a dynamic model of the term structure that will allow us to price instruments other than bonds. We show a technique for estimating today's yield curve from market data called "bootstrapping" the yield curve. We will also explore one of the many models of the dynamic term structure of interest rates. This model will take the information gleaned from the "bootstrapping" technique as input.

The bootstrapping method estimates a discount curve for present value calculations. Because of a one-to-one relationship between the curves, once one is found the others may be computed. The different curves draw out different aspects of the purchasing power of future cashflows, and which is used depends on the task at hand. In particular, if an option on a financial asset is expected to pay some amout in six months, we must use the discount curve to discount the payoff if we want to know the value in today's prices. This is due to the time value of money, by which the promise of a dollar tomorrow is worth less than a dollar in today's prices. But how can we model interest rates? Interest rates are not traded like stocks, so we cannot observe the price and use it directly in our model. We can, however, observe the price of bonds, and the market determined prices may be our best bet for building a model.

To construct a dynamic model of the term structure we must decide how many dimensions to incorporate into our model. The most accurate model would have a dimension for bonds maturing at every time from now into the infinite future. As such, this would be an infinite dimensional stochastic differential equation and it would be intractable. Instead we could choose to model the short rate of interest, the rate for very short periods of time. We could, in fact, construct a model in which two or more factors would influence the short rate, but the simplest model incorporates only one source of randomness.

Equipped with an understanding of the term structure of interest rates and a model of the short rate, we can begin to price a variety of derivative securities whose payoff is a function of the evolution of the interest rate. There are two basic classes of options: a call option gives the buyer of the option the right to buy something in the future at a price determined today, and a put option gives the buyer of the option the right to sell something at a predetermined price at some future date. Naturally, there are buyers and sellers of options, so depending on the circumstances you might buy a call or sell a put. Combinations of these basic building blocks into so-called structured products allow flexible payoffs to be built that can act as very specialized insurance policies against the unknown. Options based on the interest rate may pay, for example, if the interest rate rises above some predetermined level. This type of option would protect borrowers from high interest rates. Other options allow the buyer to swap a floating interest rate for one that is fixed, if it benefits the buyer. We will use our dynamic model of the term structure to price a family of such interest rate derivatives. We will show techniques for pricing swaps, swaptions, caps and floors, and show prices determined from market data. We will also explore ways to price a compound option, a structured product that gives the option to buy or sell a group of options.

The sticking point with options is determining the fair price for such a right. If the price is too high or too low then someone may make money with probability one; that is, an arbitrage has been created. One way to determine the value of an option today is to calculate the expected payoff of the option and then discount this payoff. Discounting the expected payoff is necessary because of the time value of money. We must be careful, though, to use the correct probabilities when we calculate the payoff. We must use the probabilities as if the game were fair, the so-called risk-neutral probabilities. Luckily, with interest rates we deal solely in the risk-neutral world so we will not have to change our measure.
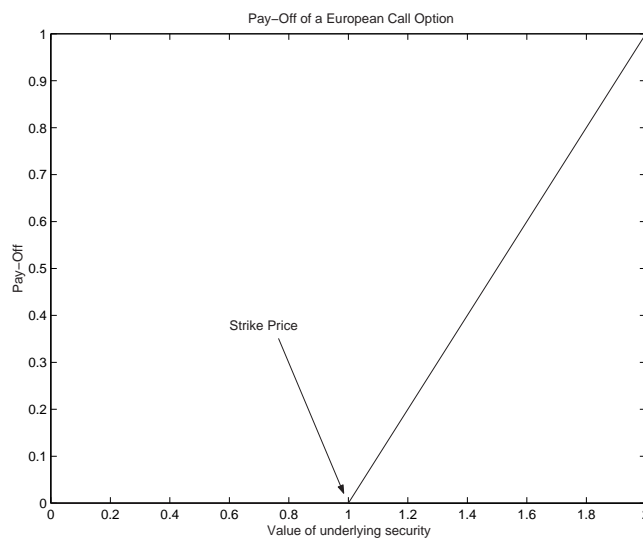
Figure 3.1: Payoff for European Call Option

The call pays $\max(S_T - K, 0)$ to the buyer of the option, where S_T is the asset price at time T and K is the strike price. The purchaser of the call buys the right to buy an asset below the going market price.
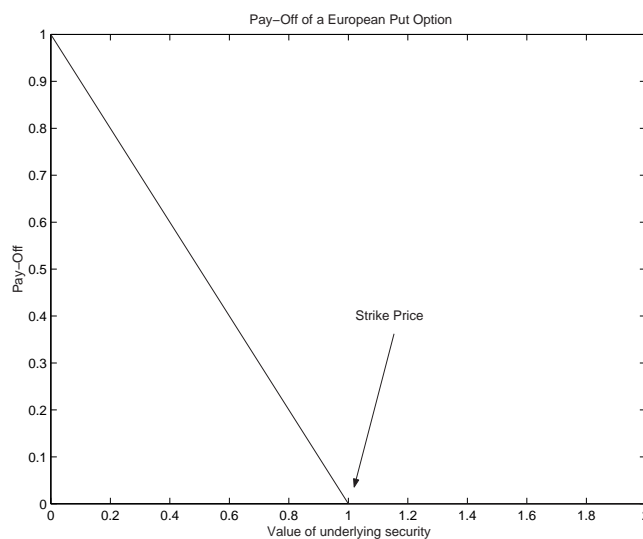

Figure 3.2: Payoff for European Put Option

The put pays $\max(K - S_T, 0)$ to the buyer of the option, where S_T is the asset price at time T and K is the strike price. Thus, the purchaser of the option buys the right to sell above the market price.

3.2 The Yield Curve

3.2.1 Estimating the yield curve

We will first describe the "bootstrapping" technique. In risk management, it is important that we value future cash flows of an asset in a consistent and dependable way. The yield on a bond is often described as its internal rate of return and a yield curve is a plot of the yield versus the time to maturity starting today. Since there is no consistent set of yields that we can observe, we must construct a yield curve by stiching together information from several different sources. In a broader sense, the yield curve is important in pricing stocks and futures, managing risk and trading structured derivatives as it encodes information about liquidity, inflation rates and the market risk. In essence, the yield curve reflects the state of the economy. Our goal will be to make one curve for the discount factor for different times to maturity. That is, we will recharacterize everything as a zero-coupon bond. If the cash flow t years from today is C(t) and the discount factor is Z(t), then the present value of the cash flow is:

$$\text{Present Value} = C(t)Z(t).$$

The timing for cash flows are specified in the contracts. Zero-coupon bonds pay nothing until maturity, when all interest and principle is repaid. Coupons bonds usually pay interest twice a year and repay principle and a final interest payment upon maturity. The "yield curve" gives information on $Z(t)$, the discount factor, enabling us to price the asset at present accordingly.

Our goal is to build a yield curve for Eurodollars with the data available from the markets, but which data is best? Economic theory tells us that the prices on actively traded assets will reach an equilibrium so that the price reflects the true demand, so we will use data on actively traded assets. Such assets are described as being liquid, since there is a ready market for them. Since by definition the yield curve describes the term structure of interest rates in the market, we will use money market, futures and swap prices to come up with a single yield curve. Since money market data gives the best information on discount factors for relatively small time scales, we use money market data coupled with the following formula to obtain the first discount factors:

$$Z(t) = \frac{1}{1 + d(t)\alpha(t_0, T)},$$

where $d(t)$ is the cash deposit rate which is given and α is the accrual factor between day t_0 and T. The spot date or the settlement date is t_0.

In calculating the accrual factor we make use of a program often called a calendar generator. This program calculates the number of business days between two given dates. In addition to weekends, the calendar generator takes into account the New York Stock Exchange (NYSE) holidays and United States federal holidays. Different markets use different conventions in evaluating the accrual factor: for example, the Euro data is calculated on the basis known as 30/360. This convention assumes that every year has 360 days and every month is made of 30 days and follows the algorithm

$$\text{number of days between } T_1 \text{ and } T_2 = (D_2 - D_1) + 30(M_2 - M_1) + 360(Y_2 - Y_1),$$

D is day portion of the date, M is month part, and Y is the year portion. So, the number of days between March 5, 2001 and July 15, 2005 is

$$
\begin{aligned}
\text{number of days} &= (15 - 5) + 30(7 - 3) + 360(2005 - 2001) \\
&= 10 + 120 + 1440 \\
&= 1570
\end{aligned}
$$

Other conventions, such as ACT/ACT, ACT/365 and ACT/360 count actual days in each month and the actual number of days in the year (either 365 or 366), and combinations of these. The calendar generator code

employes a lookup table containing every holiday for each of the two most common markets in the United States(NYSE and Federal) until 2030. The holidays were calculated algorithmically, so the generator could determine holidays for longer time horizons. Tables are used to economize on computations.

Futures data provide the most reliable information on market conditions for intermediate times to maturity. Therefore, we use the available data on Euro futures to calculate discount factors for times typically from a few months to a few years. With respect to Euro futures, the settlement date is second business day before the third Wednesday of March, June, September and December. And, as before, we calculate the discount factor at time T as

$$Z(T_2) = Z(T_1)\frac{1}{1 + (T_1, T_2)\alpha(T_1, T_2)},$$

where $Z(T_i)$ is the discount factor for futures at time T_i. From the given data on $P(T_1, T_2)$ we calculate $f(T_1, T_2)$, the forward rate, using the expression

$$f(T_1, T_2) = \frac{100 - P(T_1, T_2)}{100}.$$

For any i, we have the recurrence formula

$$Z(T_i) = Z(T_{i-1})\frac{1}{1 + f(T_{i-1}, T_i)\alpha(T_{i-1}, T_i)}.$$

An important assumption we make here is that there are no gaps, i.e. settle dates match. Techniques exist to accomodate non-overlapping data, but we will not discuss these here. Also, when we do not have data on a particular discount factor, we interpolate between two known dates. The method of interpolation has a significant effect on the foward rate curve that will be computed from the discount curve. Choice of interplation method is an active area of research and optimal techniques have not yet been established. We used spline interpolation but feel that other methods need to be tested.

As we move 2-3 years into future, the data on swap rates become most reliable. Following our pattern on calculating discount factor and since the par swap rate by definition has zero net present value, we get, after simplifying

$$Z(T_N) = \frac{1 - S(T_N)\sum_{i=1}^{N-1}\alpha(t_{i-1}, t_i)Z(T_i)}{1 + \alpha(T_{N-1}, T_N)S(T_N)},$$

where $S(T_i)$ is the par swap rate in year i. Transforming swap data into a simple discount factor requires that we take into account coupon payments made on swap agreements. For instance, if we use money market and futures data for times to maturity up to two years, and our swap data is on swaps that pay semi-annual payments, we must consider the four payments made on a swap with two years time to maturity.

Finally, putting together data on discount factors for money market rates, futures and swap rates, we obtain a complete discount curve. There is a one-to-one correspondence between the discount curve and the forward rate curve, so we can apply to following formula to obtain the forward rate curve. From period 1 to 2 the forward rate is:

$$F(T_1, T_2) = \left(\frac{Z(T_1)}{Z(T_2)} - 1\right)\frac{1}{\alpha(T_1, T_2)}.$$

3.2.2 Sample data and output from yield curve generator

Sample market data is shown in the following tables. The LIBOR data (London Inter Bank Offered Rate), shown in Table 3.1 is the rate the most creditworthy international banks charge each other for large loans based on Eurodollars. Such loans typically have short maturities. Eurodollars are simply U.S. currency held in banks outside the United States.

Libor	Ask
2 day	5.475
1 month	5.475

Table 3.1: LIBOR data

Contract	Ask
Mar97	94.3900
Jun97	94.2100
Sep97	94.0200
Dec97	93.8100
Mar98	93.7100
Jun98	93.6100
Sep98	93.5300
Dec98	93.4200
Mar99	93.3900
Jun99	93.3300
Sep99	93.2700
Dec99	93.1800

Table 3.2: Futures data*Futures contracts are settled two business days after purchase.*

The data is Table 3.2 is for Euro Futures. The price quoted is for a zero whose par price is 100. Contracts expire two business days before the third Wednesday for the months quoted.

Table 3.3 lists the par swap rate for several swaps with semi-annual coupon payments. Depending on the market, swaps with different tenors may have different coupon payment frequencies. For example, swaps with short tenors may pay quarterly while longer tenors may pay semi-annually. Also note that the day count basis is consistent for these swaps, but it may not be for another market.

The "bootstrapping" method described earlier takes the market data and produces one discount curve. The discount factors for January 29, 1997 is reproduced in Table 3.4 and plotted in Figure 3.3. Implied forward rates calculated from the discount factors are shown in Figure 3.4.

Tenor	Ask
1 SA ACT/365	5.9345
2 SA ACT/365	6.2300
3 SA ACT/365	6.4251
4 SA ACT/365	6.5353
5 SA ACT/365	6.6371
7 SA ACT/365	6.7918
10 SA ACT/365	6.960391
12 SA ACT/365	7.041999
15 SA ACT/365	7.138803

Table 3.3: Swap data *All swaps shown pay semi-annual coupons and use the accounting standard that counts the actual number of days in a month with a 365 day year.*

	Maturity	Discount
LIBOR	29-Jan-97	1.0000
	31-Jan-97	0.9997
	2-Feb-97	0.9994
	28-Feb-97	0.9955
Futures	17-Mar-97	0.9929
	16-Jun-97	0.9790
	15-Sep-97	0.9649
	15-Dec-97	0.9505
	16-Mar-98	0.9359
	15-Jun-98	0.9212
	14-Sep-98	0.9066
	14-Dec-98	0.8920
	15-Mar-99	0.8774
	14-Jun-99	0.8630
	13-Sep-99	0.8487
	13-Dec-99	0.8345
Swaps	13-Mar-00	0.8203
	31-Jul-00	0.7993
	29-Jan-01	0.7723
	30-Jul-01	0.7461
	29-Jan-02	0.7201
	29-Jul-02	0.6953
	29-Jan-03	0.6710
	29-Jul-03	0.6473
	29-Jan-04	0.6240
	29-Jul-04	0.6022
	31-Jan-05	0.5806
	29-Jul-05	0.5595
	30-Jan-06	0.5392
	31-Jul-06	0.5193
	29-Jan-07	0.4998
	30-Jul-07	0.4815
	29-Jan-08	0.4637
	29-Jul-08	0.4466
	29-Jan-09	0.4298
	29-Jul-09	0.4138
	29-Jan-10	0.3984
	29-Jul-10	0.3834
	31-Jan-11	0.3689
	29-Jul-11	0.3547
	30-Jan-12	0.3412

Table 3.4: Discount Factors *The discount curve computed from money market, futures, and swap data. All three data sets are stiched together to form one curve, which is then used to compute the other aspects of the term structure.*
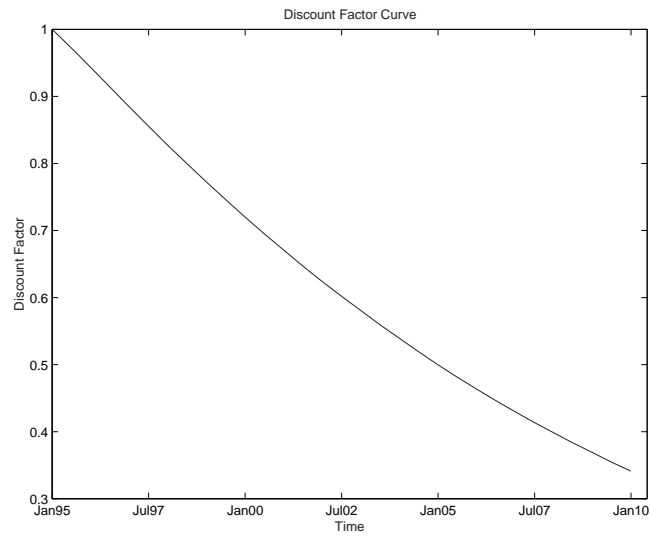
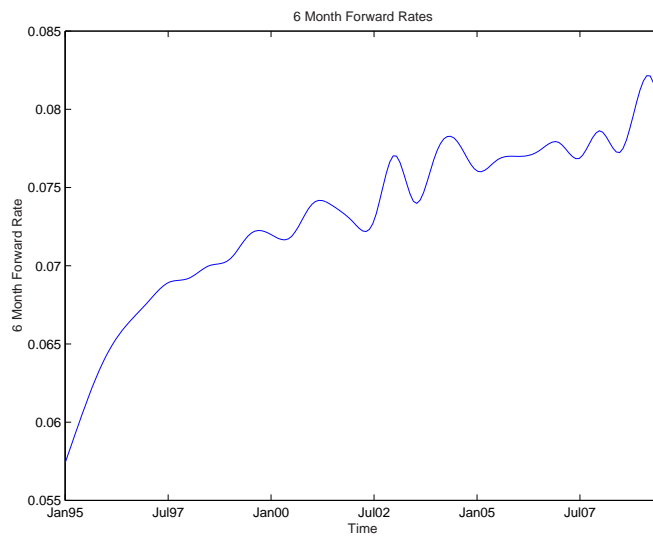Figure 3.3: Dicount Factor Curve *The discount factor for zero time to maturity is by definition 1.*

Figure 3.4: Six month forward rates
Forward information calculated from discount factors in Table 3.4

3.3 Interest Rate Models

3.3.1 Basic Binomial Model

The binomial model assumes that the underlying asset price follows a binomial process. Assume that p is a constant between 0 and 1. Some security is worth S_0 today, and a year later it may go up to S_u with probability p or down to S_d with probability $1 - p$. If the current one year rate is r, then the value of S at time 1 is

$$S_1 = \frac{pS_u + (1-p)S_d}{1+r} \tag{3.3.1}$$

where $pS_u + (1-p)S_d$ is the expected value and $\frac{1}{1+r}$ is the discount factor. Equation (3.3.1) holds for each node of the price tree, while the short rate r varies from node to node.

3.3.2 Modeling the Interest Rate

A General Framework

Since the 1980s the volume of trading in interest rate related instruments has increased dramatically. Evaluating the interest rate products is more difficult than evaluating equity and foreign exchange derivatives, since interest rate models are concerned with movements of the entire yield cure - not just with changes of a single variable. Also, as mentioned previously, we cannot directly observe interest rates in the same way that we can observe, say, a stock price.

One class of models of the interest rate is based on a process for the short-term risk-free rate, r. The short rate, r, at time t is the rate that applies to infinitesimally short period of time at time t. (Although in practice, the short period can be considered as a day, or even longer.)

Suppose an interest rate derivative provide a payoff $X = \Phi(S_T)$ at time T. If we let $\bar{r}$ be the average value of r in the time interval between t and T, the value of X at time t is given by

$$P(t, X) = E^\star \left[\frac{\Phi(S_T)}{1 + \bar{r}(T - t)} \right]$$

where $E^\star$ denotes expected value in a risk-neutral world. Accordingly, $P(t, T)$, the price at time t of discount bond that pay off \$1 at time T, satisfies:

$$P(t, T) = E^\star \left[\frac{1}{1 + \bar{r}(T - t)} \right]$$

If $R(t, T)$ is the interest rate at time t for a time to maturity of $T - t$,

$$P(t, T) = E^\star \left[\frac{1}{1 + R(t, T)(T - t)} \right]$$

Therefore,

$$R(t, T) = \frac{1}{T - t} \left(\frac{1}{E^\star \left[\frac{1}{1 + \bar{r}(T - t)} \right]} - 1 \right)$$

Once we define the process r, we have a model for the evolution of the term structure and a means to price bonds, bond options, and other interest rate products.

One approach, for instance Vasicek (1977), Cox, Ingersoll and Ross (1985), has been to propose a model for the short-term interest rate and deduce a model for the term structure based on an Ornstein-Uhlenbeck process. The Vasicek model is one of the simplest and it admits a solution with a Gaussian distribution. The Cox, Ingersoll, and Ross model, know as the CIR model, makes a slight modification to the volatility term and has a solution with a non-central chi-square distribution. Full information maximum likelihood estimation may

$Model$	$\mu(r,t)$	$\sigma(r,t)$
Vasicek	$a(b-r)$	σ
Cox, Ingersoll and Ross	$a(b-r)$	$\sigma\sqrt{r}$
Ho and Lee	$\Theta(t)$	σ
Hull and White-Extended Vasicek	$\Theta(t)-a(t)r$	$\sigma(t)$
Hull and White-Extended CIR	$\Theta(t)-a(t)r$	$\sigma(t)\sqrt{r}$

Table 3.5: *Martingale models for the Short Rate*

be used for parameter estimation since distribution of the solutions are known. For a thorough examination of a variety of models, see Rebonato [8].

Ho and Lee(1986)[5], Black, Derman, and Toy(1990)[2], Hull and White(1990)[6] consider how to describe yield curve movement using a "one-factor" model. They take market data, such as the current term structure of interest rates. By specifying the initial yield curve and its volatility structure, they are able to determine a drift structure that makes the model arbitrage free. Heath, Jarrow, and Merton(1992) [4] simulate the evolution of forward rates by allowing the volatility functions, $\sigma_i(\cdot)$, to depend on the entire forward rate curve. The main advantage of the model is th ability to easily specify the initial forward rate (or yield) curve abd their volatilities and correlations.

One Factor Models of The Short Rate

Among the models describing the process of r, those involves one source of uncertainty are called *one-factor* models. In many one-factor models, the short rate r is usually given by a stochastic process:

$$dr = \mu(r,t)dt + \sigma(r,t)dW$$

where W is a Wiener process. Some examples with their specification of μ and σ are given in Table 3.5. For a good discussion of the various models, see Hull[7].

In contrast, the Black, Derman and Toy model (BDT in the following) [2] is a one-factor model that assumes a log-normal process for r:

$$d\log(r) = \left[\Theta(t) + \frac{\sigma'(t)}{\sigma(t)}lnr\right]dt + \sigma(t)dW \qquad (3.3.2)$$

BDT developed a single-factor short-rate model to match the observed term structure of spot interest rate volatilities, as well as the term structure of interest rates, and which has proved popular with practitioners. The BDT model can be used to price any interest-rate-sensitive security (bond options, swaps, etc.) without requiring the explicit specification of investors' risk preferences. The input of model is an array of yield on zero-coupon bonds with various maturities, and an array of yield volatilities of these bonds. In the next section, we will analyze the BDT model algorithmically.

3.3.3   The Black, Derman and Toy Model

As with the original Ho and Lee model, the BDT model is developed algorithmically, describing the evolution of the entire term structure in a discrete-time binomial lattice framwork. A binomial tree is constructed for the short rate in such a way that automatically returns the observed yield function and the volatilities of different yields.

Mathematical Description of the Model

The log-normal process of r prevents the negative rates and make model calibration to some interest rate product much easier. From Equation (3.3.2), one can see that the assumption of decaying short rate volatility

is required to prevent the unconditional variance of the short rate, $\sigma(t)^2 t$, from increasing with t without bound, which could be inconsistent with the mean-reverting character of the short rate process.

The solution to equation (3.3.2) is of the form

$$r(t) = u(t)e^{\sigma}(t)W(t),$$

where $u(t)$ satisfies

$$\frac{d\ln u(t)}{dt} = \Theta(t) + \frac{\sigma'(t)}{\sigma(t)}\ln u(t)$$

is the mean of the short rate distribution at time t and $\sigma(t)$ the short rate volatility. In this model, changes in the short rate are lognomally distributed, with the resulting advantage that interest rates can not become negative. The BDT model incorporates two independent functions of time, $\Theta(t)$ and $\sigma(t)$, chosen so that the model fits the term structure of spot interest rates and the term structure of spot rate volatilities. Once $\Theta(t)$ and $\sigma(t)$ are chosen, the future short rate volatility, by definition, is entirely determined.

Benefits and Problems with the Model

Since there is much evidence that volatility is not constant, the clear benefit of the BDT model is its use of a time-varying volatility. One of the model's strengths is also one of its weaknesses. Since the model is easily calibrated to market data, practitioners favor the model. However, the model must be recalibrated often and will often give inconsistent results. That is, the model is not robust. Secondly, due to its lognormality neither analytic solutions for the price of bonds nor the price of bond options are available and numerical procedures are required to derive the short rate tree that correctly matches market data.

3.3.4 Implementing the BDT Model

We will use a recombining binomial tree to represent the stochastic process of the short rate. If one time step on the tree is Δt, the short rates on the tree are simple Δt-period rates. The usual assumption when a tree is built is that Δt-period rates follow the same stochastic process as the instantaneous rate in the corresponding continuous model.

The Short Rate Tree and Arrow-Debreu Price

The idea of BDT model is to use a multiplicative binomial tree to model the risk-neutral dynamics of the interest rate by calibrating to term structure and volatility data. The general short rate tree looks like the tree shown in Figure 3.5.

If we let $r(i, j)$ be the short interest rate at nodal (i, j), where j means the number of periods and $j - i$ means the number of upward moves. Also define,

(i, j): node at time j and state i.

r_u, r_d: value of r at nodes $(0, 1)$ and $(1, 1)$, respectively.

S_u, S_d: value of S at nodes $(0, 1)$ and $(1, 1)$, respectively.

$Y_u(i)$, $Y_d(i)$: yields at nodes $(0, 1)$ and $(1, 1)$, respectively, on a discount bond maturing at time $i\Delta t$.

Define an Arrow-Debreu security as a contract that pays \$1 at (i, j), and zero at any other nodes. Denote its price at time $t \leq j$ and state k by $G(k, t, i, j)$. For example, $G(0, 0, 2, 2)$ would be the price at node $(0, 0)$ of a security that pays \$1 at time 2 and in state 2. If we know the value for the short tree up to time j, i.e. $\{r(:, k)\}_{k=0}^{j}$, we could obtain the value of $G(k, t, i, j), 1 \leq k \leq t, 1 \leq t \leq j$ simply by repeating the basic pricing formula (3.3.1). Note that BDT assumes $p = \frac{1}{2}$. For instance,
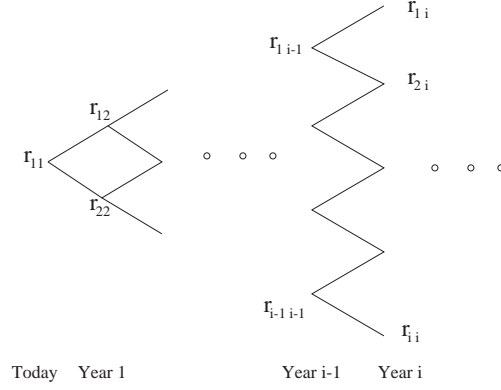
Figure 3.5: *Short Rate Tree*

$$
\begin{aligned}
G(0,0,2,2) &= \frac{1}{1+r_{0,0}} + \{\frac{1}{2} \times \frac{1}{1+r_{0,1}} \times [\frac{1}{2} \times 1 + \frac{1}{2} \times 0] + \frac{1}{2} \times \frac{1}{1+r_{1,1}} \times [\frac{1}{2} \times 0 + \frac{1}{2} \times 0]\} \\
&= \frac{1}{4} \frac{1}{1+r_{0,0}} \frac{1}{1+r_{1,1}}
\end{aligned}
$$

In general, for any intermediate node

$$
G(0,0,i,j) = \frac{1}{2} \frac{G(0,0,i-1,j-1)}{1+r_{i-1,j-1}} + \frac{1}{2} \frac{G(0,0,i+1,j-1)}{1+r_{i+1,j-1}} \tag{3.3.3}
$$

and for any extremal node (this means $i = j$ or 0)

$$
G(0,0,0,j) = \frac{1}{2} \frac{G(0,0,0,j-1)}{1+r_{0,j-1}} \tag{3.3.4}
$$

$$
G(0,0,j,j) = \frac{1}{2} \frac{G(0,0,j-1,j-1)}{1+r_{j-1,j-1}}
$$

Equations (3.3.3) and (3.3.4) are called the Fokker-Plank equations. Actually, the Arrow-Debreu price G plays a role like Green's function does in PDEs. Once we have the Arrow-Debreu price $G(0,0,i,j)$ for all i and j, we can price any security just by multiplying its payoffs at any node by the Arrow-Debreu price corresponding to that node, which is analogous to a convolution in PDEs.

The key to computing the Arrow-Debreu price is to know the short rate tree in advance. How do we calibrate the short rate tree from given the current zero-coupon yield $\{Y(i)\}_{i=1}^n$ and yield volatility $\{\sigma(i)\}_{i=1}^n$? We use the following algorithm.

1. At time 0, we have of course $r_{0,0}$ given and equal to $Y(1)$.

2. Suppose we knew the values of $\{r(:,k)\}_{k=1}^{j-1}$. Note also that we have all the $G(0,0,l,n)$, $1 \le l \le n$ and $1 \le n \le j-1$, through the Fokker-Plank equations.

3. At time j, we have to find n unknowns $\{r(i,j)\}_{i=1}^j$. Because BDT model assumes that the short rate is lognomal with a volatility that depends only on time, which implies

$$
\frac{r(1,j)}{r(2,j)} = \frac{r(2,j)}{r(3,j)} = \cdots = \frac{r(j-1,j)}{r(j,j)}.
$$

So we need two equations to solve for $r(1,j)$ and $r(2,j)$, say.

Maturity (Years)	Yield (%)	Yield Volatility (%)
1	10	20
2	11	19
3	12	18
4	12.5	17
5	13	16

Table 3.6: Sample Term Structure

$Today$	$Year1$	$Year2$	$Year3$	$Year4$
0.1	0.1432	0.1942	0.2179	0.2552
	0.0979	0.1377	0.1600	0.1948
		0.0976	0.1183	0.1406
			0.0872	0.1134
				0.0865

Table 3.7: Short Rate Tree

4. Let's initially guess $r(1, j)$ and $r(2, j)$, then we can compute the short rate tree and the corresponding Arrow-Debreu price.

5. Error Correction: It's clear that

$$S(0,0) = \frac{1}{1 + r_{0,0}}[\frac{1}{2} \times S_u + \frac{1}{2} \times S_d]. \tag{3.3.5}$$

Also, the volatility of a j-year yield is known to be

$$\sigma(j) = \frac{1}{2}\ln(\frac{Y_u(j)}{Y_d(j)}), \tag{3.3.6}$$

where $Y_u(j) = (\frac{1}{S_u})^{j-1} - 1$ and $Y_d(j) = (\frac{1}{S_d})^{j-1} - 1$.

6. Use Newton-Raphson scheme to solve equations (3.3.5) and (3.3.6) to obtain $r(1, j)$ and $r(2, j)$.

3.3.5 Applications

Given a sample term structure, like the one in Table 3.6, one can get the short rate tree in Table 3.7.

And if we compute Arrow-Debreu price $G(0, 0, 1, 2) = 0.0458$ we get the results in Table 3.8.

Options on Treasuries

Let us value a T-year call option on a N-year($T \leq N$) treasury discounted bond with strike price K. (Put options are calculated similarly.) If the price of N-year bond at time T is S_T, the payoff is $\max(S_T - K, 0)$. Using appropriate combination of the Arrow-Debreu prices for each node of the N-year bond, we obtain possible payoffs $S_T(0), S_T(1), \ldots, S_T(T+1)$. Then apply Arrow-Debreu process again to value the current price

Table 3.8: Arrow-Debreu Price Tree *The first value is the discounted payoff of 1*

0.4058	0.4374	0
	0.4554	1
		0

for call option.

Example: Let $T = 1$, $N = 3$, $K = 0.8$, and face value $S=1$. The payoffs are

$$S_1(0) = max\{fv * \sum_{j=0}^{2} G(0,1,j,3), 0\} = 0,$$

$$S_1(1) = max\{fv * \sum_{j=1}^{3} G(1,1,j,3), 0\} = 0.0152.$$

Then we repeat the appropriate Arrow-Debreu process again to get the price

$$p = S_1(0) * G(0,0,0,1) + S_1(1) * G(0,0,1,1) = 0.0069.$$

Caps

A popular interest rate option offered by financial institutions is an interest rate cap. Interest rate caps are designed to provide insurance against the rate on a floating-rate loan rising above a certain level (called *cap rate X*). If the principal is L, and interest payments are made at time $t, 2t, \ldots, nt$ from the beginning of the life of the cap, the buyer of the cap will receive a payment at time $(i + 1)t$ given by

$$Cap_{(i+1)t} = tL \max(R_i - X, 0)$$

where R_i is the floating rate at time it. Therefore, a cap can be viewed as a portfolio of call options on the floating rate R with different maturities $t, 2t, \ldots, nt$. The individual options comprising a cap are referred to as *caplets*.

    We will apply the short rate tree to evaluate the price of cap. Since each caplet is merely a call option, we can apply the method described in the previous section. The today price of cap is the sum of the prices of caplets(call options). Thus, we skip our numerical illustration here.

European Swaptions

Recall that an interest rate swap can be regarded as an agreement to exchange a fixed rate bond for a LIBOR-based floating rate bond. The floating rate is typically of the same maturity as the rate reset frequency. A swaption giving the holder the right to pay fixed and receive floating ("payer" swaption) is equivalent to a put on a fixed rate bond with strike price equal to the pricipal of the swap, and with the coupon payments equal to the quoted swap rate if the reset dates are annual. If the swaption gives the holder the right to pay floating and receive a fixed rate ("receiver" swaption), it is equivalent to a call on a fixed rate coupon bond. Assume that the pricipal is 1. Let $B_{i,j}$ represent the value of the fixed rate bond at node (i, j) in the tree, and C the cash flow at each coupon date.

    The first stage to pricing the derivative is to construct the short-rate tree out until the end of the life of the instrument underlying the option. In our example, $T = 1$ with three years left to maturity, i.e. $N = 4$. For convenience, consider the C treasure as a portfolio of three zero coupon bonds - a one-year zero with C face value; a two-year zero with a C face value; and a three-year zero with a $1 + C$ face value.

    We initialize the value of the fixed rate bond underlying the swap at each of the states at time N, $S_{i,N} = 1 + C$. We then apply backward induction for the coupon bond price, taking discounted expectation until T

$$S_{i,T} = \sum_{j=1}^{N-T-1} \sum_{k=0}^{T+j-1} C \times G(i, T, k, T + j) + \sum_{k=0}^{N-1} (1 + C) \times G(i, T, k, N).$$

    Using the state price at all nodes at time step T the swaption price can be evaluated for payer swaptions and receiver swaptions, we have respectively

$$\text{payer swaption} = \sum_{i=0}^{T} G(0,0,i,T)\max\{1 - S_{i,T}, 0\}$$

$$\text{receiver swaption} = \sum_{i=0}^{T} G(0,0,i,T)\max\{S_{i,T} - 1, 0\}$$

In our example, let $C = 0.1$, for payer swaption, $S_{0,1} = 0.08728$ and $S_{1,1} = 0.9731$ such that for the payer swaption

$$p = \max\{1 - S_1(0), 0\} * G(0,0,0,1) + \max\{1 - S_1(1)\} * G(0,0,1,1) = 0.07.$$

3.4 Options on options

3.4.1 Compound options

Since companies often have different kinds of options on the same stock on one hand hand, and they assume that the market is bullish on the other hand, it is useful to come up to strategies to reduce the risk in their investments. One way to handle that situation is by means of compound options, which are options on options.

The compound option gives the holder the right to buy (call) or sell (put) another option. The compound option expires at some date T_1 and the option on which it is contingent, expires at a later time T_2. In some sence, such an option is weakly path dependent. Let us consider the simple Black and Scholes model with a zero coupon bond B and a risky asset S:

$$
\begin{aligned}
d\,B_t &= r\,B_t\,dt \quad \text{with} \quad B(0) = B_0 \\
d\,S_t &= S_t(\mu dt + \sigma dW_t) \quad \text{with} \quad S(0) = S_0
\end{aligned}
$$

where W_t is standard Brownian motion on some probability space $(\Omega, \mathcal{F}_{t \geq 0}, \mathbb{P})$. Then, the pricing of compound options is straightforward and is basically done in two steps: first we price the underlying option and then price the compound option. Suppose that the underlying option has a payoff of $F(S)$ at time T and that the compound option can be exercised at a earlier time $T' < T$ to get a payoff $H(V(S,T'))$, where $V(S,t)$ is the value of the underlying option at time $t \leq T$. Thus the first step means solving the Feynman–Kac equation

$$
\frac{\partial V}{\partial t} + \frac{1}{2}\sigma^2 x^2 \frac{\partial^2 V}{\partial x^2} + rx\frac{\partial V}{\partial x} - rV = 0
$$
$$
V(x, T) = F(x)
$$

to find $V(x = S, T')$, which is the value of the underlying option at time T', where we can exercise the compound option. For the complition of the second step, let us denote by $G(S,t)$ the value of the compound option, which will satisfy the equation

$$
\frac{\partial G}{\partial t} + \frac{1}{2}\sigma^2 x^2 \frac{\partial^2 G}{\partial x^2} + rx\frac{\partial G}{\partial x} - rG = 0
$$
$$
G(x, T') = H(V(x, T'))
$$

Using probabilistic methods we can derive *precise* expresions for both V and P as
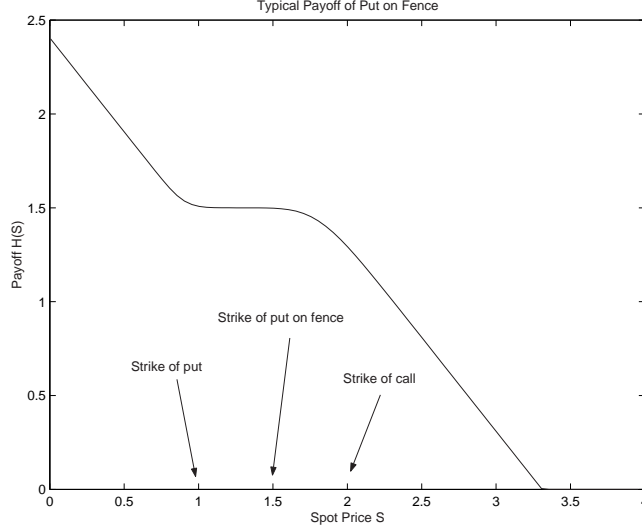
Figure 3.6: Payoff for a put on a fence
The put on a fence pays $(K - (S_T - K_2)^+ - (K_1 - S_T)^+)^+$, where $K_1 < K_2$.

$$
\begin{aligned}
V(S,t) &= e^{-r(T-t)}\mathbb{E}^*\left[F(S_T)|\mathcal{F}_t\right] \\
G(S,t) &= e^{-r(T'-t)}\mathbb{E}^*\left[H(V(S_{T'}))|\mathcal{F}_t\right]
\end{aligned}
$$

where the conditional expectations are taken with respect to the unique *risk neutral* probability measure Pr' equivalent to Pr.

3.4.2   Fence option

Let us recall that an european *call* (*put*) option is a contract in which the holder has the right but not the obligation to buy (sell) some finantial instrument, such as stock, at a previously agreed price, strike price, at some time T in the future. Thus the payoffs of the call and put options at a strike price K are $(S_T - K)^+$ and $(K - S_T)^+$ respectively.

   A *Fence* is an option in which we long (keep or buy) call option at high strike price while we short (lend or sell) a put option at a low strike price. Thus, the payoff of the fence option is

$$(S_T - K_2)^+ - (K_1 - S_T)^+$$

where $K_1 < K_2$. The payoff diagram for a put on a fence is shown in Figure 3.6.

   We will be interested in pricing a put on the fence at strike price K and time of maturity $T' < T$. In practice $K_1 < K < K_2$.

   Let us denote by $C(t,T,K,S)$ and $P(t,T,K,S)$ the price at time T of a call and a put respectively, with maturity time T and strike price K. Let $F(t,T,T',K_1,K_2,S)$ be the price of the fence option at time $t < T$. Then, under the Black and Scholes model, we have that

$$
\begin{aligned}
F(t,T,K_1,K_2,S) &= C(t,T,K_2,S) - P(t,T,K_1,S) \\
&= S\,N(d_1(S,K_2)) - K_2 e^{-r(T-t)}\,N(d_2(S,K_2)) \\
&\quad - K_1 e^{-r(T-t)}\,N(-d_2(S,K_1)) + S\,N(-d_1(S,K_1)) \quad (3.4.7)
\end{aligned}
$$

where

$$
\begin{aligned}
d_1(S, K) &= \frac{\ln(S/K) + (r + \sigma^2/2)(T - t)}{\sigma\sqrt{T - t}} \\
d_2(S, K) &= d_1(S, K) - \sigma\sqrt{T - t}
\end{aligned}
$$

and $N(z)$ is the standard accumulative normal distribution.

The payoff at maturity time $T' < T$ of a Put option on the Fence with Strike price K is

$$
(K - F(T', T, K_1, K_2, S))^+
$$

Let be $\tau' = T' - t$. Then, the price of this compound option is given by

$$
G_t = \frac{e^{-r\tau'}}{\sqrt{2\pi\tau'}} \int\limits_{-\infty}^{\infty} (K - F(T', T, K_1, K_2, Se^{(r - \frac{\sigma^2}{2})\tau'}e^{\sigma x}))^+ e^{-\frac{x^2}{2\tau'}} \, dx \tag{3.4.8}
$$

The expression inside paranthesis is strictly decreasing with respect to x, thus there exists a unique $x^* = x^*(S, \tau')$ such that

$$
K - F(T', T, K_1, K_2, Se^{(r - \frac{\sigma^2}{2})\tau'}e^{\sigma x^*}) = 0
$$

which also implies that

$$
\frac{\partial x^*}{\partial S} = -\frac{1}{\sigma S}.
$$

The last expression will be useful for deriving expressions for the hedging protfolio. The derivation of the formula expoits the techniques introduced in Geske [3]. A full derivation will be provided in a future paper.

$$
G_t = Ke^{-r(T'-t)}N(\tilde{\gamma}_2) - SM(\tilde{\gamma}_1, a_1; \rho) + K_2 e^{-r(T-t)}M(\tilde{\gamma}_2, a_2; \rho) + K_1 e^{-r(T-t)}M(\tilde{\gamma}_2, -b_2; -\rho) - SM(\tilde{\gamma}_1, -b_1; -\rho)
$$

where

$$
\begin{aligned}
\tilde{\gamma}_1 &= \frac{\log\left(\frac{S}{S^*}\right) + \left(r + \frac{\sigma^2}{2}\right)(T' - t)}{\sigma\sqrt{T' - t}} \\
\tilde{\gamma}_2 &= \tilde{\gamma}_1 - \sigma\sqrt{T' - t} \\
a_1 &= \frac{\log\left(\frac{S}{K_2}\right) + \left(r + \frac{\sigma^2}{2}\right)(T - t)}{\sigma\sqrt{T - t}} \\
a_2 &= a_1 - \sigma\sqrt{T - t} \\
b_1 &= \frac{\log\left(\frac{S}{K_1}\right) + \left(r + \frac{\sigma^2}{2}\right)(T - t)}{\sigma\sqrt{T - t}} \\
b_2 &= b_1 - \sigma\sqrt{T - t} \\
\rho &= \sqrt{\frac{T' - t}{T - t}}
\end{aligned}
$$

and where

$$S^{\star} = S e^{x^{\star} + r(T'-t)}.$$

We define M as a bivariate normal distribution with correlation, given by

$$M(\tilde{\gamma}, a; \rho) = \int_{-\infty}^{\tilde{\gamma}} \int_{-\infty}^{a} \frac{1}{2\pi\sqrt{1-\rho^2}} \exp\left(-\frac{(\gamma^2 - 2\rho\gamma\xi + \xi^2)}{2(1-\rho^2)}\right) d\gamma d\xi$$

3.5 Conclusions and Future project

Interpolation methods in yield curve estimation needs to be addressed. It is believed that the method currently used is not optimal. The computer code could also be made easier to use by allowing Excel to be used as a front end. This could be accomplished either with a Matlab back end or through a C++ coded .dll automation file.

The BDT model is easily calibrated, but as mentioned before there are some serious shortcomings that leave us in search of a better model. The Hull-White approach may offer a more robust model and should be examined. The appeal of both models is their accomodation of a time-varying volatility, however they both specify volatility as a deterministic function of time. There is ample evidence of a stochastic volatility, so that should also be considered. Derivatives prices based on th BDT model have been implemented, but so far no calculations of the so-called "greeks" has been performed. Calculations of the greeks will show the senstivity of the price to parameter fluctions and will thus show how to build hedging portfolios. Greeks in a binomial model are easily implemented using a finite-difference scheme.

As we have seen, it is possible to find formulae for the price of basic compound options in the simple Black and Scholes model, where volatility remains constant. The expressions obtained, involve the cumulative distribution function of a binormal vector. It is desirable, and will be left as a future project, to find ways to impliment models to price compound options that take into acount the facts that neither the interest nor the volatility are constant. One possible option is to consider models with stochastic volatility combined with stochastic short rate models.

Bibliography

[1] Anderson, N., Breedon, F., Deacon, M., Derry, A., & Murphy, G. (1996) *Estimating and Interpreting the Yield Curve*. John Wiley & Sons, New York.

[2] Black, F., Derman, E. & Toy, W. (1990). *A One-Factor Model of Interest Rates and its Application to Treasury Bond Options*, Financial Analysts Journal, Jan-Feb, 33-39.

[3] Geske, P. (1979). *The valuation of compound options*, Journal of Finantial Economics, **7**, 63-81.

[4] Heath, D., Jarrow, R. & Morton, A. *Bond Pricing and the Term Structure of the Interst Rates: A New Methodology*, Econometrica, 60, **1**,77-105.

[5] Ho, T.S.Y., and Lee,S.B. (1986). *Term Structure Movements and Pricing Interest Rate Contingent Claims*, Journal of Finance, **41**, 1011-29.

[6] Hull, J. and White,A. *Pricing Interest Rate Derivative Securities*, Review of Financial Studies 3, **4**,573-92.

[7] Hull, J. (1997). *Options, Futures, and Other Derivatives* (3rd edn.) Prentice Hall, Englewood Cliffs, N.J.

[8] Rebonato, R. (1996) *Interest-Rate Option Models* (2nd edn.) John Wiley & Sons, New York.

[9] Willmott, P. (1998) *Derivatives*. John Wiley & Sons, New York.

Report 4

Modeling of Molecular Diffusion in Articular Cartilage Using Fluorescence Microscopy

Mark Kozek[1], Chunhua Lan[2], Kevin Lynch[3],
Abigail Ochberg[4], Chad Wilson[5], Kittipat Wong[6], Xingzhou Yang[7]

Problem Presenter:
Farshid Guilak
Duke University Medical Center

Faculty Consultant:
Sharon R. Lubkin, with the assistance of Holly Leddy[8]

Abstract

Articular cartilage is a hydrated biological soft tissue that acts as a load-bearing surface in joints. The structural matrix in cartilage is comprised of collagen fibers and charged macromolecules (proteoglycans) with embedded cells (chondrocytes) that are responsible for matrix synthesis and repair. As cartilage has no blood vessels, these cells receive all their nutrition by diffusion through the tissue matrix. The maintenance of healthy cartilage and its progressive degradation (osteoarthritis) are highly dependent on the biomechanical and diffusional properties of the extracellular matrix. These properties can be quantified via photobleaching experiments in which fluorescent tracer particles are injected into a region of tissue and their diffusion is monitored using confocal microscopy. The goal is to model the photobleaching experiment for cartilage and characterize the dependence of effective diffusion coefficients on anisotropy and fixed charge density in the extracellular matrix.

---

[1]Wake Forest University
[2]Washington University
[3]East Tennessee State University
[4]University of Michigan
[5]University of Alabama-Birmingham
[6]University of Illinois, Urbana-Champaign
[7]North Carolina State University
[8]Duke University
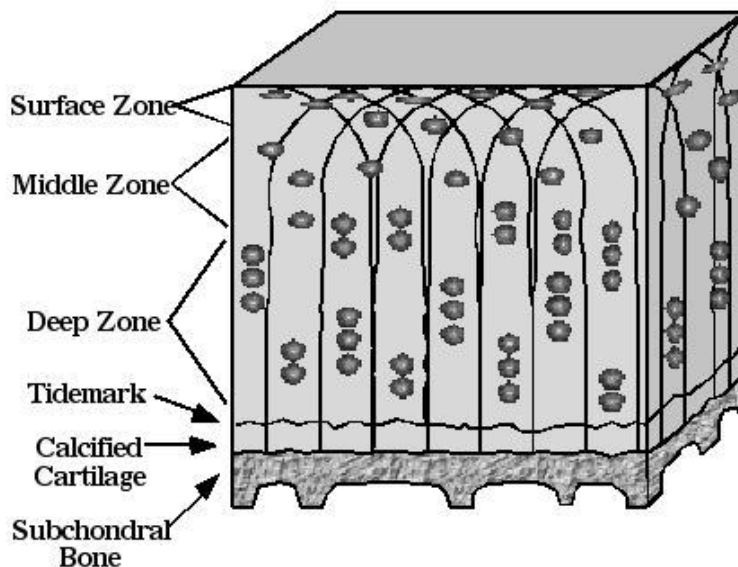
Figure 4.1: Diagram of the structure of articular cartilage taken from the knee. The orientation of collagen fibers varies with depth.

4.1   Introduction and Motivation

One of the goals of the Orthopaedic Research Lab is to study the causes of osteoarthritis (OA) and the factors which influence the degenerative impact of this disease on the body's joints and soft tissues. It is believed that the disease's degenerative effect on articular cartilage is due to a complex combination of both mechanical and biological factors. The lab is working to identify and understand these factors on several length scales. In this particular study, we consider molecular diffusion models on both the microscopic scale of the tissue matrix and the macroscopic scale of a tissue layer.

Articular cartilage is a soft tissue that is composed mainly of water and acts as a load-bearing surface in joints. The structural matrix of articular cartilage is comprised of collagen fibers and proteoglycan (PG) macromolecules with embedded cells that are responsible for matrix synthesis and repair. Since individual cartilage cells respond to changes in their local environment, diffusion through the tissue layer can influence local cell response and, over time, the overall health of the tissue. Two important factors affecting diffusion in cartilage are *anisotropy* and *inhomogeneity* of the structural matrix. Anisotropy results from the fact that orientation of the collagen fibers can vary with location. For example, in articular cartilage of the knee, collagen fibers are randomly oriented in regions away from the surface and bone. Near the surface, the fibers are usually oriented parallel to the surface whereas, near the bone, the fibers are usually oriented normal to the bone (Fig. 4.1). In a tissue layer, non-uniform concentrations of collagen or the negatively-charged PG molecules can lead to spatial variations in diffusion properties. Current knowledge in the field indicates that, in healthy tissue, the PGs are more uniformly distributed throughout the tissue whereas, for OA tissue, PG loss is initiated at the surface and progresses towards the bone (Fig. 4.2). An important goal of diffusion modeling is to facilitate experimental studies that can uncover specific relationships between changes in diffusion properties of the tissue and the progression of OA.

In this study, we consider two models of diffusion in articular cartilage. First, we consider a 2-D model of fluorescence recovery after photobleaching (FRAP) [1], [3], an experiment that is used to determine local effective diffusion coefficients. Our model incorporates the effect of anisotropy in articular cartilage. In the photobleaching experiment, fluorescent tracer particles are introduced into a region of tissue and their diffusion is monitored using confocal microscopy. Knowledge of local diffusion coefficients can be used to quantify the
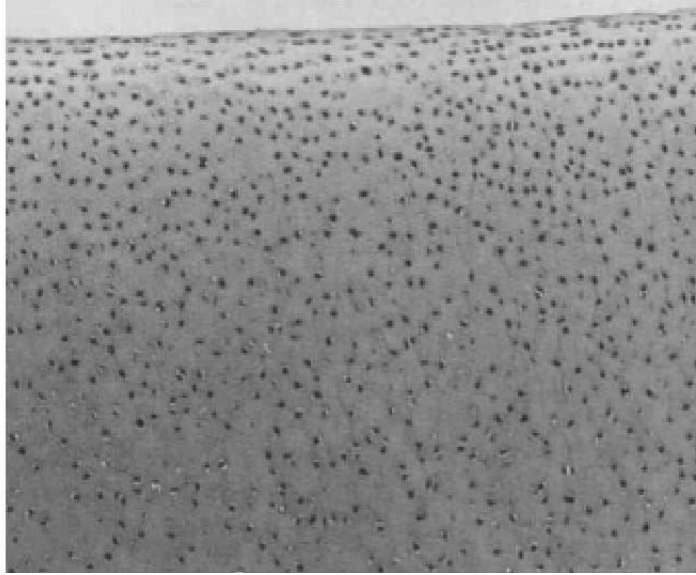
Figure 4.2: Staining for PG concentration in a layer of OA cartilage. The lighter regions near the surface are indicative of a lower PG concentration.

variation of diffusion properties with site in a sample, and across sample populations. Second, we consider a nanoscale-level model of random walks through a domain with a substantial fraction occupied by obstacles, corresponding to parallel fibers in an anisotropic tissue.

4.2 Mathematical Model of Macroscopic Anisotropic Diffusion

In this section, we model the FRAP photobleaching experiment for cartilage for length scales on which the tissue is assumed to be homogeneous but anisotropic. Consequently, the effective diffusion coefficient is assumed to be constant in space but different in each direction. In the FRAP experiment, a small area of tissue is exposed to an intense beam of light from a laser microscope causing irreversible photobleaching of the flourophore in that region. An attentuated laser beam is then used to measure the recovery of the fluorescence in the bleached area due to diffusion of fluorescent molecules from the surrounding unbleached areas.

We assume that the coordinate system is oriented in the principal directions of the diffusion tensor. The differential equation for the anisotropic homogeneous diffusion equation can be written

$$\frac{\partial}{\partial t}c(x,y,t) = \kappa_1 \frac{\partial^2}{\partial x^2}c(x,y,t) + \kappa_2 \frac{\partial^2}{\partial y^2}c(x,y,t) \tag{4.2.1}$$

4.2.1 Analytical Solutions

On an infinite domain, if the initial condition is a delta function of strength c_0 at location $(x,y) = (x_0, y_0)$, or

$$c(x,y,0) = c_0 \delta(x_0, y_0) \tag{4.2.2}$$

then the fundamental solution of the anisotropic diffusion equation,

$$c(x,y,t) = \frac{c_0}{4\pi t \sqrt{\kappa_1 \kappa_2}} e^{-\frac{1}{4t}\left(\frac{(x-x_0)^2}{\kappa_1} + \frac{(y-y_0)^2}{\kappa_2}\right)} \tag{4.2.3}$$

can be obtained by several methods. We used a Laplace transform in t and Fourier transforms in x and y. Mass is conserved, since it is easily verified that the integral

$$\int_{-\infty}^{\infty} \int_{-\infty}^{\infty} c(x,y,t)dxdy = c_0 \tag{4.2.4}$$

for all t. The peak value of $c(x_0, y_0)$ is inversely related to time:

$$c(x_0, y_0, t) = \frac{c_0}{4\pi t \sqrt{\kappa_1 \kappa_2}} \tag{4.2.5}$$

and the level curves are ellipses. For instance, the ellipse at half-maximum height is given by

$$4\ln 2t = \frac{(x-x_0)^2}{\kappa_1} + \frac{(y-y_0)^2}{\kappa_2} \tag{4.2.6}$$

and the level-curve ellipses at a fraction α of the maximum height (height at the center) are given by

$$4\ln \frac{1}{\alpha}t = \frac{(x-x_0)^2}{\kappa_1} + \frac{(y-y_0)^2}{\kappa_2} \tag{4.2.7}$$

Hence for all level curves, the major and minor axes of the ellipse are in a fixed ratio to each other for all time. The ratio of the horizontal extent to the vertical extent of the level-curve ellipse is always $\sqrt{\frac{\kappa_1}{\kappa_2}}$.

It is important to note that if the initial condition is not a delta function (as in the general case), these observations do not hold. For our case of an initially photobleached disk of radius R and density ρ, the exact solution for all time is

$$c(x,y,t) = \int_{-R}^{R} \int_{-\sqrt{R^2-\xi^2}}^{\sqrt{R^2-\xi^2}} \frac{\rho}{4\pi t \sqrt{\kappa_1 \kappa_2}} e^{-1/4t \left(\frac{(x-\xi)^2}{\kappa_1} + \frac{(y-\eta)^2}{\kappa_2} \right)} d\eta \, d\xi \tag{4.2.8}$$

Unfortunately, there is not a clean expression for this integral, though the inner integral can be evaluated, yielding terms containing the error function erf.

For long times and great length scales, the photobleached disk adequately approximates a delta function, and the closed-form solution is a good approximation, with its fixed shape of elliptic level curves. Note, however, that for short times and small length scales (of the order of R), the level curves of the diffusing disk do resemble ellipses, but the curves are *not* of a uniform shape (see Figure 4.4). The ellipses corresponding to the largest values of c are, initially, longer *perpendicular* to the long axis of the ellipses corresponding to small values. This is because the anisotropic diffusion cannot be observed where the gradients are small, i. e. in the center of the photobleached region. The anisotropic diffusion causes fast smearing of the initially circular region in one direction and slower smearing in the other direction, resulting in a very different family of level curves for an initial condition of a delta function versus a circle.

4.2.2   Finite Difference Solutions

In the Fluorescence Recovery After Photobleaching (FRAP) experiment, we have the following equation, where $C(x,y,t)$ denotes the concentration (fluorescence intensity) at the point $(x,y) \in \Omega = [a,b] \times [c,d] (\subset \Re^2)$, a smoothly bounded region representing a sample of cartilage matrix. We assume the domain $\Omega = [a,b] \times [c,d]$ is a square ($b-a = d-c$), and the center of Ω is (x_0, y_0) ($x_0 = \frac{a+b}{2}, y_0 = \frac{c+d}{2}$). We use initial conditions corresponding to the characteristic function of a disk of radius R centered at (x_0, y_0) (Figure 4.3). We assume that the boundary is far enough away that the boundary conditions are unimportant; for ease of programming, we take the boundary condition to be Dirichlet.

$$C_t = \kappa_1 C_{xx} + \kappa_2 C_{yy} \tag{4.2.9}$$

$$\text{IC: } C(x,y,0) = \begin{cases} C_0, & \text{if } (x,y) \text{ is in the circle } (x-x_0)^2 + (y-y_0)^2 \le R^2 \\ 0, & \text{otherwise} \end{cases} \tag{4.2.10}$$

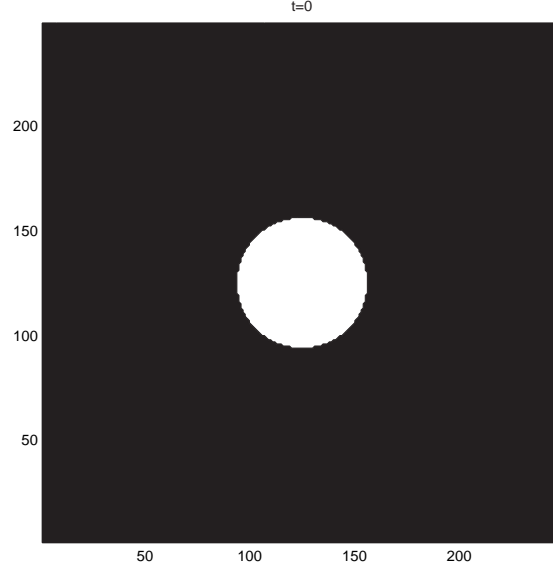$$\text{BC: } C(x,y,t) = 0. \qquad (x,y) \in \partial\Omega \tag{4.2.11}$$

Figure 4.3: Initial conditions. Domain $[a, b] \times [c, d] = [1, 64] \times [1, 64]$. Radius of circle $R = 8$. The disk has concentration $C_0 = 10$ and the blank region has $C = 0$.

We use the alternating direction implicit (ADI) method to solve (4.2.9) – (4.2.11). If κ_1 and κ_2 are constants, ADI is unconditionally stable, as is easily seen by von Neumann analysis for two dimensions. To implement ADI methods on the square domain $\Omega = [a, b] \times [c, d]$, we begin with a grid consisting of points (x_i, y_j), given by $x_i = a + (i-1)*h$, $y_j = c + (j-1)*h$, where $h = \delta x = \delta y = (b-a)/N$, and $i = 1, 2, \cdots, N+1$, $j = 1, 2, \cdots, N+1$. The scheme is as follows,

$$C_{ij}^{n+\frac{1}{2}} = C_{ij}^n + \frac{k}{2h^2}\left(\kappa_1(C_{i-1,j}^n - 2C_{ij}^n + C_{i+1,j}^n) + \kappa_2(C_{i,j-1}^{n+\frac{1}{2}} - 2C_{ij}^{n+\frac{1}{2}} + C_{i,j+1}^{n+\frac{1}{2}})\right)$$
$$C_{ij}^{n+1} = C_{ij}^{n+\frac{1}{2}} + \frac{k}{2h^2}\left(\kappa_1(C_{i-1,j}^{n+\frac{1}{2}} - 2C_{ij}^{n+\frac{1}{2}} + C_{i+1,j}^{n+\frac{1}{2}}) + \kappa_2(C_{i,j-1}^{n+1} - 2C_{ij}^{n+1} + C_{i,j+1}^{n+1})\right)$$
$$i = 2, 3, \cdots, N, \quad j = 2, 3, \cdots, N$$

With this method, each of the two steps involves diffusion in both the x- and y-directions, and can be shown to give first-order-accurate approximation over time $k/2$. However, the combined method is second-order-accurate over the full time step.

We consider the following domain $[1, 64] \times [1, 64]$. The concentration is $C_0 = 10$ in the circular center with radius $R = 8$, and zero outside. Simulations were run in Fortran 90 and are displayed via Matlab. Figure 4.4 presents a time series of the evolution of the concentration of photobleached molecules (white indicates high photobleached concentration).

Notice $\kappa_1 = 1 < \kappa_2 = 6$, and the diffusion speed in y-direction (vertical) is faster than that in x-direction (horizontal). One goal was to produce a measure or measures that an experimentalist can also measure and use to determine the anisotropy in a specific sample. In the hopes of determining some metric for the eccentricity of the disks (in the absence of a neat closed-form solution), we took slices of the domain parallel to the principal axes of diffusion (x and y) (Figure 4.5). We use 2-norm to measure the difference of the concentrations in the x cross-section $C[x]$ at $y = y_0$ and in y cross-section $C[y]$ at $x = x_0$

$$M = \int_{-\infty}^{\infty} (C[x](\xi - x_0) - C[y](\xi - y_0))^2 \ d\xi \tag{4.2.12}$$

M is a function of time and of anisotropy, as illustrated in Figure 4.6. For example, a fixed ratio, say $\kappa_1 = 1, \kappa_2 = 6$ (the curve with stars), initially M increases, reaching a peak at $t = 6$, then decreases.
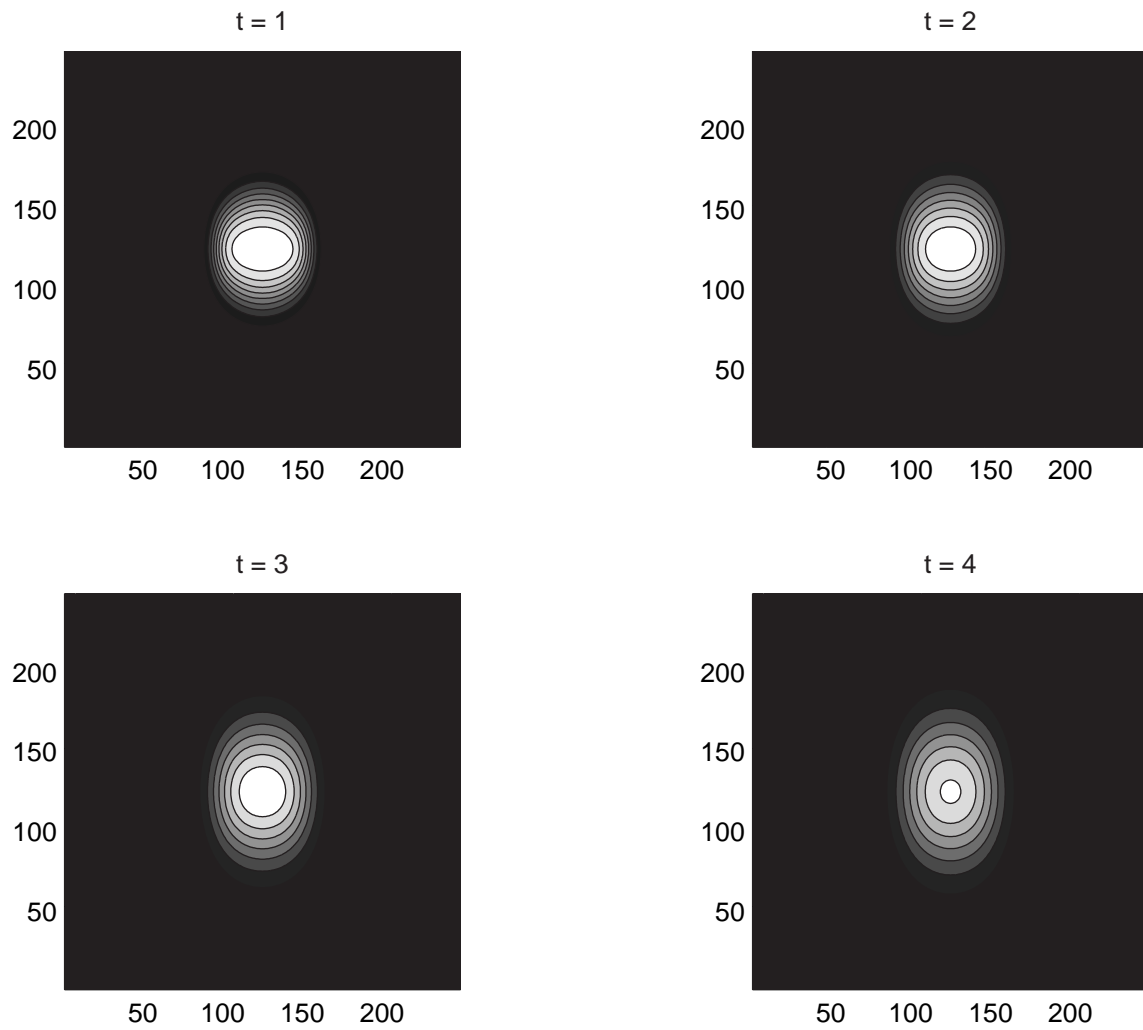
Figure 4.4: Contour plots of C at different times, by ADI method. $\kappa_1 = 1, \kappa_2 = 6$
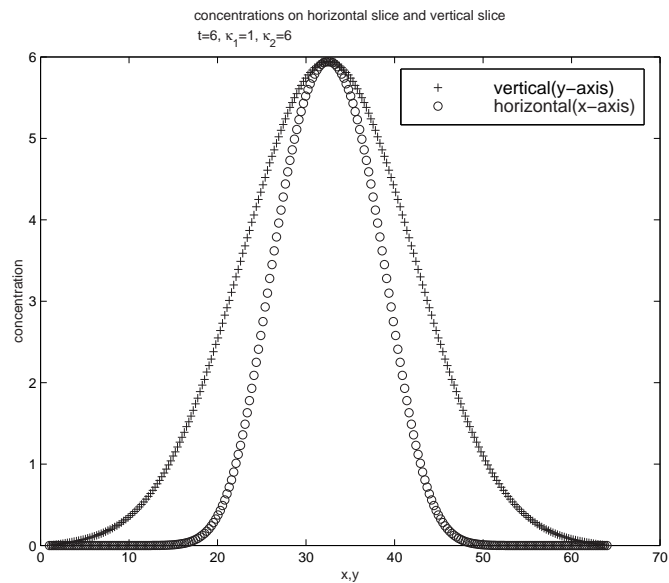
Figure 4.5: Comparison of concentrations on horizontal and vertical slices through the center.
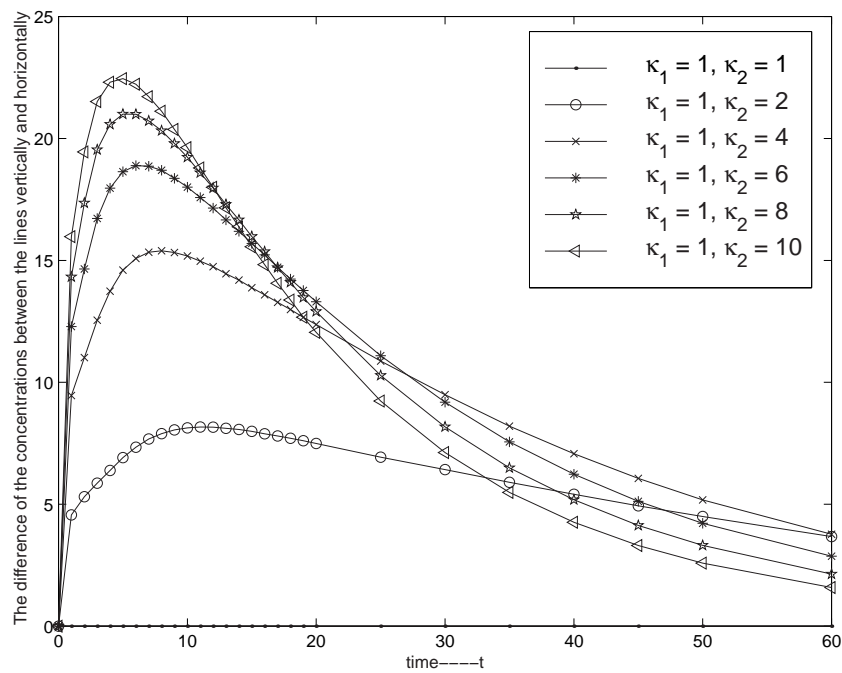

Figure 4.6: Norm of difference in profiles in the two principal directions of diffusion $M(t)$. For the isotropic case (small dots) there is no difference in profiles. For anisotropic cases, the greatest observable difference in profiles occurs a short time after photobleaching. Note that for each doubling of the ratio of diffusion coefficients, the peak value of norm M also appears to double.
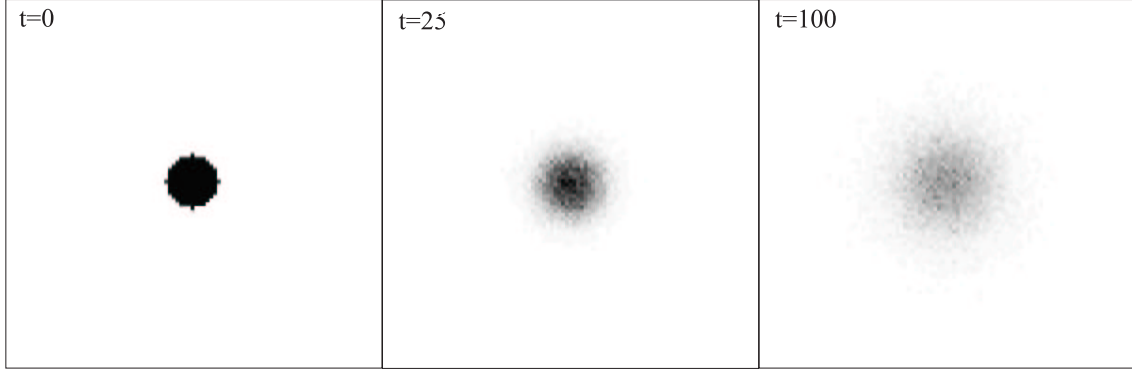
Figure 4.7: Random walk simulation of FRAP experiment. Domain 101 by 101, bleach spot radius $R = 11$, $\kappa_1 = \kappa_2 = 1$.

4.2.3   Random Walk Solutions

We investigated another simulation technique, that of a random walk. On the square lattice, walkers were released with equal probabilities from the interior of the initial disk. Each had a probability of moving to the right or left, up or down, proportional to the diffusion coefficient in that direction (x or y). The random walk technique was equivalent to a Monte Carlo simulation of the underlying PDE (4.2.1); the PDE is equivalent to the expectation for the underlying random walk process. See Figure 4.7.

By analogy with M above, we define a parameter, the Anisotropy Parameter (AP) that would reflect that shape change and be easily correlated with the ratio of the horizontal and vertical diffusion coefficients. The AP is calculated by subtracting the central vertical and horizontal concentration profiles, and summing the square of those distances (Figure 4.8).

$$AP = \sum (C[x](\xi - x_0) - C[y](\xi - y_0))^2 \tag{4.2.13}$$

AP is the discrete version of the norm M defined above. The AP varies with time and with the ratio of the horizontal and vertical diffusion coefficients. For a circular initial bleached region, the AP starts at zero at time zero, where there is radial symmetry in the bleached spot. For isotropic diffusion, the AP quickly reaches a limiting value which depends on the coarseness of the simulation. For an infinitely fine δt, AP would be zero for all time in the isotropic case. For anisotropic diffusion, the bleached spot elongates over time in the direction of fastest diffusion, creating differences in the horizontal and vertical concentration profiles, and thus an increase in the anisotropy parameter, as observed in the finite difference simulations (Section 4.2.2). The difference between the horizontal and vertical concentration profiles then starts to decay because the long ends of the bleached spot are now approaching the concentration of the surrounding unbleached areas. After a long time, AP must decay back to zero because the bleached spot disappears.

The AP should increase with the ratio of the diffusion coefficients. Thus, as the diffusion becomes more anisotropic, the AP increases. Because the all APs must start at zero and decay to zero; the AP will only reflect the different ratios of diffusion coefficients at some of the intermediate time steps.

The AP was calculated from the random walk model averaged over 100 simulations for a 101 by 101 square grid with a bleached disk of $R = 7$ starting with 10 particles per square in the bleached spot going out to 300 time steps for 6 different diffusion coefficient ratios. The simulations still show considerable random fluctuations when averaged over such a relatively low number, but this may be useful in mimicking the kind of noise found in actual data (Figure 4.9). The simulations do follow the predicted trends: the AP increases and then decreases with time, and the AP is generally higher for higher ratios of diffusion coefficients. Curiously, the time at which the peak AP occurs appears to *increase* with the ratio of the diffusion coefficients (cf. Figure 4.6). The relationship between peak anisotropy parameter and the ratio of the diffusion coefficients is
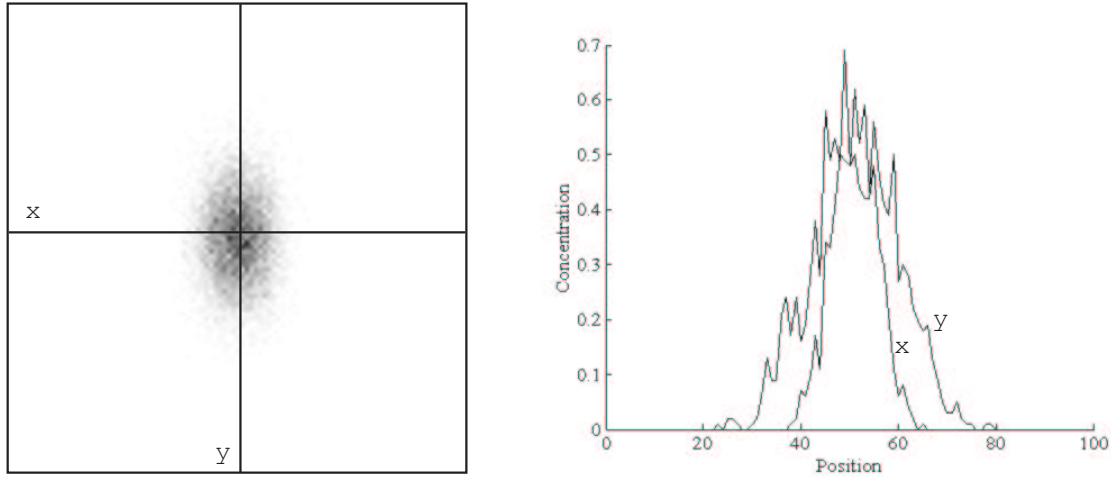
Figure 4.8: Left panel shows the results of a random walk simulation of a FRAP experiment where the diffusion coefficient in the y direction is 6 times greater than the diffusion coefficient in the x direction. The panel on the right shows the concentration profile along the x and y axes as drawn on the left side. The anisotropy parameter is the sum of the squared difference between the two curves.

strikingly linear over the range examined (Figure 4.10):

$$\kappa_1/\kappa_2 = 7.7709 * AP - 2.324 \qquad (4.2.14)$$

The experimentalist can use this relationship to calculate the ratio of the diffusion coefficients from the AP. There are, however, a number of limitations of our AP. If the amount of variation in these simulations is representative of the variation in the experimental data, this method cannot effectively discriminate small amounts of anisotropy ($\kappa_1/\kappa_2 < 2$). As currently described, it is dependent on the amount of area around the bleached spot that is analyzed (i.e. if the bleach spot is large relative to the total grid size, then the peak AP will be larger than it would be if the bleach spot is smaller). This problem is easy to address by simply setting the AP measurement to only include a fixed distance surrounding the bleached spot.

4.2.4 Comparison between stochastic and ADI solutions

The results from the stochastic model and the ADI model were compared to confirm that both models were approaching the same solution. When the stochastic model's results are averaged over enough iterations, its solution should converge to the ADI model results.

We held the following conditions constant in both methods: initial conditions ($R = 3$, $\rho = 10$), matrix dimensions ($N = 63$), number of particles per cell of the center (10), time ($t =0$ to 10), and the horizontal/vertical probabilities (0.5, 0.5).

For the stochastic model, we varied the number of runs, and then calculated its "error factor" with respect to the ADI model. The stochastic model was run for the following sample sizes: 10, 50, 100, 500, 1000, 5000, and 10000.

The error factor was calculated as follows. For each specific cell, (i, j) of the stochastic and the ADI matrix,

$$E = \sum_{i,j} [C_{stochastic}(i,j) - C_{ADI}(i,j)]^2/(N^2) \qquad (4.2.15)$$

The units for E are particles per cell.

These results suggest that at larger sample sizes, the results of the stochastic and the ADI models become closer, but they don't converge completely, since there remains a residual error from the grid size (Figure 4.11).
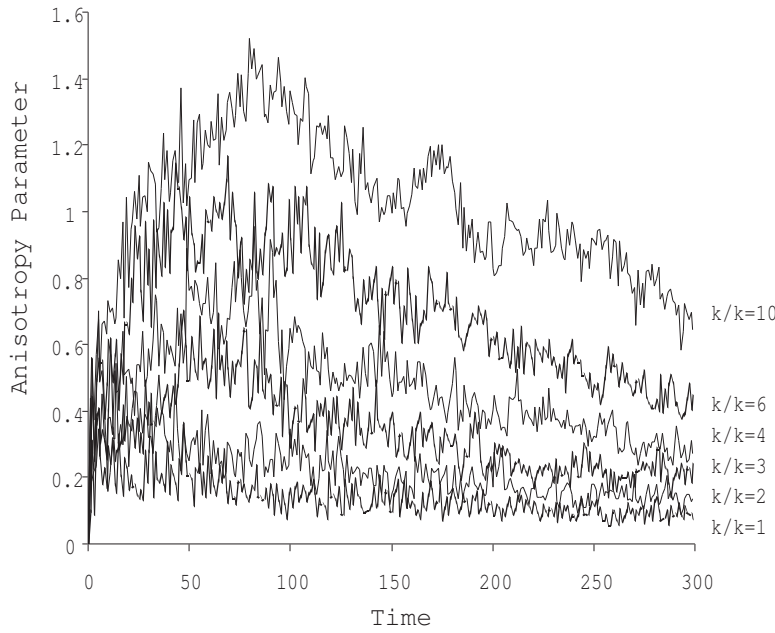
Figure 4.9: Anisotropy parameter AP varies with time and with ratio of diffusion coefficients. Lines are average results of 100 random walk simulations for a 101 by 101 square grid with an $R = 7$ bleached disk starting with 10 particles per square. Ratio of horizontal and vertical diffusion coefficients is given alongside each line.
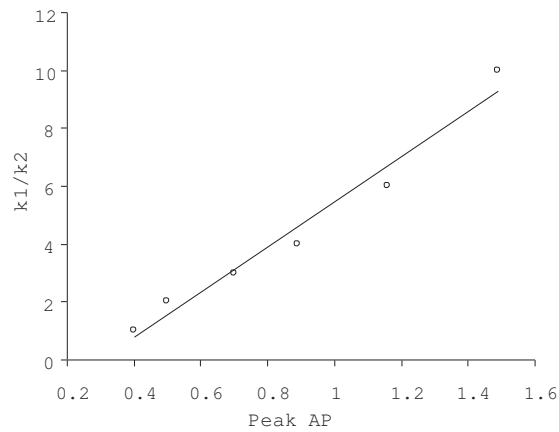

Figure 4.10: Peak anisotropy parameter AP varies linearly with ratio of diffusion coefficients. Data points are from random walk simulations (see text for details). Fitted line is $\kappa_1/\kappa_2 = 7.7709 * AP - 2.324, R^2 = 0.97$.
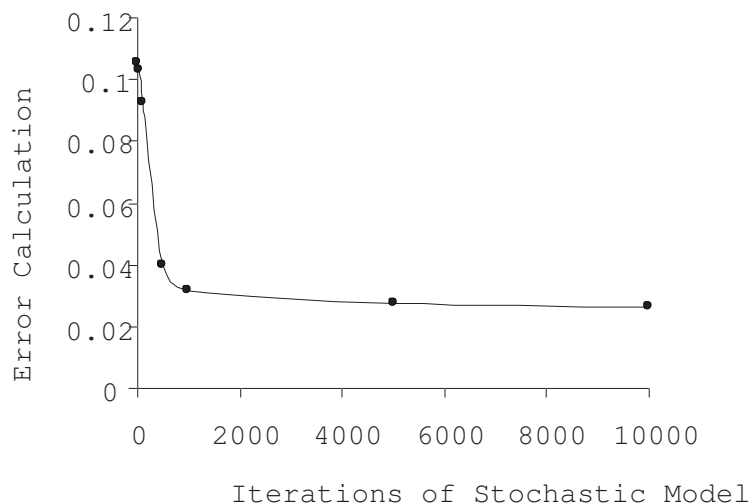
Figure 4.11: Error calculation versus number of iterations of the stochastic model shows that the difference between the stochastic and ADI methods decreases with increasing iterations of the stochastic model.

4.3   Simulation of Nanoscale Mechanisms of Anisotropic Diffusion

Since one of the main goals of our study is to be able to use the FRAP technique to measure the anisotropy of a material, we need to understand the relationship between the microstructure of the material and the observed diffusion coefficients of photobleached molecules [2].

In articular cartilage, collagen fibers are organized with a distinct structural arrangement that that varies with distance from the tissue surface (Figure 1). As collagen is believed to provide cartilage with its tensile mechanical properties, anisotropy and inhomogeneity in the tissue's mechanical properties are believed to reflect the collagen fiber orientation. However, the influence of this structure on the diffusion properties of the tissue are not known, and it is hypothesized that the orientation of the collagen fibers may lead to differences in the diffusion coefficients in the x- and y-direction. This behavior can be caused by the presence of ordered diffusion barriers, such as fibers. The goal of this portion of the project was to determine under what conditions the presence of fibers can cause anisotropy in diffusion.

To that end, we simulated random walkers on a 2D domain which included a substantial fraction of nonintersecting obstacles, corresponding to aligned fibers (Figure 12). We compiled statistics on the average distance traveled over time in the x and y directions, to determine the effective diffusion coefficients in each direction as a function of the parameters governing the fiber array (such as density and volume fraction). From this we calculated the diffusion coefficients in the x- and y-directions. The ratio of the two diffusion coefficients reflects the anisotropy. We examined how the anisotropy changed with fiber density and geometry.

The aspect ratio (length over width) of a fiber tends to increase anisotropy (Figure 13). This occurs because as fiber length increases, there is an increase in the vertical length which a molecule must travel before it can travel horizontally to get around the fiber. The data show a drop in anisotropy above an aspect ratio of about 35. This is probably an artifact of the way the model was constructed, and at that fiber size, the molecules got trapped between the fibers and did not move much at all.

The percent of space that is occupied by fibers also increases the anisotropy (Figure 14). If the fibers are spaced far apart, the molecules will not hit them very often, so they will have little effect. The degree to which fiber density increases anisotropy depends strongly on the aspect ratio (length to width ratio) of the fibers. If the fibers are longer, it is harder for the molecules to move across them because there are fewer gaps allowing
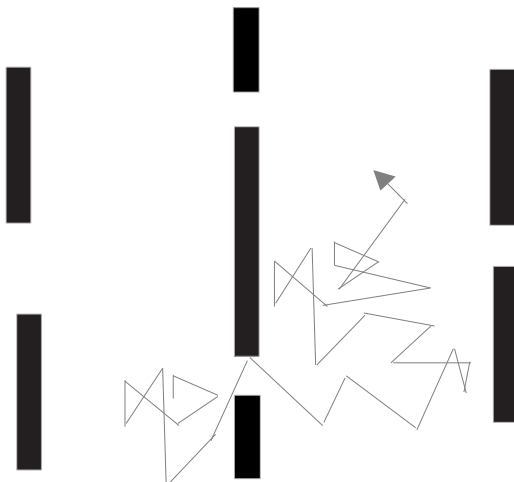
Figure 4.12: Path of a randomly moving molecule faced with fiber-like barriers. The molecule will face fewer barriers moving vertically than moving horizontally.
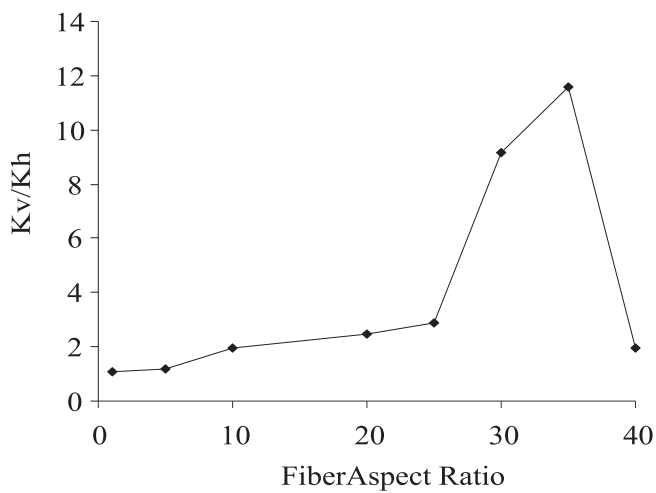

Figure 4.13: Ratio of vertical and horizontal diffusion coefficients (κ_v/κ_h) calculated from random walk simulations versus the aspect ratio of the fibers acting as diffusional barriers in the simulations.

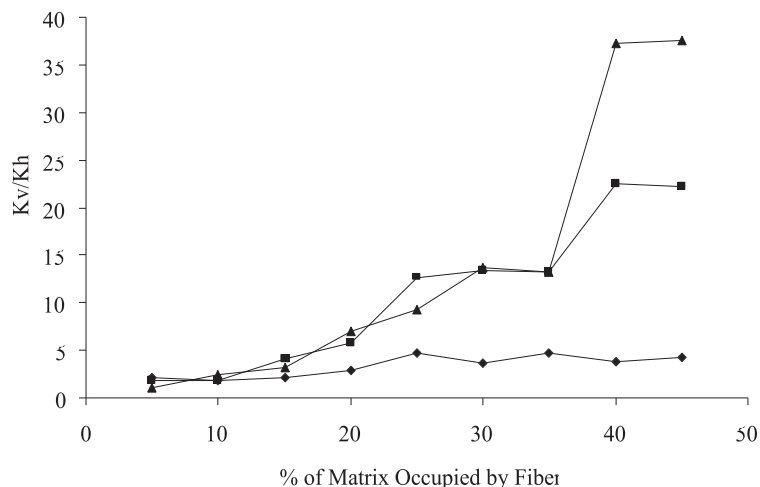Figure 4.14: Ratio of vertical and horizontal diffusion coefficients (κ_v/κ_h) calculated from random walk simulations versus the percent of matrix area occupied by fibers. Each line represents a different fiber aspect ratio (triangles 20:1, squares 15:1, diamonds 10:1).

horizontal movement.

A tissue, such as cartilage, with a relatively low fraction (20% by wet weight) of relatively long fibers would show some anisotropy by the 2-D model. However, a 3-D model is required to generate any realistic conclusions. We can say in a general 2-D system anisotropy is increased with increasing fiber aspect ratio and with fiber density.

4.4   Discussion

We made several observations about anisotropic diffusion which will be useful in guiding photobleaching microscopy experiments to measure material properties in articular cartilage.

First, we noted (section 4.2.1) that the diffusion from a sudden point source (delta function at $t = 0$) is described by level curves which are always ellipses. Furthermore, the major and minor axes of the ellipses are always (for all time) in the same ratio as the square roots of the diffusion coefficients in the principal directions. Thus any sufficiently fast and sufficiently localized photobleaching will leave a signature which conveys a direct measurement of the local anisotropy.

We could imagine a microscopy technique which photobleached a regular array of spots on a cartilage sample. The spots would rapidly deform into localized ellipses, providing immediate visual display of the local direction and magnitude of the anisotropy (Figure 15).

An important caveat about the 2-D nanoscale model is that it is not a realistic representation of what happens when a molecule diffuses through a tissue and will greatly over estimate the anisotropy. When a particle hits a fiber in 2-D, it must go all the way around the long dimension of the fiber to get around it, whereas in 3-D, to get around a barrier, the particle could go the long way or it could go around the fiber in the third dimension. The 2-D model is a pilot step towards a 3-D model.
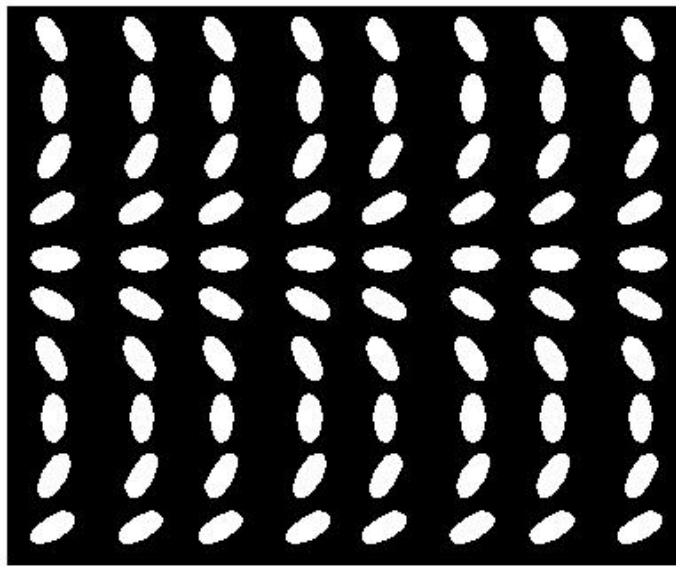
Figure 4.15: Hypothetical observation of an array of small photobleached spots on a material whose anisotropy varies in space.

Bibliography

[1] D. Axelrod, D. E. Koppel, J. Schlessinger, E. Elson, and W. W. Webb (1976), *Mobility measurement by analysis of fluorescence photobleaching recovery kinetics*, Biophys J., 16:1055-1069.

[2] J. Han and J. Herzfeld (1993) *Macromolecular diffusion in crowded solutions*, Biophys J, 65:1155-1161.

[3] T. K. L. Meyvis, S. C. de Smedt, P. van Oostveldt, and J. Demeester (1999), *Fluorescence recovery after photobleaching: A versatile tool for mobility and interaction measurements in pharmaceutical research*, Pharmaceutical Res., 16(8):1153-1162

Report 5

Modeling Control of HIV Infection Through Structured Treatment Interruptions with Recommendations for Experimental Protocol

Shannon Kubiak[1], Heather Lehr[2], Rachel Levy[3], Todd Moeller[4], Albert Parker[5], Edward Swim[6]

Problem Presenter:
Sarah Holte
Fred Hutchinson Cancer Research Center

Faculty Consultant:
H. Thomas Banks, with the assistance of Brian Adams and David Bortz

Abstract

Highly Active Anti-Retroviral Therapy (HAART) of HIV infection has significantly reduced morbidity and mortality in developed countries. However, since these treatments can cause side effects and require strict adherence to treatment protocol, questions about whether or not treatment can be interrupted or discontinued with control of infection maintained by the host immune system remain to be answered. We present sensitivity analysis of a compartmental model for HIV infection that allows for treatment interruptions, including the sensitivity of the compartments themselves to our parameters as well as the sensitivity of the cost function used in parameter estimation. Recommendations are made about collecting data in order to best estimate the most sensitive parameters in the model. Furthermore, we present parameter estimates using simulated data.

5.1 Introduction

Highly Active Anti-Retroviral Therapy (HAART) has been highly successful in reducing the viral load in HIV patients. However, the combined expense and side effects of this therapy have had a negative impact on drug

---

[1] Towson University
[2] University of Texas at Austin
[3] North Carolina State University
[4] Georgia Institute of Technology
[5] Montana State University - Bozeman
[6] Texas Tech University

distribution and patient compliance. Studies indicate [1], [2] that Structured Treatment Interruptions (STI) which involve periods of time during which patients receive no medication, may actually be beneficial to the patient. These interruptions stimulate the immune system and potentially induce a state in which the immune system controls the viral infection.

In this workshop, we examined a modified version of the Wodarz-Nowak model for HIV infection dynamics. As a step toward finding a treatment protocol involving STI that will induce host control of the virus, we performed a sensitivity analysis of our model. This sensitivity analysis suggests future experimental design to test the model and theory of STI for control of HIV. Our investigation sought the most sensitive parameters and compartments as well as the optimal time schedule for data collection. We also considered the parameter identification problem that would use data to estimate parameters in the model.

In Chapter 2, we will describe the modifications made to the Wodarz-Nowak model and the effects those changes make to the dynamics of the problem. In Chapter 3 we describe the sensitivity analysis that was conducted and the resulting recommendations for experimental protocol. Finally, in Chapter 4 we present the parameter estimation results we computed using simulated data.

5.2   Description of the Modified Wodarz-Nowak Model

The goal of this workshop was to examine a modified version of the Wodarz-Nowak model [3] for HIV infection dynamics. The modification involves the addition of an extra compartment, V, to represent the viral load present. The change in viral load over time is modeled as a difference of a linear birth rate dependent on the number of infected cells and a death rate of the short-lived virus.

5.2.1   ODE Model

The model is a coupled system of five ordinary differential equations with twelve parameters. Here the state variables describe compartments in the biological system. Our modification of the Wodarz-Nowak Model for HIV infection dynamics is

$$
\begin{aligned}
\dot{X} &= \lambda - d\,X - \beta\left[1 - f\,u(t)\right]XV \\
\dot{Y} &= \beta\left[1 - f\,u(t)\right]XV - a\,Y - p\,YZ \\
\dot{W} &= c\,XYW - cq\,YW - bW \\
\dot{Z} &= cq\,YW - h\,Z \\
\dot{V} &= k\,Y - \mu\,V,
\end{aligned}
$$

where the compartments are

$$
\begin{aligned}
X &= \text{Uninfected T helper cells} \\
Y &= \text{Infected T helper cells} \\
W &= \text{Immune Precursors Cytotoxic T Lymphocyte} \\
Z &= \text{Immune Effector Cytotoxic T Lymphocyte} \\
V &= \text{Free Virus,}
\end{aligned}
$$

and the parameters are

$$
\begin{aligned}
\lambda &= \text{Target cell production rate} \\
d &= \text{Natural death rate of target cells} \\
\beta &= \text{Rate of viral replication} \\
f &= \text{Treatment efficacy factor} \\
a &= \text{Natural death rate of Infected cells} \\
p &= \text{Death rate of infected cells due to immune response} \\
c &= \text{CTL activation rate} \\
q &= \text{Growth rate of CTL effectors due to infected cells and CTL precursors} \\
b &= \text{Natural death rate of CTL precursors} \\
h &= \text{Natural death rate of CTL effectors} \\
k &= \text{Growth rate of virions due to infected cells} \\
\mu &= \text{Natural death rate of virions.}
\end{aligned}
$$

In the model, we assume the virus instantaneously approaches T-cells with no time lag for diffusion. It is important to note that such a delay probably exists, but is not modeled by our system. Also note that the compartment V only represents virions that can infect uninfected cells (represented by the X compartment). In this model, immune precursors (W) are stimulated by infected cells, not by the virus. Figure 1 visually represents the relationship between the compartments in the modified Wodarz-Nowak Model.

5.2.2 Incorporation of Structured Treatment Interruption (STI) in the Model

Structured treatment interruptions are planned times that patients will cease taking medication. In this model, it is assumed that STI is incorporated only after the patient has been on medication long enough to maintain a low level of viral load. Then, during a treatment interruption, the virus level rises and consequently stimulates the immune system. The refreshed immune system may (hopefully!) then suppress the viral load without the aid of continued medication.

The function $u(t)$ represents the incorporation of STI in our model. Values of $u(t)$ range from 0 to 1, with 0 representing no treatment and 1 representing full treatment. Thus $u(t)$ effectively reduces the infectivity parameter (β) of the system as it grows from 0 to 1. In our analysis we considered a periodic STI schedule, $u(t)$, of the form shown in Figure 2.

The parameter f represents the efficacy of the treatment, for which we assumed a value of 0.75. It is important to note that independent investigations by Brian Adams (a graduate student advising our group) suggest that the behavior of the model is radically different for $f < 0.95$ than for $f > 0.95$.

5.2.3 Equilibria and Choice of Parameter Values

The parameters in our work are derived from those used by Wodarz and Nowak, whose model has a basic viral reproductive ratio, $R_0 = \beta\lambda/ad = 25$. As mentioned earlier, our model consists of their model together with a compartment for free virus. Adding this free virus compartment results in a basic viral reproductive ratio, $R_0 = \beta\lambda k/ad\mu$. To calculate parameters for our modified model, we made three assumptions:

1. the same basic viral reproductive ratio ($R_0 = 25$);

2. a ratio of our new parameters: $k/\mu = 25$, since accepted values for these parameters are $k \in [20, 250]$ and $\mu = 1$; and

3. $\beta k = 0.5$ for our new parameter set, where 0.5 is the value of β used by Wodarz and Nowak.
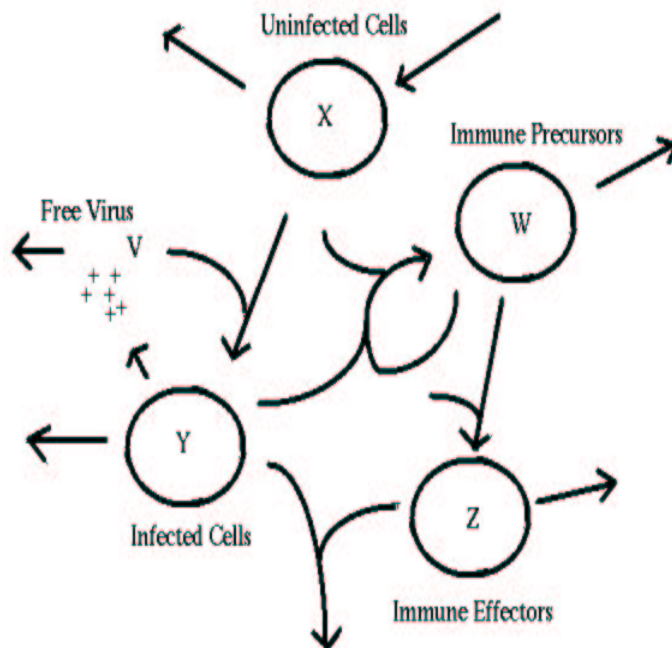
Figure 5.1: Relationship between compartments in the modified Wodarz-Nowak model. Uninfected T-helper cells X are infected by free virus V to become infected T-helper cells Y. The infected cells stimulate the immune precursors W to become immune effectors Z that can in turn kill the infected cells. The model includes other relationships, but these are the primary interactions between compartments in the model.
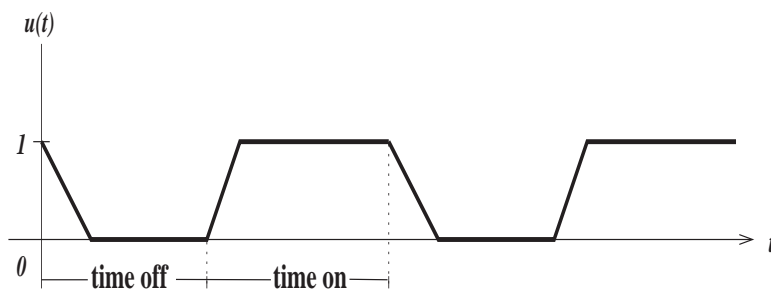

Figure 5.2: The function u(t) which incorporates STI in the model. Our work assumes a drug rise time of two days and decay time of four days.

The last condition (3) is enforced because in our model, the dynamics for V depend largely on kY. Consequently the dynamics for Y, which include βXV, indirectly depend on βk. These assumptions yield the following parameters, which were used in our simulations.

Parameter	Value
λ	1
d	0.1
β	0.02
a	0.2
p	1
c	0.027
q	0.5
b	0.001
h	0.1
k	25
μ	1
f	0.75

This model has multiple equilibria for all parameter sets $\mathbf{q} = [\lambda, d, \beta, a, p, c, q, b, h, k, \mu, f]^T$, but the stability of each of these equilibria depends on the choice of parameters. For the choice of parameters used in the simulations ($\mathbf{q_0}$), there are two stable equilibria which correspond to the success or failure of the immune system to control infection. The equilibrium values corresponding to our parameters are given in the following table.

Compartment	1st Equilibrium (virus dominates)	2nd Equilibrium (immune system dominates)
X	0.4	9.8
Y	4.8	.004
W	0	8751
Z	0	4.7
V	120	0.10

Our stability analysis is localized at the point $\mathbf{q_0}$ in the parameter space. We linearize the non-linear system about an equilibrium point, then carry out an eigenvalue analysis. [4] This produces only local stability results. We would expect different numerical results if we localized our study at different parameter values. In solving the parameter identification problem, values for our parameter vector $\mathbf{q}$ were chosen from the set Q_{ad}, the space of valid values for $\mathbf{q}$.

5.3 Analysis

Because the modified Wodarz-Nowak model is complex, including five compartments and twelve parameters, it is necessary to establish priorities about which parameters to estimate and which compartments to try to observe. A sensitivity analysis informs this prioritization, which can aid in experimental design.

The sensitivity analysis has three goals. First, in order to choose a subset of parameters to estimate, it is necessary to determine which parameters to play a significant role in the dynamics of the model. Second, in order to suggest a timing schedule for collection in the experimental protocol, it is necessary to determine which times are most critical for data collection. Third, in order to determine which compartments are necessary to

observe and whether or not their observation can be combined, it is necessary to determine which combinations of compartments play a significant role in the dynamics of the model.

5.3.1   Derivation of the Sensitivity Matrix

In this subsection, we find an equation for the sensitivity matrix, $\partial z/\partial q$, from our model. This will suggest the sensitivity of the states to the parameters.   Recall   that   our   model   has   five   compartments, $\mathbf{z} = [X, Y, W, Z, V]$ and twelve parameters, $\mathbf{q} = [\lambda, d, \beta, a, p, c, q, b, h, k, \mu, f]$.   We can therefore represent our model by

$$\dot{\mathbf{z}} = f(\mathbf{z}(t); \mathbf{q}),$$

$$\mathbf{z}(0) = \mathbf{z_0}.$$

Differentiating with respect to q and formally passing the time derivative through yields

$$\left(\frac{\dot{\partial z}}{\partial q}\right)(t) = \frac{\partial f}{\partial z}(z(t, q_0); q_0) \cdot \frac{\partial z}{\partial q} + \frac{\partial f}{\partial q}(z(t, q_0); q_0).$$

This can be written as an $n \times m$ matrix system ($n = 5, m = 12$) of ODEs for the sensitivity matrix $r(t) = \partial z/\partial q$

$$\dot{r}(t) = A_0(t)\, r(t) + g_0(t),$$

$$r(0) = 0,$$

where

$$A_0 = \frac{\partial f}{\partial z}(z(t, q_0); q_0)$$

and

$$g_0 = \frac{\partial f}{\partial q}(z(t, q_0); q_0).$$

The solution to this system of ODEs yields the local system sensitivity about the point $\mathbf{q_0} \in Q_{ad}$ which we will use to examine the sensitivity of the states with respect to the parameters over time.

5.3.2   Forward Solution of the ODE

Note that the solution of the matrix system of ODEs depends on having a solution to the original model of ODEs (see equation for $\dot{\mathbf{z}}$ above). Therefore, to employ our sensitivity results, we first must be able to solve the original model. To this end, we employed the MATLAB stiff ODE solver *ode15s*. We used parameters values $\mathbf{q_0}$ as given in the table in Section 2.3 and initial condition $\mathbf{z}_0 = [10, 0.3, 0.008, 0.001, 7.5]$. Solutions were found over different time spans, e.g., 100 days and 500 days.

5.3.3   Sensitivity of $\frac{\partial J}{\partial \mathbf{q}}(\mathbf{q_0})$ Based on the Cost Function $J(q)$

The cost function,

$$J(\mathbf{q}) = \frac{\sum_i |\log(C * \mathbf{z}(t_i, \mathbf{q})) - \log(C * \hat{\mathbf{z_i}})|^2}{\sigma_i^2},$$

gives a measure of how well the values predicted by the model for $\mathbf{z}(t_i)$ fit the experimental data $\mathbf{z_i}$. Therefore, analyzing

$$\frac{\partial J}{\partial \mathbf{q}}(\mathbf{q_0}) = \sum_i 2 \frac{\log(C * \mathbf{z}(t_i, \mathbf{q_0})) - \log(C * \hat{\mathbf{z_i}})}{\sigma^2 \cdot (C * \mathbf{z}(t_i, \mathbf{q_0}))} \cdot \left(C * \frac{\partial \mathbf{z}}{\partial \mathbf{q}}(t_i, \mathbf{q_0})\right)$$

gives us an idea of how sensitive this fit is to small changes in any one of the parameters. Since we did not have experimental data with which to work, we instead used the solution to the original system of ODEs found using the MATLAB stiff solver *ode15s* and added random noise to it in the following manner:

$$\log \hat{\mathbf{z_i}} = \log \mathbf{z}(\mathbf{t_i}) + \eta \epsilon(t_i),$$

where $\hat{\mathbf{z_i}} =$ simulated data at time t_i, $\eta =$ error range percentage, and $\epsilon(t_i)$ is randomly distributed according to an N(0,1) normal distribution.

Figure 3 depicts the values we obtained for $\log |\partial J/\partial \mathbf{q}|$ over 100 different simulated data sets. This particular plot represents results for the system with no treatment (i.e., $u = 0$). We also carried out the same analysis for the system under the periodic treatment interruption mentioned earlier in the paper and found the the same four parameters β, a, p, c were still the most sensitive and that the drug efficacy f became the fifth most sensitive parameter.

Throughout the paper, the boxplot of a data set is a box and whisker plot where the box has lines at the lower quartile, median, and upper quartile values. The whiskers are lines extending from each end of the box to show the extent of the rest of the data. The whiskers end at the data points that lie just within 1.5 of the interquartile range (IQR). Outliers are data with values beyond the ends of the whiskers.
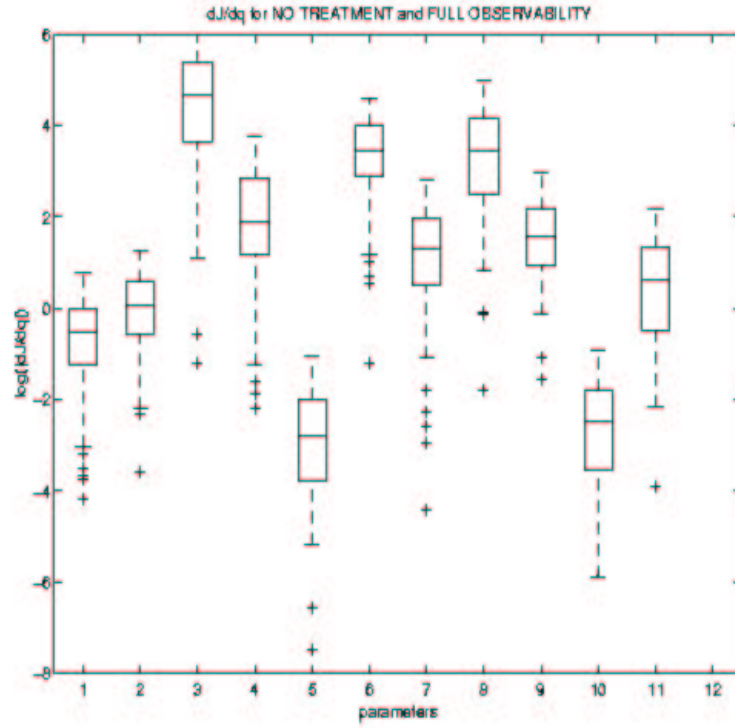

Figure 5.3: Log scale plot of sensitivity of the cost function to our twelve parameters, where the indices along the x-axis correspond to the parameters in the same order found in Section 2.2. Full observability means $C = I$

5.3.4   Sensitivity of Parameters Over Time

One benefit of the sensitivity matrix,

$$\frac{\partial \mathbf{z}}{\partial \mathbf{q}}(t, \mathbf{q_0}),$$

is that it illustrates the time dependence of the sensitivity of each compartment to each parameter. If we choose a particular parameter, we can plot the sensitivity of each compartment with respect to that parameter as a function of time and use this information to decide when measurements of those compartments will be most beneficial. Since many of the laboratory measurements can be costly, it is important to minimize the number of measurements. For our simulated data, we can construct a data measurement schedule and then interpolate at those time values. Using this data we can then compute the sensitivity of the cost function to our parameters.

For example, in the model with no drug treatment, i.e., $u(t) = 0$, we observed that β (infection rate), c (immune effector activation rate), a (natural death rate of infected cells), and b (natural death rate of the immune effector) are most sensitive. In Figure 5, we observe very different behavior of the sensitivity to each of these parameters as functions of time.

Although these plots only represent the sensitivity of the viral compartment, Figure 6 shows that the sensitivity of the other compartments is qualitatively similar.
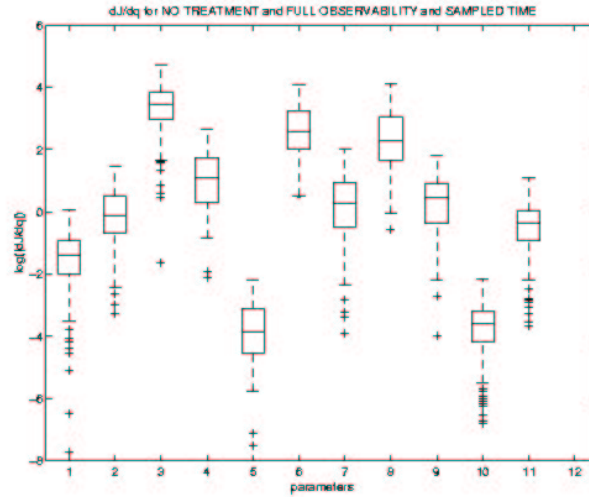

Figure 5.4: Log scale plot of sensitivity of the cost function to our twelve parameters after implementing a measurement scheme based on the sensitivity of β over time. Again, $C = I$.

The system appears to be most sensitive to β initially, but this reduces quickly and then begins to dominate again as time progresses. Hence, we would suggest measuring $\mathbf{z}$ after five days, waiting a month, and then beginning weekly measurements. Using this measurement scheme, Figure 4 shows an increase in the relative sensitivity to β. Similarly, since sensitivity to a remains high throughout time, we would recommend regular measurement throughout the entire observation period (e.g., weekly). The sensitivity to c is high initially, but then decreases rapidly, so we might recommend measuring every third day for six weeks and then discontinuing measurements. For b, we might recommend just the opposite approach. As a result, it is difficult to recommend a measurement schedule for estimating all four of our most sensitive parameters. Perhaps the best approach is simply to measure at regular intervals.

When the structured treatment interruption described in Section 2.2 is introduced, the qualitative behavior of the sensitivity matrix changes. As observed in Figure 7, our previous measurement schemes for a and b may still be appropriate, whereas we need to modify those for β and c. Since the sensitivity to β now begins to increase rapidly after two months, we need to measure more frequently instead of on a weekly basis. Similarly, our measurement scheme for c should now mimic the one for b, since the sensitivities to those parameters are very similar.
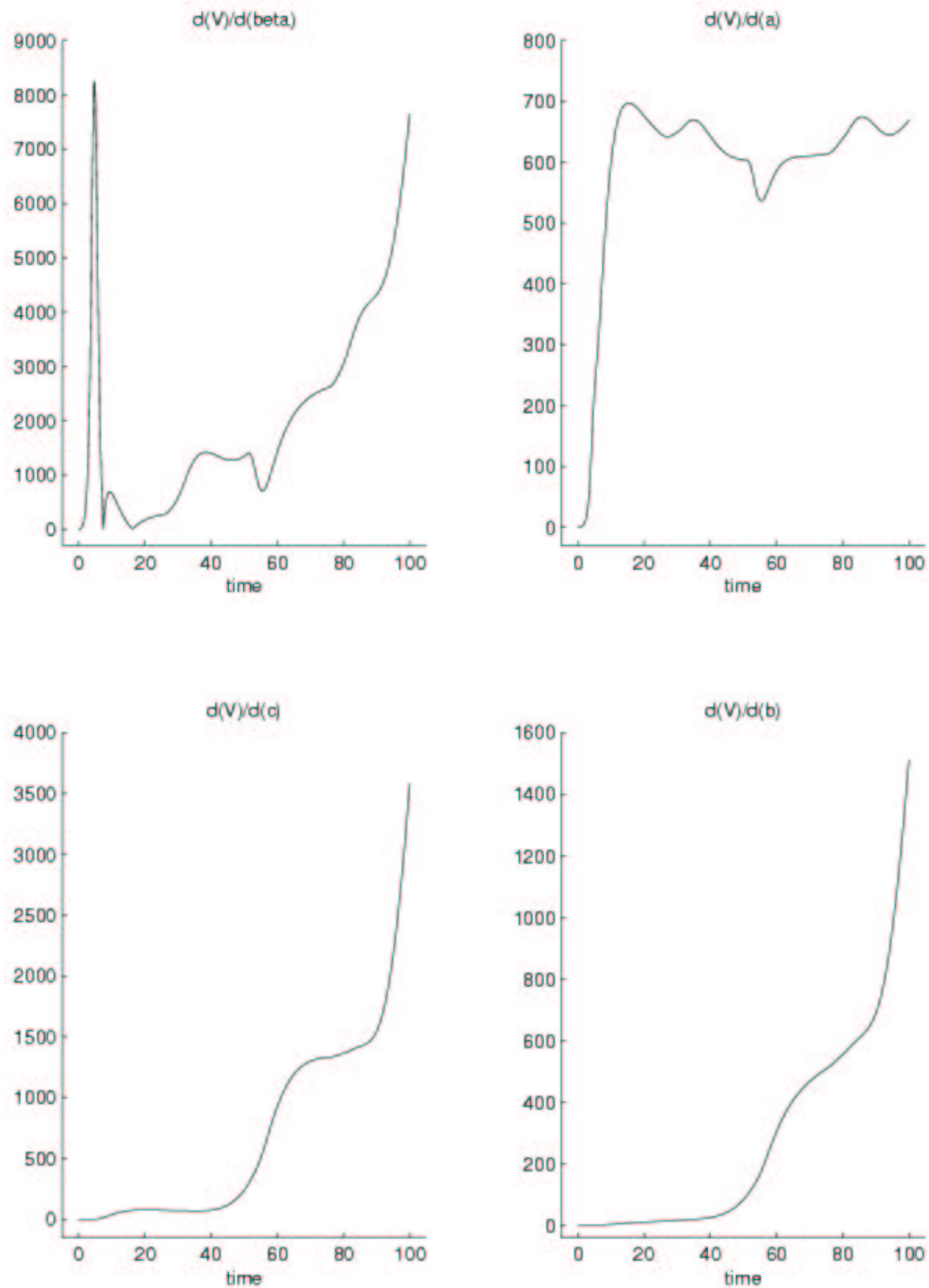
Figure 5.5: Plots of the sensitivity of the viral load V to parameters β, a, c, and b over 100 days of no treatment.
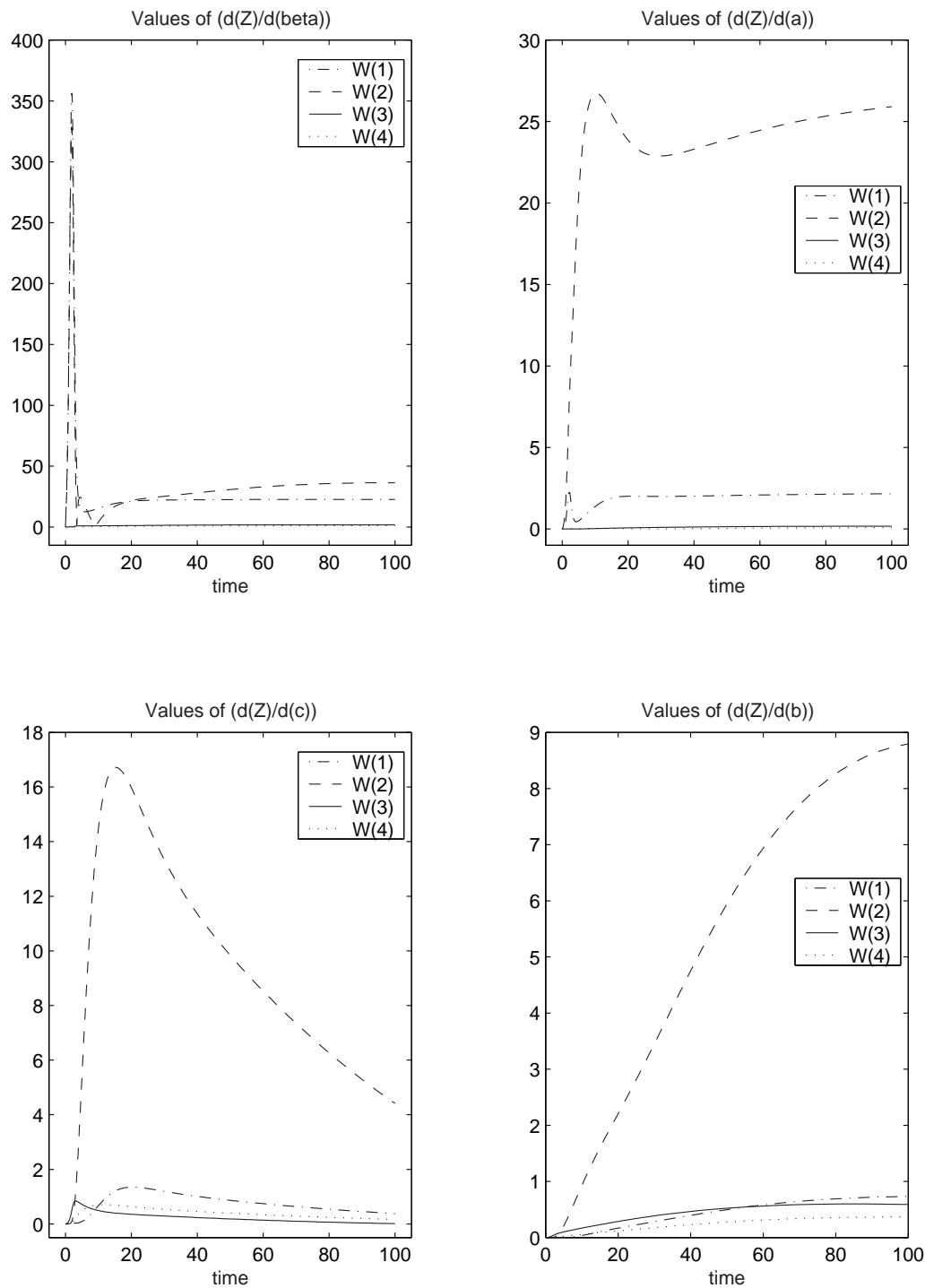
Figure 5.6: Plots of the sensitivity of the first four compartments, where $Z = W(1)$, etc., to the same four parameters as in Figure 5.
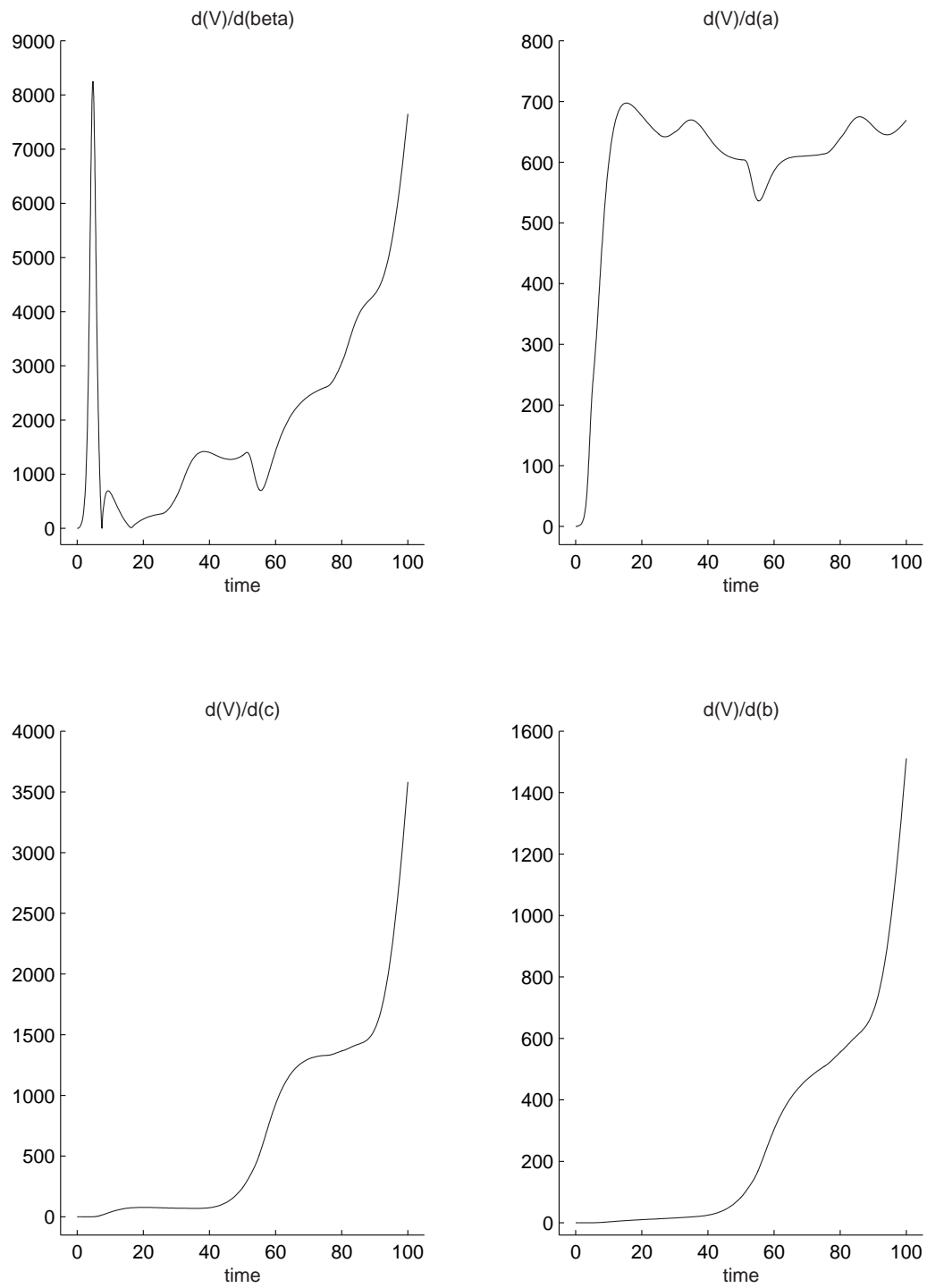
Figure 5.7: Sensitivity of the viral load over 100 days of periodic STI.

5.3.5   Observation Matrices

The cost of data collection varies widely across the five compartments in the model. The viral load V is often the only compartment measured. The uninfected cells X and the infected cells Y, can be measured together with considerably less expense than measuring them separately. The same is true for the immune precursors W and the immune effectors Z. In order to suggest an effective and frugal experimental protocol, it is useful to determine which compartments measurements are essential and whether combining or eliminating compartments compromises the quality of the data. In order to answer these questions, we created a set of observation matrices C_i to represent different combinations of compartments. When our compartmental vector is multiplied by one of these observation matrices, we change the observations made in the parameter estimation problem.

The observations we examined were:

Observations
$[X, Y, W, Z, V]$
$[X, Y, W + Z, V]$
$[X + Y, W + Z, V]$
$[X + Y, W + Z]$
$[X, Y, V]$
$[X + Y, V]$
$[V]$

### 5.3.6   The Effect on $\frac{dJ}{dq}$ from Changing the Observables

Our next step was to incorporate different observation matrices C into the cost function and analyze $\frac{dJ}{d\mathbf{q}}$ for each. To summarize the results, measuring only $[V]$, or $[X + Y, V]$ causes a significant loss in sensitivity with respect to most parameters, whereas the results obtained with $[X + Y, W + Z]$, $[X + Y, W + Z, V]$, and $[X, Y, W + Z, V]$ are strikingly similar to those obtained with the full set of observables $[X, Y, W, Z, V]$. As in Section 3.3 we used a time sampling of once a day for 100 days in each data set, and the results below are for the untreated model. Similar results were obtained in the treated model. Figures 8 and 9 illustrate the changes that occur in the sensitivity of our cost function as we change the observation matrix. The 100 different data sets used to generate the results for any one of the observation matrices were not the same as the data sets used for any of the other observation matrices.

5.4   The Inverse Problem: Estimating the Parameters

5.4.1   Why solve the Inverse Problem?

All of the analysis in this paper is based on the the modified Wodarz-Nowak Model. Now we concern ourselves with another question: *Is our model a good model?* One way to answer this question is to answer another question instead: *Given a data set, does our model describe the data set?* Solving the inverse problem answers the latter question.

Inverse problems arise in a variety of important applications in science and industry. These range from biomedical and geophysical imaging to groundwater flow modeling. In all these applications the goal is to estimate some unknown attributes of interest, given measurements (a data set) which are indirectly related to these attributes. For example, in medical tomography, one wishes to image structures within the body from measurements of X-rays which have passed through the body [9]. For our model, the data set which the immunologist can measure is the vector of observables $\hat{\mathbf{y}} = C\hat{\mathbf{z}}$. For instance, $\hat{\mathbf{y}} = [X + Y, V]$ indicates that the
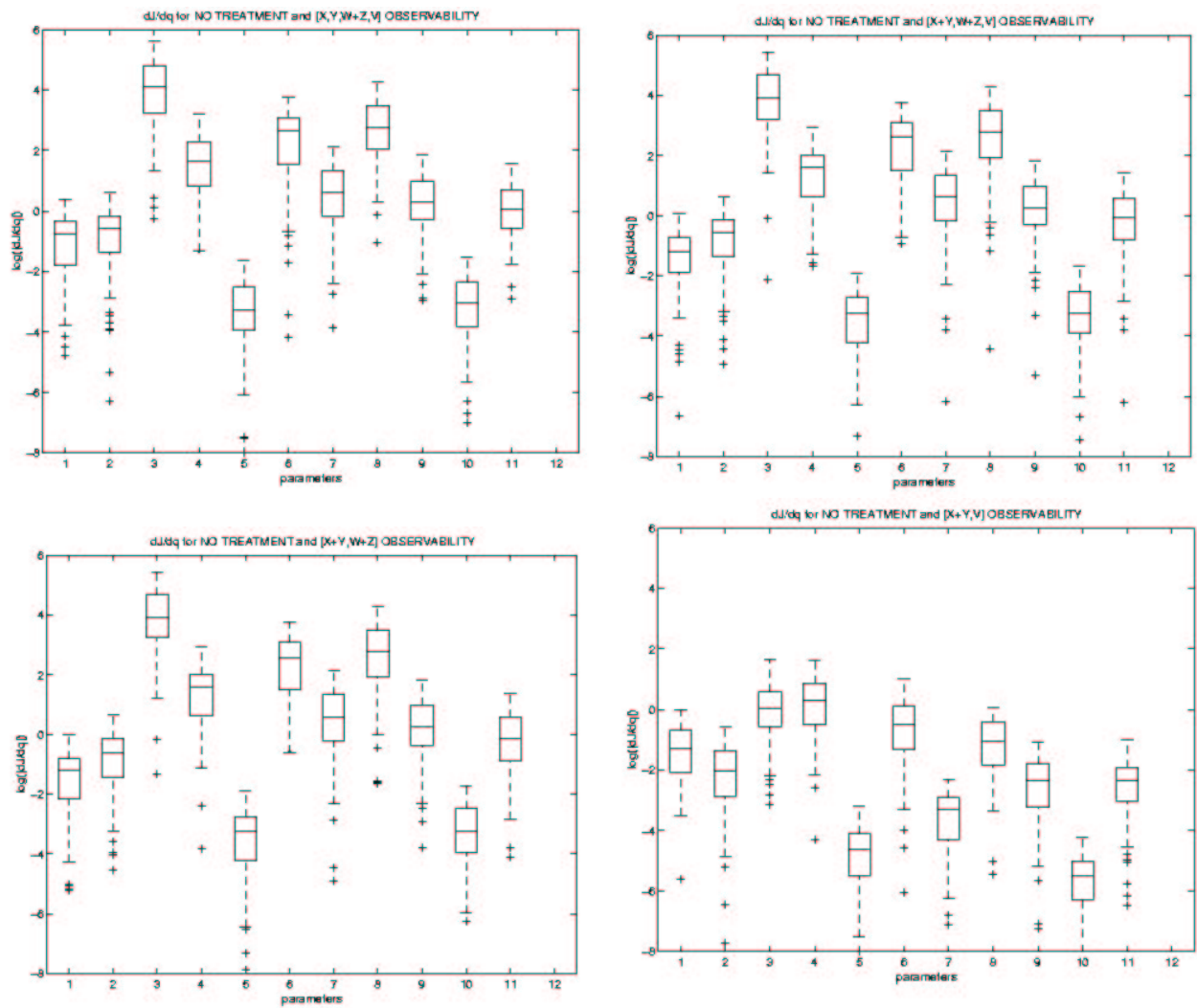
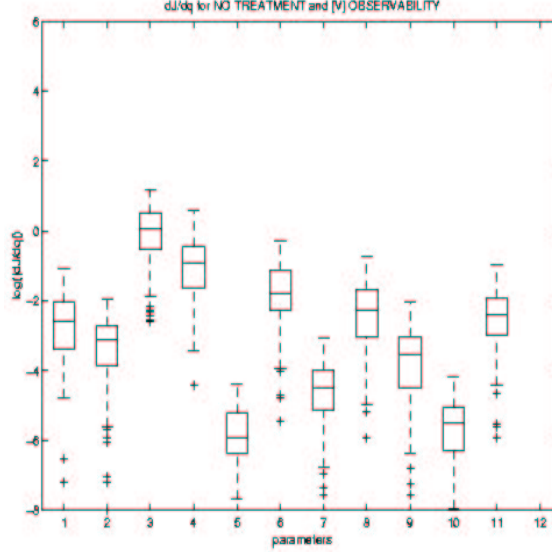Figure 5.8: $\frac{dJ}{d\mathbf{q}}$ for various observation matrices.

Figure 5.9: $\frac{dJ}{d\mathbf{q}}$ when only the viral load is observed.

data available is the total count of X plus Y, the combined total of uninfected T helper cells and infected T helper cells, and V, the number of free virions. The attributes of interest that we wish to estimate given the data $\hat{\mathbf{y}}$ are the components of $\mathbf{q}$.

Solving the inverse problem identifies the parameters $\mathbf{q}^*$ for which the model best describes the given data $\hat{\mathbf{y}}$. That is, we determine $\mathbf{z}(\mathbf{q}^*)$ so that the "distance" between $C\mathbf{z}(\mathbf{q}^*)$ and $\hat{\mathbf{y}}$ is as small as possible. We use the least squares cost function,

$$J(\mathbf{q}) = \frac{\sum_i \left|\log(C * \mathbf{z}(t_i, \mathbf{q})) - \log(C * \hat{\mathbf{z_i}})\right|^2}{\sigma_i^2},$$

to determine this distance. Therefore, solving the inverse problem is equivalent to solving $\mathbf{q}^*$ such that

$$\mathbf{q}^* = \mathrm{argmin}_{\mathbf{q} \in Q_{ad}} J(\mathbf{q}) = \frac{\sum_i \left|\log(C * \mathbf{z}(t_i, \mathbf{q})) - \log(C * \hat{\mathbf{z_i}})\right|^2}{\sigma_i^2}$$

where Q_{ad} is called Q-admissible, the space of valid values for $\mathbf{q}$.

Given a data set, does our model describe the data set? The answer is yes if $J(\mathbf{q}^*)$ is "small".

5.4.2   Implementation

Simulating Data

To formulate the inverse problem requires data. Since we did not have access to real data, we simulated data by

$$\log \hat{\mathbf{z_i}} = \log \mathbf{z_i} + \sigma \epsilon_i,$$

where $\epsilon_i = \epsilon(t_i) \sim N(0,1)$ and we assumed the vector of measurement errors were $\sigma^2 = [.01 .01 .01 .01 .25] \cdot \lambda$, for $\lambda \geq 1$. That is, σ^2 is the error incurred when a clinician actually measures each compartment. Therefore, when we generate data we are assuming that X, Y, W and Z are each measured with 1% error from the true measurement and V is measured with 25% error from the true measurement.

Since we are assuming that X, Y, W, Z, V are mutually independent, then for example we can assume that the measurement error for measuring X and Y together is the sum of the measurement errors of measuring X and then Y individually. Hence, the measurement error for $C\hat{\mathbf{z}}_{\mathbf{i}}=$[X + Y] is $\sigma_X^2 + \sigma_Y^2$.

Optimization Methods

To find $\mathbf{q}^*$, we used the Nelder Mead simplex method (MATLAB's *fminsearch*). We tried other optimization methods, including Steepest Descent, Newton CG and BFGS methods, but Nelder Mead outperformed these for our data. Nelder Mead has the further advantage that the gradient $\nabla_q J = \partial J / \partial \mathbf{q}$ need not be calculated; the method only requires evaluations of the cost function $J(\mathbf{q})$.

Using the Sensitivity Analysis

If it becomes difficult to find $\mathbf{q}^*$ over all the parameters, then we can concern ourselves with optimizing J just over the parameters to which the model is most sensitive. The five most sensitive parameters for the model with treatment in order of sensitivity, identified by the sensitivity analysis that we performed, are

$$
\begin{aligned}
\beta &= \text{proliferation rate of Infected T helper cells,} \\
c &= \text{proliferation rate of Immune Precursors Cytotoxic T Lymphocyte,} \\
b &= \text{natural death rate of Immune Precursors Cytotoxic T Lymphocyte,} \\
a &= \text{natural death rate of Infected T helper cells, and} \\
f &= \text{drug efficacy.}
\end{aligned}
$$

Further Assumptions

We solved the inverse problem for thousands of different synthetic data sets $\hat{\mathbf{z}}$, where the error σ^2 was generated for λ=1, 10, 100, 1000, and 10000; and $\mathbf{z} = \mathbf{z}(t_i, \mathbf{q_{true}})$, with $\mathbf{q_{true}} =$[1, .1, .02, .2, 1 ,.027, .5, .001, .1, 25, 1, .75]. Note that each $J(\mathbf{q})$ evaluation requires a forward solution of the ODE, as in Section 3.2. For each of these, we assumed that $z_{init} = [10, .3, .008, .001, 7, .5]$.

Furthermore, we let C be the identity matrix (so we are assuming *full observability*, that each compartment of $\mathbf{z}$ can be measured), that $t_i = 1, 2, 3, 4, ..., 100$ (measurements for each compartment are taken each day over a 100 days), and that the periodic treatment $u(t)$ is being applied.

5.4.3 Results

Two general approaches were used. First, for $\mathbf{q_{init}} = \mathbf{q_{gen}}$, synthetic data was generated for λ=1, 10, 100, 1000, and 10000. When the parameters are independent, this approach allows us to estimate a probability density for each of the components of $\mathbf{q}$.

Secondly, we solved the inverse problem for many different values of $\mathbf{q_{init}} = \mathbf{q_{true}} + \mathbf{q_{true}} \cdot \eta\delta$, where $\delta \sim N(0, 1)$. As η increases, $\mathbf{q_{init}}$ is perturbed further from $\mathbf{q_{true}}$. Since $\mathbf{q}^* \approx \mathbf{q_{true}}$, this methodology should enable us to estimate a confidence neighborhood about $\mathbf{q_{true}}$ so that for any $\mathbf{q_{init}}$ in this neighborhood we can make a confidence statement about how well our inverse problem algorithm can find $\mathbf{q}^*$ adequately close to $\mathbf{q_{true}}$.

Estimating Probability Densities

As mentioned before, we simulated data by

$$
\log \hat{\mathbf{z}}_{\mathbf{i}} = \log \mathbf{z}_{\mathbf{i}} + \sigma \cdot \epsilon,
$$

where

$$
\epsilon \sim N(0, 1),
$$

and we assumed the vector of measurement errors was σ^2=[.01, .01, .01, .01, .25]$\cdot\lambda$, for $\lambda \geq 1$ where lambda is a scalar to amplify the noise in the data. Simulations were run for lambda=1, 10, 100, 1000 and 10000.

Keeping $\mathbf{q_{init}} = \mathbf{q_{true}}$ fixed, we varied the amount of noise in the data by generating 100 different synthetic data sets for each of the values λ=1, 10, 100, 1000 and 10000. When the parameters are independent, this approach allowed us to construct a marginal probability density for each of the components of $\mathbf{q}$.

Figure 10(a) shows the results of our algorithm for the five most sensitive parameters: β, c, b, a, and f when $\lambda = 10$. Figure 10(b) shows a probability density for β when $\lambda = 10$.
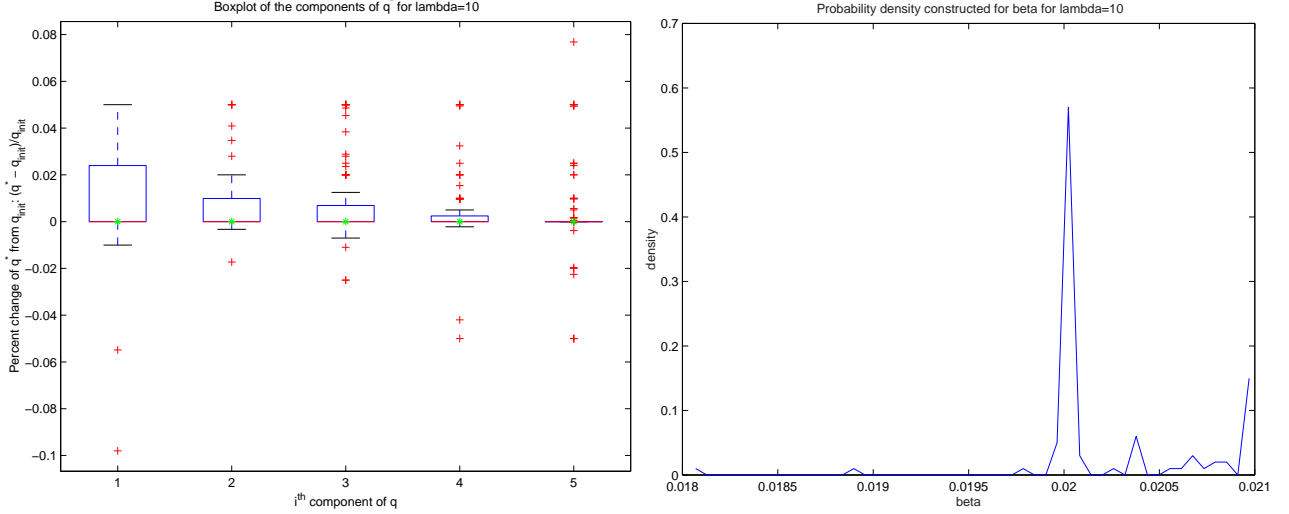

Figure 5.10: (a) Boxplot of $\mathbf{q}$=[β c b a f] vs the percent variation of each these parameters ($\mathbf{q}^*$) from $\mathbf{q_{true}}$, $\frac{\mathbf{q}^* - \mathbf{q_{true}}}{\mathbf{q_{true}}}$, over 100 inverse problem solves for λ =10. (b) The probability density of beta that we constructed using the results from (a).

Trying to Find a Confidence Neighborhood

First, we attempted to find $\mathbf{q}^*$ over all twelve parameters. For η =.01, .05, and .1, we saw that the $\mathbf{q}^*$ procured from our algorithm was not very far from $\mathbf{q_{init}}$ (see Figure 11). For values of $\eta \geq .2$ (for large perturbations of $\mathbf{q_{init}}$ from $\mathbf{q_{true}}$, the Nelder Mead algorithm was unable to solve the system at all. Hence, we turned to the results of our sensitivity analysis to make the optimization problem simpler.

As mentioned earlier, when it becomes difficult to find $\mathbf{q}^*$ over all the parameters, then we can concern ourselves with optimizing J just over the parameters to which the model is most sensitive. Therefore, we set $\mathbf{q_{true}}$ =[β c b a f], the five most sensitive parameters.

The only benefit to this approach was that we were able to solve the system for $\eta \leq .5$. Unfortunately, the $\mathbf{q}^*$ procured from our algorithm still was not very far from $\mathbf{q_{init}}$, as seen in Figure 12. Hence a new optimization scheme is recommended which is not so dependent on $\mathbf{q_{init}}$.

5.5   Conclusion

The results of our investigations provide some guidance for future study, including design of experiments aimed to investigate the efficacy of STIs, the validity of the modified Wodarz-Nowak model for HIV infection dynamics, and estimates for the parameters in the model.

Our first set of results from the sensitivity analysis concerns the parameters in the model. The sensitivity analysis determined that the parameters $\beta, a, p,$ and c were still the most sensitive and that with treatment,
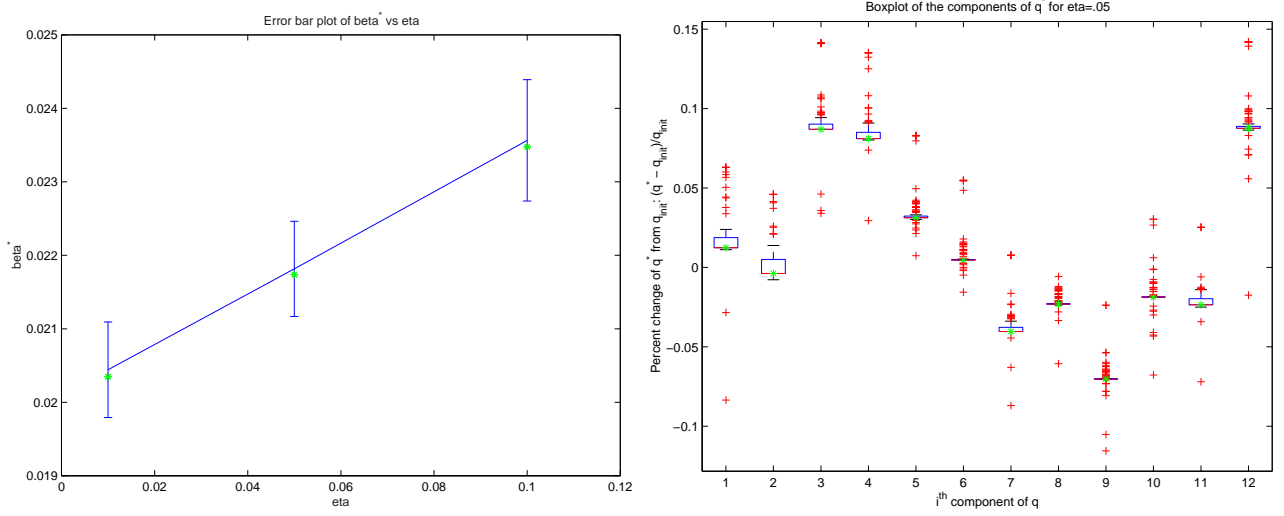
Figure 5.11: (a) When optimizing over all the parameters, this is the error plot of optimal β, β^*, vs η, the perturbation applied to β_{true} to generate β_{init}. The value of β_{init} is indicated by an '*'. For the same $\mathbf{q_{init}}$, the inverse problem was solved 100 times, with a different synthetic data set for each solve, for η: $\eta =.01$, .05, and .1. Since $\mathbf{q_{init}} = \mathbf{q_{true}} + \mathbf{q_{true}} \cdot \eta N(0,1)$ then, for each η, $\beta_{init} = .02 + .02 \cdot \eta N(0,1)$. Error bars indicate 2 standard deviations about the mean for the 100 different inverse problem solves. β^* is directly related to the perturbation of β_{init}. In fact, for for $\eta \geq .05$, $\beta^* > .15\beta_{true}$. (b) When optimizing over all parameters, this is the boxplot of the components of $\mathbf{q}$ vs the percent variation of each component of $\mathbf{q}^*$ from $\mathbf{q_{true}}$, $\frac{q^* - q_{true}}{q_{true}}$, over 100 inverse problem solves for $\eta =.05$. $\beta = \mathbf{q}[3]$. These plots indicate that we ought to try constraining our optimization to the parameters that affect the model the most.
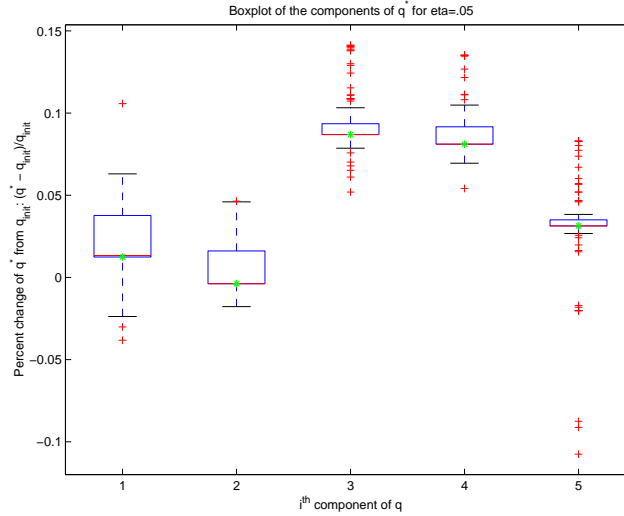

Figure 5.12: When optimizing over the 5 parameters which affect the model the most, $\mathbf{q}=[\beta\ c\ b\ a\ f]$, this is the boxplot of the components of $\mathbf{q}$ vs the percent variation of each component of $\mathbf{q}^*$ from $\mathbf{q_{true}}$, $\frac{q^* - q_{true}}{q_{true}}$, over 100 inverse problem solved when $\eta =.05$. These plots indicate that even when constraining our optimization to the parameters that affect the model the most, $\mathbf{q}^*$ is still far from $\mathbf{q_{true}}$. Hence a new optimization scheme is recommended which is not so dependent on $\mathbf{q_{init}}$.

the drug efficacy f becomes the fifth most sensitive parameter. These parameters play significant roles in the dynamics of the model.

Our second set of results from the sensitivity analysis suggests times to collect data about the parameters. Without STI, the system is most sensitive to β initially, which reduces quickly and then begins to dominate again as time progresses. We suggest measuring **z** after five days, waiting a month, and then beginning weekly measurements. Since sensitivity to a remains high throughout time, we would recommend regular measurement throughout the entire observation period (e.g., weekly). The sensitivity to c is high initially, but then decreases rapidly, so we might recommend measuring every third day for six weeks and then discontinuing measurements. For b, we recommend the opposite approach. Because the results for each parameter suggest a different measurement schedule, we suggest that the best approach may be to measure at regular intervals. With STI, the sensitivity to β now begins to increase rapidly after two months. Consequently, with the introduction of STI, we suggest more frequent measurement.

Our third set of results from the sensitivity analysis indicates which combinations of compartments play a significant role in the dynamics of the model. Measuring only $[V]$, or $[X+Y,V]$ causes a significant loss in sensitivity with respect to most parameters, whereas the results obtained with $[X+Y, W+Z]$, $[X+Y, W+Z, V]$, and $[X, Y, W+Z, V]$ are strikingly similar to those obtained with the full set of observables $[X, Y, W, Z, V]$. This is a very useful result, since combining measurement of X with Y and W with Z leads to a large reduction in cost of data collection without sacrificing the quality of the information collected.

In our work with the inverse problem, we have discovered the probability distributions for optimal β, c, b, a, and f, the parameters to which the model is most sensitive, given the synthetic data sets that we constructed. Although our approach was not able to achieve a solution for the inverse problem over all twelve parameters, limiting the optimization to the most sensitive parameters results in some increase in the ability of the optmizer to converge to the optimal parameter set.

Some questions for future consideration concern the details of the experimental protocol and future attempts to solve the inverse problem. One issue of particular concern is how to time the STIs given that a "day" in our model may not correspond to real time. Once data have been collected, the inverse problem can be reexamined to find better estimates for parameters in the model.

5.6   Acknowledgements

Bibliography

[1] Lisziewicz J, Rosenberg E, Liebermann J et al., *Control of HIV despite the discontinuation of antiretroviral therapy*, New England Journal of Medicine, 340:1683-4, 1999.

[2] Rosenberg, E. S., M. Altfeld, S. H. Poon et al., Nature, 407:523-526, 2000.

[3] Wodarz, D., and M.A. Nowak, *Specific therapy regimes could lead to long-term immunological control of HIV*, Proc Natl Acad Sci USA 96, 14464-9, 1999.

[4] Coddington, Earl A., and Levinson, Norman, *Theory of Ordinary Differential Equations*, McGraw-Hill, New York, 1955.

[5] Bonhoeffer, S., M. Rembiszewski, G. M. Ortiz, and D. F. Nixon, *Risks and benefits of structured antiretroviral drug therapy interruptions in HIV-1 infection*, AIDS 14:2313-2322, 2000.

[6] Davey RT. N. Bhat, C. Yoder et.al. 1999, Proc. Natl. Acad. Sci, 96:15109-14.

[7] Garcia, F., M. Plana, C. Vidal et al., AIDS, 13:F79-F86.

[8] Ortiz G, Nixon D, Trkola A et al., *HIV-1-specific immune responses in subjects who temporarily contain antiretroviral therapy*, J. Clin. Invest., 104:R13-R18, 1999.

[9] C.R. Vogel, *Computational Methods for Inverse Problems*, preliminary manuscript, to be published by SIAM, available on the web at www.math.montana.edu/∼vogel/Book

Report 6

Ring Structure Against Rolling Circular Drum

Nathan Gibson [1], Jason Kurtz [2], Ahmed Naga [3], Zoi Rapti [4], Yoon Song [5], Yan Yu [6],
Stanislav Žabić [7]

Problem Presenters:
Damon Christenbury & Yue Zhang
Michelin North America

Faculty Consultant:
Hien T. Tran, with the assistance of Julie Raye

Abstract

This problem, motivated by Michelin, arises in the design of a run-flat, or PAX, tire system. A PAX tire system consists of a larger than normal radius aluminum wheel, a low-profile tire, and a special rubber support ring attached to the wheel inside the tire. The goal of the support ring is to provide a safe driving transition in the case of a flat tire. After the air has deflated from the tire, the support ring carries the entire load of the car.

Here we discuss ways to optimize the design of the support ring. This work represents a "first step" in the process of solving the problem. In particular we focus on minimizing the interior temperature over different feasible shapes for the design of the ring, subject to mass and stability constraints. This involves nonlinear optimization and the solution of a 2D heat equation. In addition to addressing these initial aspects, we point out which directions might yield the most improvement in future undertakings.

6.1 Introduction and motivation

A run-flat, or PAX, tire system is a new type of tire and wheel capable of running safely even when the tire is unexpectedly deflated, say by a nail on the road. When the tire is deflated, the weight of the car is supported

---

[1]North Carolina State University
[2]Clarkson University
[3]Wayne State University
[4]University of Massachusetts at Amherst
[5]University of Maryland - Baltimore County
[6]State University of New York at Stony Brook
[7]Louisiana State University

by a stiff, one-piece rubber ring structure mounted on the wheel inside the tire. This interior ring must be capable of supporting the weight of a car and passengers at road speeds long enough to reach a destination where the tire can be replaced. The design of this ring is the subject of the current report.

There are several obvious criteria for an acceptable PAX tire system. The first of these is that the vehicle must be able to run a suitable distance, for example 120 miles, with a completely deflated tire. Thus, the ring structure must be capable of both supporting the cyclic loading to which a tire is subjected and evenly distributing the heat generated by that loading. Under high temperatures the material properties of the rubber can change and therefore decrease the structural stiffness. Experiments conducted on initial ring designs by Michelin have shown that the heat generated is indeed a significant problem. In addition, we must constrain the weight of the ring structure since it serves no purpose under normal operating conditions, i.e., when the tire is inflated. Ideally, a set of four PAX tires should weigh the same as, or less than, a conventional set of wheels and tires plus one spare tire. Some extra weight could possibly be justified by the added safety of a PAX tire system. Lastly, the thickness of the ring, must obviously be small enough to fit inside the tire, but not so small as to affect the drivability of the vehicle when the tire is flat. In short, our design goals are minimize temperature and maximize mechanical stiffness, subject to constrained mass and dimensions.

A complete mathematical approach to the design of a PAX tire system must take all of these effects into consideration. However, to obtain a model simple enough to be used in an optimization routine, we have taken the approach of separating the mechanical properties of the design from the thermal properties. In particular, the problem we attempt to solve in this paper has the objective of minimize temperature, subject to constrained stiffness, mass and dimensions.

In order to most effectively determine the best overall shape for the ring element, as well as most efficiently utilize the time available to our team during the workshop, we decided to divide the problem into two essentially independent, but complementary parts. One approach is what we refer to as "Topology Optimization". By this we mean that initially we assume nothing about the shape of the structure, and through an optimization routine we attempt to discover a general, optimal design. This can be thought of as a macroscopic or global view of the optimization problem.

The second approach is to assume a certain general shape (ideally determined by the previous method) and define parameters to specify its exact geometry. The objective function is then optimized over this relatively small set of parameters. We refer to this method as "Geometric Optimization". It can be thought of as a fine tuning of the first method. When used together these two methods can determine a specific and yet globally optimal design for the ring structure in the PAX tire system.

6.2   Physical Background

To determine the design of the ring, we choose the shape of one section, or element, of the structure, and then repeat this shape around the rim of the wheel thus forming a ring. Although the ring is circular, and a wedge from the ring would have some curvature, we assume the element is flat and use cartesian coordinates. The radial direction of the tire is referred to as the depth of the element, and we fix this thickness of the ring throughout the rest of the paper (based on the constraint described above for the height of the tire when deflated).

As soon as the tire is deflated, the PAX system is in operation. The support ring undergoes cycling loading, i.e. there is a pressure applied to it each time it hits the ground. Due to this cycling loading there are mechanical strains and deformations. This contracting and expanding of the rubber generates heat internally. In our model, we approximate the heat generated by a uniform heat source

$$\dot{Q} = f_{req} * \sigma * \varepsilon * sin\delta, \tag{6.2.1}$$

(given in watts per cubic meter) where f_{req} is the frequency of the cycling loading, σ is the mechanical stress, ε is the mechanical strain, δ is the phase angle [7]. For the purposes of our numerical calculations, $\dot{Q}$ is given by experimental data from Michelin with only temperature dependence.
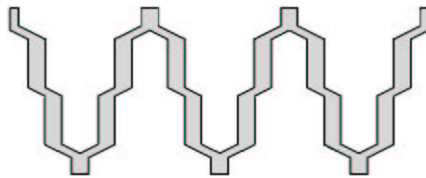
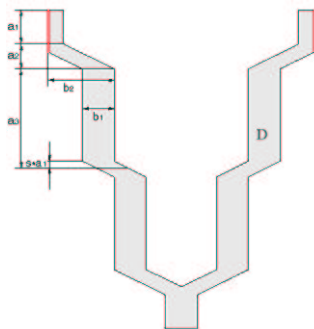Figure 6.1: Skematic of current V-shape design at Michelin

Figure 6.2: Geometric characterization of V-shape design

For our physical model, we assume that the heat transfers only in the plane of the surface of the element and that there is no heat transfer along the depth of the element. All air and heat dynamics outside the support ring are assumed constant and are incorporated into appropriate boundary conditions for the element. This reduces the problem of solving for the temperature to a two dimensional heat transfer problem with Newton cooling on the open boundaries and insulation on periodic boundaries, which is described by a two dimensional parabolic PDE with mixed Neuman boundary conditions.

6.3 Geometry Optimization

A current prototype for the support ring designed by Michelin has a periodically repeated V-shape as shown in Figure 6.1. The periodic zig-zag pattern, sandwiched between two thin rubber sheets, becomes the support ring (To picture this, imagine the support ring in action, supporting the weight of the car - adjacent to the road is the tire casing, the outer rubber sheet of the support ring, the zig-zag structure, the inner rubber sheet, and finally the wheel.). As a starting point for the geometry optimization, we assume that the current V-shape design at Michelin (see Figures 6.1 and 6.2) is inherently good at bearing load without buckling. Thus our objective is to specify the exact dimensions of a V-shape that simply distributes heat most effectively. To do this we introduce 6 geometrical parameters that characterize the shape and dimensions, as illustrated in Figure 6.2. The optimal V-shape obtained by our model is represented by an optimal set of values for these parameters subject to the previous constraints and conditions.

6.3.1 Mathematical Model

We wish to minimize the maximum temperature over the area of the element at the final time, varying the dimensions of the V-shape. We formulate our problem as a non-linear optimization problem with cost function
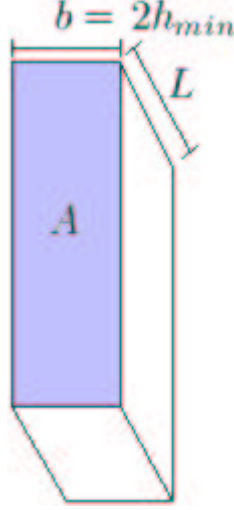
Figure 6.3: Approximation of V-shape design for calculating critical load

$\max_{x,y \in D} T(t_f, x, y)$, where D is the domain of the V-shape, T is the temperature, and t_f is the final time.

Again, we assume that the heat generated by a cyclic load can be represented by a uniform heat source $\dot{Q}$. Then the planar heat transfer within the V-shape is governed by the 2-D heat equation,

$$\rho c_p \frac{\partial T}{\partial t} = k\left(\frac{\partial^2 T}{\partial x^2} + \frac{\partial^2 T}{\partial y^2}\right) + \dot{Q} \tag{6.3.2}$$

We assume the initial distribution of heat is constant and equal to the ambient temperature, T_∞. Heat transfer through the edges of the V-shape is specified by two different boundary conditions. On the boundaries which are actually in contact with the next V-shape (shown in red in Figure 6.2 and collectively referred to as Γ_{per}, as in periodic boundary conditions) we assume that no heat is transferred, thus

$$\frac{\partial T}{\partial x} n_1 + \frac{\partial T}{\partial y} n_2 = 0, \text{ on } \Gamma_{per}$$

where $\vec{n} = (n_1, n_2)$ is the outward unit normal to the boundary. On boundaries in contact with air (shown in black in Figure 6.2 and denoted by Γ_{air}), we assume that there is sufficient turbulent mixing for the air temperature to be a constant. Thus we have Newton's law of cooling,

$$\frac{\partial T}{\partial x} n_1 + \frac{\partial T}{\partial y} n_2 = -h(T - T_\infty), \text{ on } \Gamma_{air}.$$

With this model for heat generation and diffusion we can compute the temperature distribution $T(t, x, y)$ within the V at some final time t_f.

We must also be able to compute the load that a given V-shape can safely support without buckling. This is rather complicated and requires approximation. We approximate the V-shape by a rectangle of the same contact area as the V-Shape and a width that is twice the minimum width of the V's arms ($b = 2h_{min}$), as shown in Figure 6.3. This is roughly like collapsing the arms of the V inward against each other and computing the buckling load for the resulting solid rectangular block. For such a shape (with rectangular cross-section) we have the following formula for F_{crit}:

$$F_{crit} = \frac{4\pi^2 E(T) A b^2}{12L^2}$$

This represents a gross underestimation of the actual V-shape's buckling load. Our model addresses the third design goal (maximize mechanical stiffness) by requiring that $F_{crit} \geq F_{load} = \text{Mass}_{car}g$. In our computation we take A to be the area of the crossection of the V-shape.

Throughout, all material properties are taken to be independent of temperature for simplicity. The only exception is Young's modulus $E(T)$, which is taken from the following look-up table based on experimental data:

Temperature T	Young's modulus $E(T)$
0 C°	4.6
20 C°	4.05
40 C°	3.8
60 C°	3.7
80 C°	3.6
100 C°	3.6

6.3.2 Optimization Problem

Our objective is to minimize the maximum temperature over the V-shape at the final time, by varying the geometry parameters and keeping the total width and total height of the element fixed. Another requirement is to make sure the V-shape is able to support a prescribed load. We formulate our problem as the following non-linear optimization problem.

$$\min_{a_1, a_2, a_3, b_1, b_2, s, L} \quad \max_{x, y \in D} \quad T(t_{max}, x, y)$$

$$
\begin{aligned}
2b_2 + b_1 &= \text{width,} \\
a_1 + a_2 + a_2 &= \text{height,} \\
F_{crit} &\geq F_{load}, \\
\text{Volume} &\leq \text{Initial volume,} \\
b_2 - \frac{b_1}{2} &\geq 0, \\
a_1, a_2, a_3, b_1, b_2 &\geq 0, \\
0 \leq s &\leq 100, \\
0 \leq L &\leq L_{max}.
\end{aligned}
$$

Here, the parameters $a_1, a_2, a_3, b_1, b_2, s$ and L represent dimensions in the V-shape as illustrated in Image 2, with L the radial thickness of the element. The domain defined by a_1, a_2, a_3, b_1, b_2 and s is denoted by D. The temperature distribution at time t_{max} is denoted by $T(t_{max}, x, y)$. The first two constraints fix the planar width and height of the V-shape so that two different V-shapes can be considered comparable since one is not wider or narrower than the other. The third constraint expresses our requirement that the prescribed load be less than the buckling load of a given V-shape. The fourth constraint adresses our weight constraint since the thickness and density of the ring are fixed. The rest of the constraints are required to keep the dimensions of the V-shape from *collapsing* during the optimization process.

6.3.3 Computation and Numerical Solution

The above optimization problem was implemented in MATLAB using the PDE Toolbox to solve the heat equation (6.3.2). The initial program optimizes only the V-Shape but can be easily modified to support other shapes. The input parameters are the initial dimensions of the element, material density ρ, specific heat c_p, thermal conductivity k, heat rate per unit volume $\dot{Q}$, convection coefficient h, air temperature T_∞, prescribed load F_{load}, initial rubber temperature T_0, final time t_f, and the discrete time-step size. The body of the program is a non-linear optimization routine, which calls a heat equation solver in each step. By modifying

the code of our program, one can change the precision of the algorithm, maximum number of iterations, and all lower and upper boundaries for constraints on variables. Of course, one has to make sure that the initial data falls within these constraints. The outputs are the minimal value of the objective function, that is the attained minimum of the overall maximum temperature on the element at the final time, the optimal dimensions, and two images: one of the initial shape with heat distribution, and the other of the optimal shape with heat distribution as well.

We have experimentally determined an interval of appropriate values for t_f. This is because solving the heat equation over a long time can become computationally expensive, especially since it must be done for each objective function evaluation. For our computations, we chose t_f as low as 500 seconds. This interval was chosen because the temperature distribution changes little after 800 seconds (the overall temperature, of course is still rising), so that computing the solution for longer times is unnecessary. If one solution is optimal after the distribution stabilizes, it should remain optimal since the heat source is uniform. However, in order to determine the actual maximum temperature at a specific final time, one should prescribe the optimal value of the parameters as initial conditions and change t_f to the desired amount.

6.3.4 Results

We tested our program with the following parameter values as input:

Input 1							
GeometryParms =	a_1	a_2	a_3	b_1	b_2	s	L	"V-shape" area
	37	9.01	12.49	9.88	15.56	7.07	40	2000
PhysicalParms =	ρ	c_p	k	$\dot{Q}$	h	T_{Air}	T_{Ext}	load
	1200	1940	0.23	5.85530	11	393.15	393.15	350
SolverParms =	T_0	t_{max}	timestep					
	298.15	500	10					

Lower bound on L was 20. See Figure 6.4.

Input 2							
GeometryParms =	a_1	a_2	a_3	b_1	b_2	s	L	"V-shape" area
	37	9.01	12.49	9.88	15.56	7.07	40	2000
PhysicalParms =	ρ	c_p	k	$\dot{Q}$	h	T_{Air}	T_{Ext}	load
	1200	1940	0.23	5.85530	11	393.15	393.15	350
SolverParms =	T_0	t_{max}	timestep					
	298.15	500	10					

Lower bound on L was 40. See Figure 6.5.

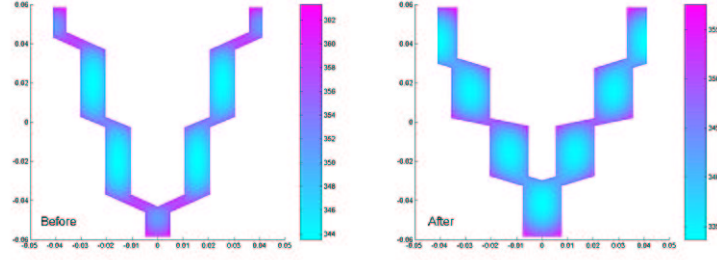| Input 3							
GeometryParms =	a_1	a_2	a_3	b_1	b_2	s	L	"V-shape" area
	37	9.01	12.49	9.88	15.56	20	30	2000
PhysicalParms =	ρ	c_p	k	$\dot{Q}$	h	T_{Air}	T_{Ext}	load
	1200	1940	0.23	5.85530	11	393.15	393.15	350
SolverParms =	T_0	t_{max}	timestep					
	298.15	500	10					

Lower bound on L was 20. See Figure 6.6.

Figure 6.4: Computed solution with parameters Input 1
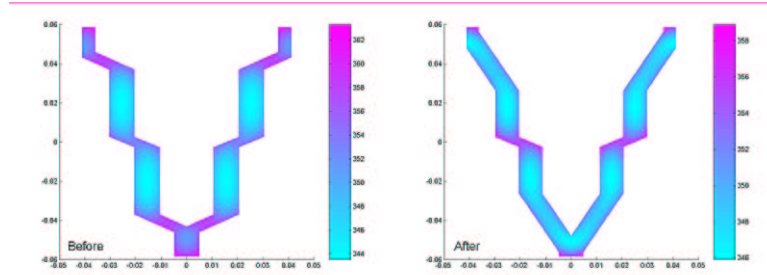
Figure 6.5: Computed solution with parameters Input 2

Input 4								
GeometryParms =	a_1	a_2	a_3	b_1	b_2	s	L	"V-shape" area
	37	9.01	12.49	9.88	15.56	25	40	2000
PhysicalParms =	ρ	c_p	k	$\dot{Q}$	h	T_{Air}	T_{Ext}	load
	1200	1940	0.23	5.85530	11	393.15	393.15	350
SolverParms =	T_0	t_{max}	timestep					
	298.15	500	10					

Lower bound on L was 30. See Figure 6.7.

Given these inputs, our program produces the following "optimal" values.

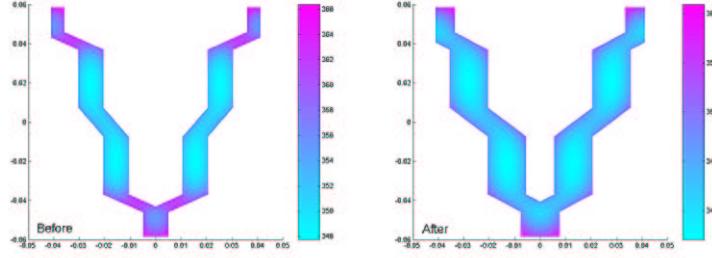| Final Geometry Parameter Values								
	a_1	a_2	a_3	b_1	b_2	s	L	T_{max}
Results 1	27.6192	5.0702	25.8107	15.1373	12.9313	7.0728	30.0000	357.5409
Results 2	26.2536	30.24645	2.0000	9.2065	15.8968	9.4405	40.0000	358.8926
Results 3	36.8345	9.1083	12.5572	15.0042	12.9979	20.0007	20.0000	360.9081
Results 4	31.9007	10.3611	16.2382	13.8389	13.5805	24.9999	30.0000	358.4912

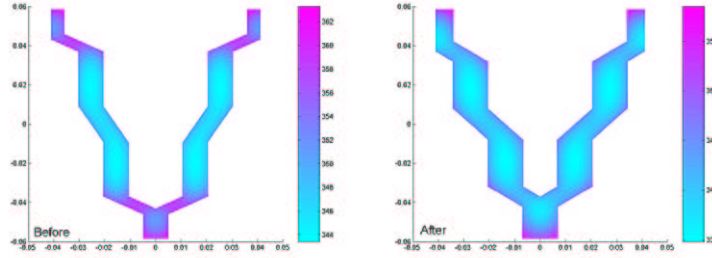Figure 6.6: Computed solution with parameters Input 3

Figure 6.7: Computed solution with parameters Input 4

6.4 Topology Optimization

It should be said first that the topology optimization method is very ambitious and currently not too well understood. Whereas our implementation of the geometry optimization method has only 6 variables to optimize over, the topology optimization can require more than 200 to get a usable result. With this many unknowns, obviously the sensitivity of parameters is an issue. Considering this and other technical difficulties with the topology optimization method, what we present here is a framework for its future implementation.

This work is based on a paper by Ole Sigmund [9] in which a MATLAB code is given for solving a topology optimization problem involving only mechanical stresses (downloadable from the web at http://www.topopt.dtu.dk). Here we first clarify exactly what is meant by topology optimization. Then we develop a model for the temperature of the element, as well as a solution method, based on Sigmund's, which can be used within in the topology optimization method. Lastly we discuss some enhancements to Sigmund's optimization routine, as well as explore some limitations of the entire code through sensitivity analysis.

6.4.1 Problem description

The basic idea of topology optimization is that one starts with a domain that is discretized into smaller elements (rectangles in 2D). Each rectangle is partially filled with material, in this case rubber. We iterate from some initial distribution and hopefully converge to some final distribution where each element is either completely filled or completely empty. We assume that the elements are initially filled uniformly, the total amount of mass in the domain is always constant, and the physical properties of the material in each element are some fraction of what they would be if the element were completely filled. This last assumption is what is known as the "power-law approach" or SIMP (see [9] and references therein). The idea of a uniformly, yet partially filled element is almost like starting with a solid chunk of rubber and carving away pieces until the objective function is maximized, except that we must always have the same amount of mass. It more closely resembles having a porous, malable material which can be squeezed to fit into certain rectangles but always

maintains a fixed overall mass, as long as the material properties in each element are taken to be the average over that element.

The amount of the material in each element is given by a fill-in coefficient between 0 and 1. The matrix of all fill-in coefficients is x and the goal is to determine the optimal value for x.

In order to actually solve the problem using topology optimization one must be able to solve for both the buckling load, F_{crit}, and the temperature distribution, T, on a domain defined by the matrix x. These values must then be used as either objective functions or constraints for the optimization problem. Since the problem of solving for F_{crit} was solved by Sigmund in [9], we emulate his approach and develop a method for solving for the temperature.

The basis for the approach is to multiply the local stiffness matrices in the finite element method by the fill-in coefficient raised to a penalty power. This is consistent with the power-law approach. Because of this, as well as due to the fact that the boundaries of the domain upon which T and F_{crit} must be solved are not well defined, we must write our own finite element method for the heat equation.

6.4.2 Solution Method

Variational Formulation

Again, we model the increase in temperature of the structure using the heat equation

$$\rho c_p T_t = k\Delta T + \dot{Q}, \qquad \forall (t,x,y) \in [0, T_f] \times \Omega, \tag{6.4.3}$$

where T is the temperature of the structure, ρ is the density, c_p is the specific heat, k is the thermal conductivity, and $\dot{Q}$ is the uniform heat source, and Ω is the material domain. We assume that initially the structure is at the same temperature as the air inside the tire; this is given by the initial condition

$$T(0, \cdot) = T_\infty, \qquad \forall (x,y) \in \Omega.$$

The surface of the structure is in direct contact with the air in the tire, so it is reasonable to suppose that Newton's law of cooling takes place along the open boundaries. We model this boundary condition as

$$\frac{\partial T}{\partial n} = h(T_\infty - T), \qquad \forall t \in [0, T_F], (x,y) \in \Gamma_{air}$$

where n is the unit outward normal, T_∞ is the temperature of the air, h is the convective heat transfer coefficient, and Γ_{air} is the part of the boundary which contacts the air. For any part of the boundary of this section of the ring that touches another section of the ring, in other words, a periodic boundary, we use insulated boundary conditions

$$\frac{\partial T}{\partial n} = 0, \qquad \forall t \in [0, T_F], (x,y) \in \Gamma_{per}.$$

Although there is air flow inside the tire, it is difficult to characterize the dynamics of the flow. Instead, we let the parameter h account for their net effects.

To begin the finite element method, we first write (6.4.3) in variational form. We multiply (6.4.3) by a test function $\phi \in H^1(\Omega)$ and integrate over Ω to obtain

$$\rho c_p (T_t, \phi) = k(\Delta T, \phi) + \dot{Q}(1, \phi), \tag{6.4.4}$$

where $(\cdot, \cdot)$ denotes the usual L^2 inner product on Ω, i.e.,

$$(f, g) = \int_\Omega fg \ d\Omega.$$

We integrate by parts in (6.4.4) to obtain

$$\rho c_p (T_t, \phi) = -k(\nabla T, \nabla \phi) + k \left\langle \frac{\partial T}{\partial n}, \phi \right\rangle_\Gamma + \dot{Q}(1, \phi),$$

for all $\phi \in H^1(\Omega)$, where $< \cdot, \cdot >_\Gamma$ denotes the L^2 inner product only on Γ, the boundary of Ω. We substitute our boundary condition to yield our final variational formulation

$$\rho c_p(T_t, \phi) = -k(\nabla T, \nabla \phi) - kh < T - T_\infty, \phi >_{\Gamma_{air}} + \dot{Q}(1, \phi), \qquad \phi \in H^1(\Omega).$$

Finite Element Method

Following standard finite element methods, we now approximate our solution space with a finite dimensional function space. For simplicity we choose to use standard bi-quadratic, rectangular elements, see Figure (fig). Thus the semi-discrete form of the heat equation becomes

$$\rho c_p M \dot{\xi} + kA\xi + khB\xi = F$$

where ξ is a vector whose components represent the value of T at each of the nodes in the discretization of the domain Ω and the finite element matrices are traditionally defined as follows

$$M_{ij} := (\phi_i, \phi_j), \tag{6.4.5}$$

$$A_{ij} := (\nabla\phi_i, \nabla\phi_j), \tag{6.4.6}$$

$$B_{ij} := < \phi_i, \phi_j >_{\Gamma_{air}}, \tag{6.4.7}$$

and,

$$F_i := hT_\infty < 1, \phi_i >_{\Gamma_{air}} + \dot{Q}(1, \phi_i). \tag{6.4.8}$$

The only difference in this case, however, is that during the assembly of the global matrices, each local matrix is multiplied by its fill-in coefficient raised to a penalty power, as per the power-law rule. For example, for rectangle k the local mass matrix M_k is defined by

$$M_k := x_k^p \left[(\phi_i, \phi_j)_k \right]_{i,j=1,\ldots,4} \tag{6.4.9}$$

where $(\cdot, \cdot)_k$ denotes integration only on rectangle k, and i and j represent the local labeling of the nodes.

The assembly of B can be handled various ways. While it makes some sense that a rectangle which is less full should have less of a contribution to the mass and stability matrices, it is possible for it to contain a longer portion of the boundary, and thus could contribute more to the matrices which represent integration over the boundaries. One possibility is to assume that the length of the boundary inside an element is proportional to the amount of material in that element, and thus B can be scaled with x^p just as M and A.

Another approach, which is the one we implemented, is to determine a threshold value above which the element is assumed "full" for the purposes of determining an exact boundary. If two elements border each other and one is above the threshold while the other is below, then there is a definite boundary at their border. We define a separate matrix of 0's and 1's for each border to determine whether or not it is a part of Γ_{air}. The integrations required in B and F are then simply multiplied by the elements of this matrix.

It would not be difficult to modify the existing code to allow for the "probability" of there being a boundary between two elements. Specifically, a value between 1 and 0 could be used based on the either how far above or below a threshold the fill-in coefficients for each element is, or how far from each other they are. The local matrices for B and F would then be multiplied by this coefficient raised to a penalty power.

Heat Equation Results

The linear ordinary differential system resulting from the semi-discrete form of the finite element method describe above is simply solved using a built-in Matlab routine. We tested several different values for x characteristic of various shapes. We give their solutions graphically in Figure 1 .

Our program shows how to solve the heat equation in a domain determined by the topology optimization method. Several key issues remain before a full implementation of this method can be made for the coupled thermal and mechanical optimization problem.
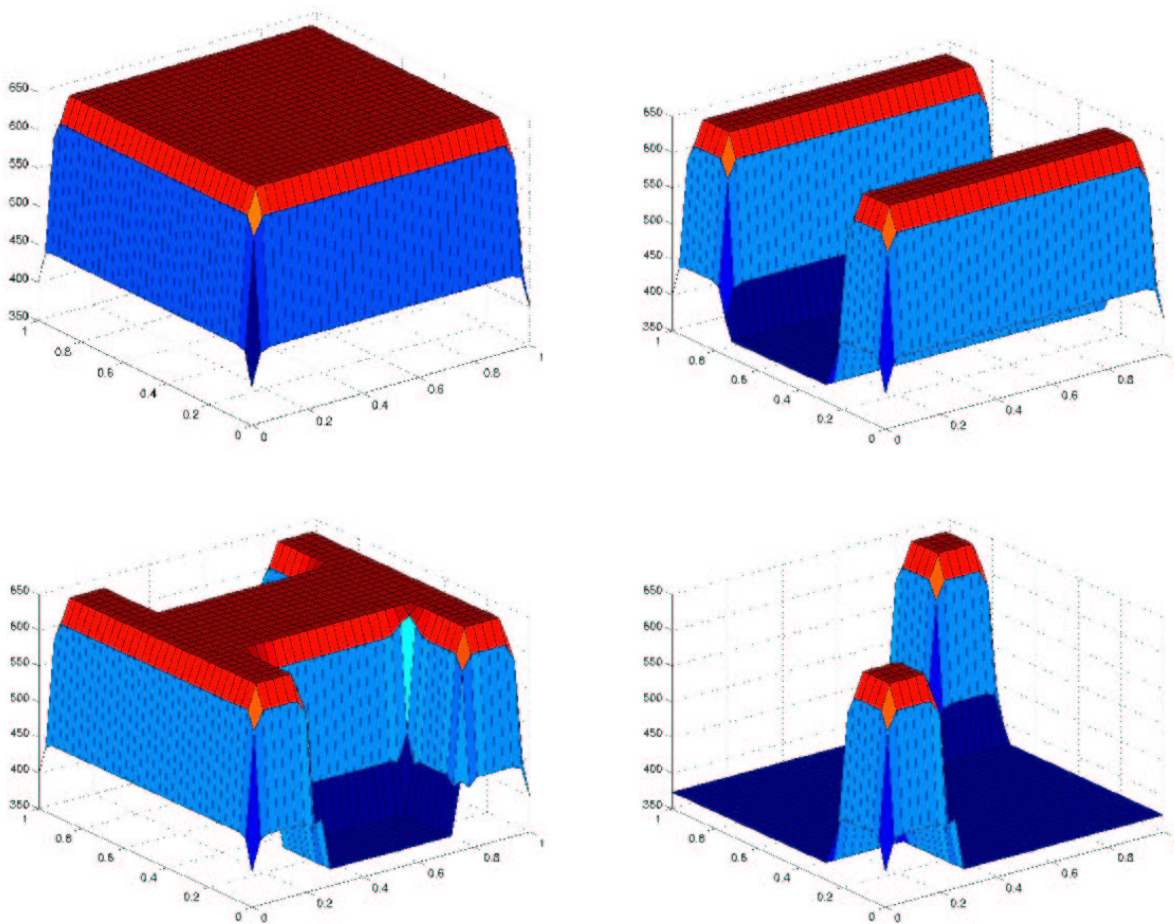
Figure 6.8: Final temperature profiles for various shapes x

6.5 Optimality Criteria method

Before we can attempt to solve a coupled thermal and mechanical optimization problem, we must first have an optimization algorithm which is capable of solving it. In his paper, Sigmund [9] used the optimality criteria implementation which is only good for a single constraint and is based on a heuristic fixed point type updating scheme (see section 4.4 [9]). In this section, we see the modification of the method based upon the first order necessary optimality condition (known as *Karush-Kuhn-Tucker conditions*, see Theorem 12.1 [8]) for a constrained optimization problem. The merits of this modification are the following:

(1) The execution time for the optimization steps are decreased by approximately 10% (see the table below).

(2) This method can be generalized for more than a single constraint.

Consider the following general optimization problem where $c(x)$ is assumed to be continuous in the design variable x

$$\min_{x} \quad c(x)$$
$$\text{s.t.} \quad g_j(x) = 0 \quad j = 1, \ldots, m.$$

Table 6.1: Comparison of runtime between Sigmund's optimization routine and our modified version

	modified version	Sigmund's version
(20,20) single force	247.86s / .06s	280.26s / 1.68s
(60,20) single force	2511.5s / .25s	3341.73s / 7.01s
(10,10) uniform force	10.53s / .000s	9.62s / 0.18s
(30,20) uniform force	342.130s / .110s	286.58s / 1.27s

For the initial design x, the corresponding values of the Lagrange multipliers are determined by solving the linear equation

$$\sum_{i=1}^{m} \lambda_i \sum_{e=1}^{N} (\epsilon_i(x) \frac{\partial g_j(x)}{\partial x_e}(x_e)) = \sum_{e=1}^{N} (\frac{\partial g_j(x)}{\partial x_e}(x_e)), \quad j = 1, \ldots, m, \tag{6.5.10}$$

where

$$\epsilon_i(x) = \frac{\frac{\partial g_i(x)}{\partial x_e}}{-\frac{\partial c(x)}{\partial x_e}} \quad i = 1, \ldots, m.$$

The equations are derived from the sensitivity analysis of each constraint on the design variable x:

$$\Delta g_j(x) = \sum_{e=1}^{N} \frac{\partial g_j(x)}{\partial x_e} \Delta x_e, \quad j = 1, \ldots, m. \tag{6.5.11}$$

Note that the left hand side of equation 6.5.11 is zero since each g_j is an equality constraint. We define

$$\Delta x_e = x_e{}^{\text{new}} - x_e = x_e(\sqrt{\sum_{i=1}^{m} \epsilon_i(x)} - 1). \tag{6.5.12}$$

These multipliers are then used to find the next iterate by the recursive formula

$$x_e{}^{\text{new}} = x_e \sqrt{\sum_{i=1}^{m} \epsilon_i(x)}. \tag{6.5.13}$$

For more detail, the reader is referred to [1]. The results compared with the Sigmund's code TOP.M are listed in the following table. Total execution time is listed before the backslash. The second time listed is for the optimization steps.

6.6   Modified version of TOP.M

```
% INITIALIZE
x(1:nely,1:nelx) = volfrac; lambda=1000;
loop = 0;
change = 1.;  chlambda = 1000;
% START ITERATION
while (change > 0.01)
  if chlambda <.01; break;
  else
    loop = loop + 1;
    xold = x;
```

```
    lambdaold=lambda;
  end;
% OPTIMALITY CRITERIA UPDATE
function [xnew,lambda]=OC(nelx,nely,x,volfrac,dc)
move = 0.2;
x=(abs([volfrac*(nelx*nely)-sum(sum(x))])/(nelx*nely))+x;
lambda= ((sum(sum(x.*sqrt(-dc))))^2)/((sum(sum(x)))^2);
xnew = max(0.001,max(x-move,min(1.,min(x+move,x.*sqrt(-dc./lambda)))));
```

6.6.1 Sensitivity of top.m

Sigmund's TOP.M solves a Topology Optimization problem for compliance minimization of statically loaded structures. The code TOP.M is designed to find the optimal topology of a support structure at a given weight while maintaining its structural stiffness. The code TOP.M assumes the support structure is statically loaded and solves a 2D problem. It initially takes the shape of a rectangle, assigns a mesh to it and then uses an artificial factor, the fill-in coefficient, to define how much mass each element contains. Eventually the fill-in coefficient should converge to a matrix which defines a definite shape that is the optimal for the given constraints and conditions.

Finding the limitations of TOP.M is one of our goals in this section. The factors that we want to study are the load types, support conditions, the penalization power, and the Poisson's ratio since our structure is made of rubber.

(1) Change the load types and support conditions

In TOP.M, the load is applied vertically in the upper middle point of the domain and the structure is supported horizontally in the two lower corners. However, in our problem, the optimization of support ring, the load is uniformly applied vertically on the top of the ring, instead of at one point. And also, the support should be fixed, which means the lower layer can't have any displacement in both vertical and horizontal direction. See Figure 6.9.
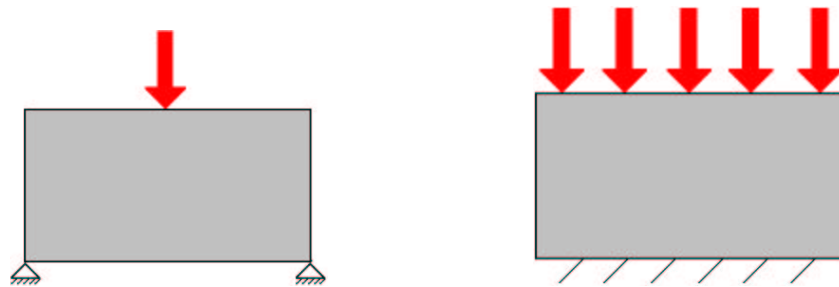

Figure 6.9: Design domain with load and support conditions. Left: load on one piont and supported in two corners and right: uniform load and fixed support

It is simple to change those load types and support conditions. We only need to change line 79 in the original code

```
F(2,1)=-1;
```

to

```
for elx=0:nelx
    F(2\*(nely$+$1)\*elx$+$2,1)=-1;
end
```

and line 80

```
fixeddofs=union([1:2:2*(nely+1)],[2*(nelx+1)*(nely+1)]);
```

to

```
fixeddofs=[];
for elx=1:nelx$+$1
    fixeddofs$=$union(fixeddofs,[2\*nely$+$1)\*elx$-$1,2\*(nely$+$1)*elx]);
end
```
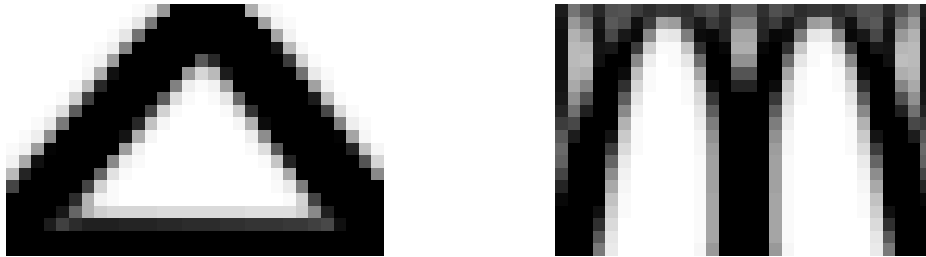
The results are compared in Figure 6.10.

Figure 6.10: Results of topology optimization. Left: load on one point and supported in two corners and right: uniform load and fixed support

We also considered another support condition by supposing that the lower layer can only have displacement in the horizontal direction. The result is shown in Figure 6.11.
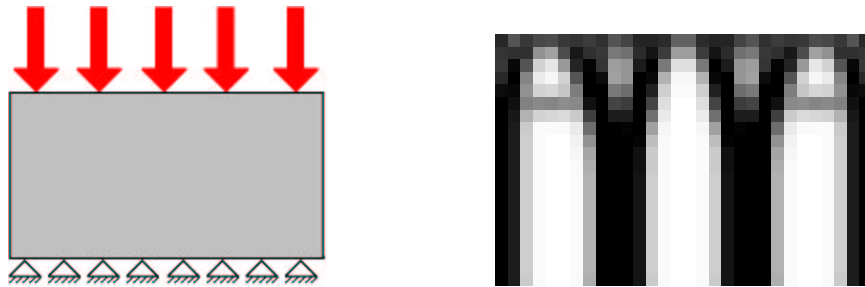
Figure 6.11: Result of topology optimization. Left: design domain and right: topology optimized domain

All of the experiments shown above are based on considering the uniform load as single load case. Perhaps we could it as a multiple load case. First, we should know what multiple load means: in a multiple load, the loads are applied on the object one by one, not at the same time. So, the final optimal design of the object should be able to support each one of those loads. We compare the result in Figure 6.12.

(2) Change the size of the domain

We tried two sizes, first $30x20$ then $20x30$. The results are shown in Figure 6.13. The load is uniformly applied vertically and is a single load case. The support is fixed.
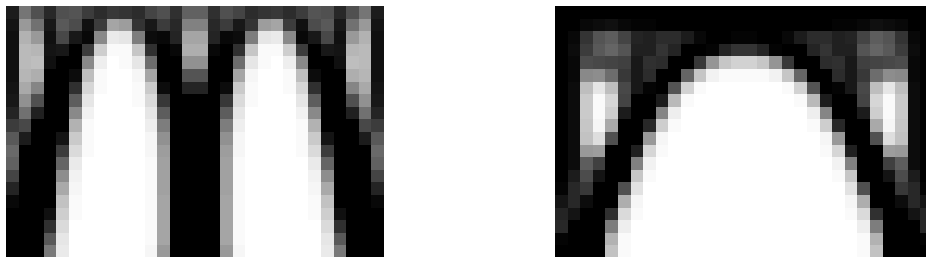
(3) Change the penalization power

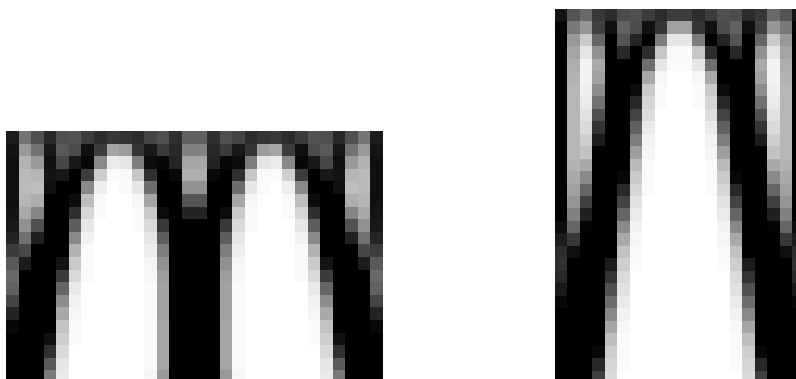Figure 6.12: Results of topology optimization. Left: single load case and right: multiple load case

Figure 6.13: Results of topology optimization. Left: size of domain is $30x20$ and right: size of domain is $20x30$

The power law approach to topology optimization is proved to be physically permissible as long as simple conditions on the power are satisfied, such as $p \geq 3$ for Poisson's ratio equal to $1/3$. Here p is the penalization power. Since the Poisson's ratio for rubber is about 0.45, the penalization power needs to be 4.0 or 5.0. Unfortunately, we do not get convergent results when $p = 4.0$ or 5.0, and convergence is slow for $p = 3.5$.

(4) Change the Poisson's ratio ν

The Poisson's ratio for rubber is about 0.45, so we tried $\nu = 0.4$ and $\nu = 0.5$ (see Figure 6.14.). As above, the load is uniformly applied vertically and considered as single load case, and the support is fixed.
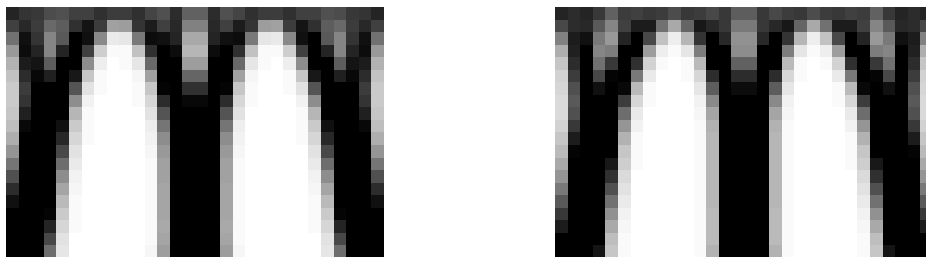

Figure 6.14: Results of topology optimization. Left: $\nu = 0.4$ and right: $\nu = 0.5$

6.7   Acknowledgements

Bibliography

[1] J.S. Arora eds., *Guide to Structural Optimization,* American Society of Civil Engineers, New York, 1997.

[2] M. P. Bendsoe, *Optimal shape design as a material distribution problem,* Structural Optimization, Vol. 1, 193-202, 1989.

[3] M. P. Bendsoe and N. Kikuchi, *Generating optimal topologies in optimal design using a homogenization method,* Computational Methods in Applied Mechanics and Engineering, Vol. 71, 197-224, 1988.

[4] Susanne C. Brenner and L. Ridgway Scott. *The Mathematical Theory of Finite Element Methods*, Vol. 15 of *Texts in Applied Mathematics*. Springer-Verlag, New York, 1994.

[5] Lawrence C. Evans. *Partial Differential Equations*, volume 19 of *Graduate Studies in Mathematics*. American Mathematical Society, Providence, Rhode Island, 1998.

[6] Claes Johnson. *Numerical solution of partial differential equations by the finite element method*. Cambridge University Press, New York, 1995.

[7] J. Mark, B. Erman, F. Eirich, *Science and Technology of Rubber, 2nd Edition*, Academic Press, 1994.

[8] J. Nocedal and S.J. Wright, *Numerical Optimization,* Springer-Verlag, New York, 2000.

[9] O. Sigmund, A 99 line topology optimization code written in Matlab, To appear in *Structural Optimization,* 2000.